Development of Electron Backscatter Diffraction as a Tool to Image and Analyse Threading Dislocations in GaN

PhD Thesis

Kieran Paul Hiller

Semiconductor Spectroscopy and Devices Group

Department of Physics

University of Strathclyde, Glasgow

March 3, 2025

This thesis is the result of the author's original research. It has been composed by the author and has not been previously submitted for examination which has led to the award of a degree.

Abstract

In this thesis, a scanning electron microscope (SEM) based technique known as electron backscatter diffraction (EBSD) is utilised and developed to investigate types of crystalline defects known as threading dislocations (TDs) in the III-nitride semiconductor gallium nitride (GaN). GaN is used prolifically in electronic and optoelectronic devices such as in high electron mobility transistors (HEMTs) and light-emitting diodes (LEDs). However, the high densities of TDs in GaN limits device performance by reducing electron mobility due to their associated strain and scattering effects, causing non-radiative recombination, and inducing local bandgap variations across the semiconductor. TDs in GaN are most commonly edge, screw, and mixed TDs. Each of these types has its own unique associated strain and misorientation profile that can affect the semiconductor's structure, and also its (opto)electronic properties.

The first step in analysing these defects within GaN is to obtain high-quality images of their distributions near to the surface of the semiconductor. By doing so it is possible to calculate TD densities (TDDs) and, if the imaging conditions are correct such that surface steps are also visible, identify which TDs are edge type or have screw component. This was achieved through the development of the virtual diode centre of mass (VDCOM) imaging technique. This is a post-processing technique applied to EBSD datasets that produces high signal images of the same area with different dominant contrast mechanisms- either crystallographically dominated (showing TDs) or topographically dominated (showing surface steps and TDs)- by monitoring changes in signal within different regions of the EBSD detector. By utilising the pixelated EBSD detector in this way, there is much greater flexibility in the different images that can be acquired with only one dataset, versus the more traditional SEM imaging technique of

electron channelling contrast imaging (ECCI) which uses individual hardware diodes.

Next, the strain and misorientation (lattice rotations) associated with TDs were simulated using an analytical simulation written in Python. It was found that the misorientation and strain associated with a screw TD is significant both in-plane (around the specimen z axis) and out-of-plane, while that of the edge TD is significant for current EBSD measurements only in-plane. This indicated that if the misorientation and strain profiles could be measured and mapped with sufficient resolution, then by comparing in-plane and out-of-plane strain and misorientation, it would be possible to distinguish between edge TDs and screw component TDs (screw and mixed) in GaN.

Strain and misorientation maps were then produced using EBSD with sufficient resolution to resolve individual TDs. This allowed the overall subgrain structure to be qualitatively interrogated and also for the TDs to be correctly identified as screw-component or edge TDs. In combination with the VDCOM technique, this means that TDs were identified and their densities calculated for a range of GaN samples. The mapping of relative strain and misorientation with such a high resolution also provides a mechanism to visualise how the strain and misorientation due to TDs varies across a particular GaN sample.

Another post-processing imaging modality was developed using Radon transformations, Radon centre of mass (RCOM) imaging. This allows EBSD users to image using the distortion of a particular crystal plane to provide contrast, much like in transmission electron microscopy (TEM). This means that only TDs affecting a particular plane are imaged, and when utilising particular invisibility criteria, the TD types can then be identified. For plan-view measurements however, this technique is limited by surface relaxation, and so full identification would require cross-sectional EBSD.

Publications and Conference Contributions

1. K. P. Hiller, A. Winkelmann, B. Hourahine, B. Starosta, A. Alasmari, P. Feng, T. Wang, P. J. Parbrook, V. Z. Zubialevich, S. Hagedorn, S. Walde, M. Weyers, P.-M. Coulon, P. A. Shields, J. Bruckbauer, and C. Trager-Cowan, "Imaging Threading Dislocations and Surface Steps in Nitride Thin Films Using Electron Backscatter Diffraction," *Microscopy and Microanalysis*, vol. 29, pp. 1879–1888, (2023).

2. K. P. Hiller, A. Winkelmann, B. Hourahine, P. J. Parbrook, J.Bruckbauer and C. Trager-Cowan, "Analysis of misorientation, strain and threading dislocations in semiconductor thin films using electron diffraction in the scanning electron microscope", due for submission to *Nature Materials* in early 2025

3. Oral Conference Presentation: "Misorientation and Strain Associated with Threading Dislocations in GaN using Electron Backscatter Diffraction" - UK Nitrides Consortium (UKNC) Winter Conference 2024

4. Conference Poster Presentation: "Imaging and Quantitative Analysis of Individual Dislocations in GaN using Electron Backscatter Diffraction (EBSD)" - International Workshop on Nitride Semiconductors (IWN) 2022

5. Oral Conference Presentation: "Quantitative Dislocation Analysis in Thin Film GaN Using Imaging Techniques in the SEM" - UK Nitrides Consortium (UKNC) Winter Conference 2022

6. Oral Conference Presentation: "Imaging Techniques for Quantitative Defect Analysis in EBSD" - AGH University, Krakow EBSD Meeting 2021

7. Oral Conference Presentation: "Quantitative Orientation Data from Thin Film GaN Using Virtual Diode and Centre of Mass Imaging" - Royal Microscopical Society (RMS) Annual EBSD Meeting 2021

Contents

Acknowledgements

During the course of my PhD I have been lucky enough to have the help and support from a number of people in my life- some of whom I've been close to for much of my life and some of whom I've grown close to since starting the PhD. I would like to take this opportunity to thank them now.

Firstly, I owe a great deal to my supervisors, Carol Trager-Cowan and Jochen Bruckbauer. Through working with them I have learned so much about EBSD, communicating and conducting research and what it means to be an academic. Through their kindness and unrelenting willingness to help in all aspects of life I have been able to successfully navigate some of the toughest periods of my life with something to show for it- this PhD. For that I cannot thank them enough.

Next I would like to thank Ben Hourahine for all the wisdom he has imparted to me during group meetings, coffee breaks and hallway encounters. His willingness to indulge even my most naive questions has been a great help and a catalyst in the development of my PhD research and my development as a physicist. In a similar vein, I would like to thank Aimo Winkelmann, without whom I would not have had the privilege to work on such interesting projects. Aimo's work provided the foundations for much of my PhD and he was always only an email or Zoom meeting away when I had difficult questions.

To my PhD colleagues (Dale, Meg, Alex and Anejo) and other inhabitants of the second floor who kept me busy in my downtime with crosswords, games of pool and conversations regarding just about anything- thank you.

I would also like to thank Professor Rachel Oliver and Dr Menno Kappers at the Cambridge Centre for Gallium Nitride, University of Cambridge for providing the thin

film GaN samples for us to analyse.

This brings me to thank many of the people outside the University of Strathclyde who have had an immeasurable impact on my life both before and during my PhD. The first of these groups of people is a core group of friends I've had throughout university, and even school for a few of them (Thom, Matteo, Max, Sam, Luke, Stu, Bruce, Martin, Reece, Ewan O and Ewan L). Although they may not know it, at times during my PhD they have kept me afloat with our nights out, discussions of music and sport and their seemingly endless patience for me talking absolute rubbish. I thank them for the years of our friendship so far and look forward to many more.

I would also like to thank a new group of friends I have made during my PhD- a group of people that I have become deeply fond of and that mean a great deal to me (Gio, Chris, Léo, Charlie, Noé, Diego, Silas, Elli, Amanda and Kyndall). They are some of the most down to Earth people I have ever met, and their company has given me many moments of laughter and joy. They have reinvigorated my passion for life- thank you.

To my longtime friends and ex-flatmates Calum and Robbie, thank you for the endless days of climbing, swimming, camping and general shenanigans. I have enjoyed them thoroughly and look forward to planning many more in your company.

A final friend I would like to acknowledge is Grant, whom I met during the first few days of my undergraduate degree. We have been on a long journey in physics together and I'm extremely grateful for his friendship, advice and kindness. While our PhDs may be the end of our shared academic journey, I look forward to our continued friendship.

Now, to my partner Ioana, I don't think the words thank you are enough. She has given me so much support, love and encouragement for so many of my days (good and bad) throughout my PhD. I am forever grateful.

My last and biggest thank you goes to my family, whom I love dearly. My brothers Liam and Callum have been in my corner my whole life, helping me build my character and confidence and providing wisdom and counsel whenever I've asked. I am eternally grateful to have them as my brothers and use them as a constant reference point for the

person I am trying to be. To my father, Ian, the constant support, care and inspiration he gives me each day has kept me motivated and driven me towards the end of this PhD journey. I could not have asked for a better or more thoughtful father. To my dog, Che, I am hugely grateful for his wonderful companionship, for keeping me active during periods of intense study, and for always making me smile when I walk through the door. Finally, I would like to thank my mother, Andrea, to whom I dedicate this thesis. The values and principles she instilled in me drive me to be a better person and to try to leave the world a better place than I found it. In the tough moments her words have guided me and given me comfort. I know she would be proud.

List of Abbreviations

AFM	Atomic force microscopy
AlN	Aluminium nitride
BSD	Backscattered diode
BSE	Backscattered electron
COM	Centre of mass
EBSD	Electron backscatter diffraction
ECCI	Electron channelling contrast imaging
ELOG	Epitaxial lateral overgrowth
FSD	Forescatter diode
GaN	Gallium nitride
GND	Geometrically necessary dislocations
GROD	Grain reference orientation deviation
HEMT	High electron mobility transistor
LED	Light-emitting diode
MOVPE	Metal-organic vapour phase epitaxy
RCOM	Radon centre of mass
ROI	Region of interest
SEM	Scanning electron microscope
TD	Threading dislocation
TDD	Threading dislocation density
TEM	Transmission electron microscope
TKD	Transmission Kikuchi diffraction
VD	Virtual diode

VDCOM	Virtual diode centre of mass
WBV	Weighted Burgers Vector

Chapter 1

Motivation

To say that, as a society, we are reliant on semiconductor-based (opto)electronics is a considerable understatement. Integrated circuits using semiconductor technology dominate our lives, from the cars we drive, the computers on which we work, the lighting that illuminates our homes and streets, to the medical instrumentation used in our hospitals. In fact, it is impossible to overstate the importance of semiconductor-based electronics, illustrated by the fact that this list does not even scratch the surface of their current functionality. Moreover, these devices are currently being researched, developed, and produced faster than at any other time in the history of the human race, with over 1.1 trillion produced in 2021 alone and the industry itself expected to grow to a value of $1 trillion by 2030 [1].

Each type of semiconductor has its own characteristics, which makes it uniquely qualified for its task, whether that characteristic is the energy band gap defining the wavelength of light emitted from a light emitting diode (LED) or the mobility of charge carriers providing the speed with which tasks can be carried out in high-frequency electronics. One semiconductor in particular that is used in both of these applications is gallium nitride (GaN) [2–5]. Despite a booming industry, GaN is still not a completely understood material. While its characteristics make it extremely desirable for electronic applications, it suffers from an unusually high density of threading dislocations (TDs), a type of extended defect that is detrimental to its performance [6–9].

In order to finely tune the performance and efficiency of these devices, the behaviour

and characteristics of GaN must be well known. Moreover, threading dislocations must be fully understood and their number reduced in the manufacturing process. Physicists, engineers and materials scientists are at the heart of driving this characterisation and analysis forward. This involves a combination of experimental and theoretical work on how GaN is grown (manufactured), how effectively it performs in given electronics, and how commercially viable it is. In a world where our electronics need to be mass-produced, perhaps it is not surprising that the latter point often takes precedence. However, in order to produce high-quality GaN in large volumes, we must have experimental characterisation techniques which can match the efficiency and pace of industry. That is to say, more generally, we must be able to test our semiconductor materials and provide conclusions with how they can be improved for future applications quickly.

The number of techniques used for the characterisation of these materials is vast, including but not limited to X-ray diffraction, Raman Spectroscopy, cathodoluminescence, neutron diffraction, atomic force microscopy, electron channeling contrast imaging (ECCI), electron backscatter diffraction (EBSD), and transmission electron microscopy.

This thesis focuses on EBSD in particular, a scanning electron (SEM) microscope-based technique used for the analysis of crystalline materials (ceramics, metal alloys, and semiconductors). EBSD is addressing a current need for fast, non-destructive quantitative analysis of materials with high statistics. This is, of course, hugely beneficial for the field of semiconductor development, where EBSD has provided sufficient proof that it can be extremely useful in threading dislocation analysis [10–15]. Consequently, the aim of this research is to push the boundaries of using EBSD in the analysis of threading dislocations in GaN.

During the course of the research, EBSD was further developed as a tool to image TDs at the surface of GaN. This involved developing new image processing techniques which can be applied to EBSD datasets post-acquisition, known as virtual diode center of mass imaging (VDCOM). This provides the functionality to acquire high-signal, high spatial resolution images at the same time as the quantitative angular and strain information that EBSD typically provides. Moreover, by analysing misorientation and

strain information at sufficient spatial resolution, it was shown that it is possible to distinguish between screw component and pure edge TDs. It was also shown that it is possible to obtain strain information with sufficient resolution to resolve the strain distributions associated with individual TDs. The experimental strain was compared with analytical simulations in order to better understand its distribution, important for device engineering. Finally, a novel image processing method was developed to image threading dislocations affecting individual crystal planes, providing greater insight for their characterisation.

Overall, this research provides valuable EBSD based techniques for the analysis of TDs in GaN, which can be extended to other materials: semiconductors, ceramics, and metal alloys.

Chapter 2

Introduction

This chapter is split into two halves and describes the fundamentals required for understanding the work reported in Chapters 3 to 6. The first half of the chapter provides the relevant material physics background to understand how TDs affect GaN and GaN-based devices. It will do so by first summarising some basic crystallography so that the effects of TDs on a general crystalline material can be understood. The relevant details of GaN as a material are then discussed- this includes its basic properties and crystal structure, how it is grown, and also outlines GaN-based devices. The first half of the chapter then concludes by describing how TDs affect GaN specifically and the impact this can have on GaN-based devices.

The second half of this chapter will address the experimental methods used in this thesis to interrogate TDs in GaN. It will describe the basics of scanning electron microscopy and the interaction between electrons and matter. It will then describe the basics of electron backscatter diffraction (EBSD) and how information such as crystal misorientation and strain can be extracted from EBSD measurements.

Ultimately, this should provide the relevant physics background and motivation for the following chapters, which discuss imaging of TDs in GaN using EBSD, simulating their associated strain fields and lattice rotations, and experimentally measuring their strain and misorientation using EBSD.

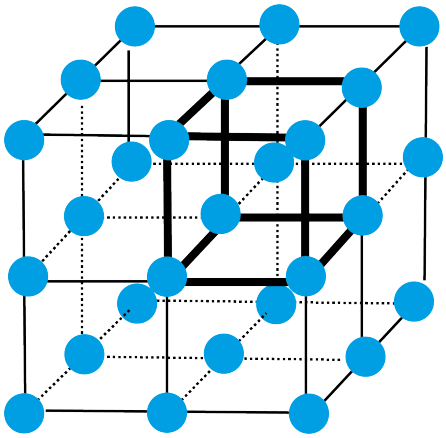

Figure 2.1: A simple cubic lattice, with the unit cell (the fundamental repeated building block in the lattice) highlighted with bold lines.

2.1 Background Theory

2.1.1 Bravais Lattice and Crystal Planes

A basic three-dimensional, perfect crystalline solid can be defined as a regular arrangement of atoms. This can be visualised by a structure known as a lattice. A lattice is simply an infinite set of points in space, where the surroundings of each individual lattice point are identical to those at any other lattice point [16]. There are a number of different lattice geometries. In order to define the geometry, rather than considering a lattice in its entirety, one can describe it by the smaller, fundamental building block that makes up the particular lattice when repeated in space. This is known as a unit cell. Figure 2.1 shows a simple cubic lattice structure with a unit cell highlighted.

For the cubic cell shown in 2.1, the unit cell vectors, **a**, **b** and **c** run along the edges of the unit cells in the Cartesian x, y and z directions. The magnitudes of these vectors are known as the lattice parameters [17]. These are particularly important parameters for describing a crystal and become very useful for defining how a lattice is distorted in a non-perfect crystal. For a perfect simple cubic lattice a = b = c. The angles between these vectors are α, β and γ, with the convention that α is the angle between **b** and **c**, moving on cyclically from there. When discussing crystallography, it is often common to refer to 'sample coordinates', described by the lattice vectors and angles,

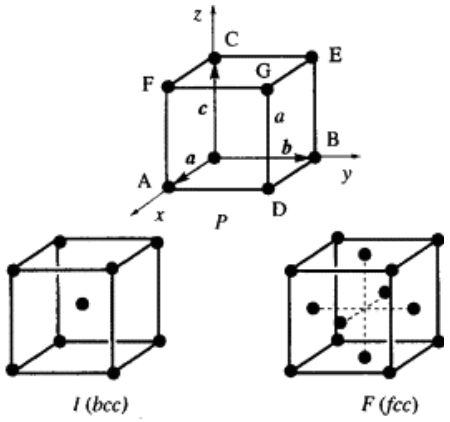

Figure 2.2: Primitive cubic unit cell (P), body-centered cubic unit cell (I), and face-centered cubic unit cell (F). Figure adapted from [19].

and 'specimen coordinates', which in this thesis are described using the *xyz* Cartesian coordinate system.

A simple cubic cell contains a total of one lattice point, meaning it is a *primitive cell*. However, in certain cases it is more useful and convenient to use non-primitive cells (containing more than one lattice point) to describe the symmetry of a crystal structure [18]. Examples of this include the body-centred cubic cell, containing two lattice points, and the face-centred cubic cell, containing four lattice points (Figure 2.2).

Each point in a lattice may well only be one atom, at which point the lattice is defined as monatomic. However, more generally, each lattice point will correspond to some arrangement of atoms, defined as a basis. Therefore, the transformation from a lattice to a crystal structure involves replacing lattice points with the given basis. As such, when choosing a non-primitive lattice that best relates to the symmetry of the crystal structure, it is necessary to choose it so that when repeated, the chemical character of the crystal is maintained.

In total, there are fourteen lattices used to describe the geometry of crystal systems. These are known as the Bravais Lattices and are listed in Table 2.1 [20].

When analysing crystal structure and characteristics, it is imperative to be able to discuss crystal directions and the geometry of the system. To define a crystal direction, consider a vector, **r**, relating two points anywhere on a lattice via translation along the

Crystal System	Unit Cell Descriptors	Bravais Lattice
Triclinic	$a \neq b \neq c$ $\alpha \neq \beta \neq \gamma$	Primitive
Monoclinic	$a \neq b \neq c$ $\alpha = \beta = 90° \neq \gamma$	Primitive, Base-centred
Orthorhombic	$a \neq b \neq c$ $\alpha = \beta = \gamma = 90°$	Primitive, Base-centred, Body-centred, Face-centred
Tetragonal	$a = b \neq c$ $\alpha = \beta = \gamma = 90°$	Primitive, Body-centred
Cubic	$a = b = c$ $\alpha = \beta = \gamma = 90°$	Primitive, Body-centred, Face-centred
Trigonal	$a = b = c$ $120° > \alpha = \beta = \gamma \neq 90°$	Rhombohedral Primitive
Hexagonal	$a = b \neq c$ $\alpha = \beta = 90°, \gamma = 60°$	Primitive

Table 2.1: The seven crystal systems with the corresponding fourteen Bravais lattices and their unit cell descriptors (lattice parameters and angles).

a, b and c crystal coordinate axes:

$$\mathbf{r} = U\mathbf{a} + V\mathbf{b} + W\mathbf{c} \tag{2.1}$$

where **a**, **b** and **c** are the unit cell vectors (basis vectors) parallel to the a, b and c crystal directions, defined earlier, and U, V and W are factors that represent translation along each basis vector direction. The crystal direction defined by this vector, **r**, is then given as [UVW]. Further to this, it can also be useful to decompose the three-dimensional Bravais lattice into two-dimensional arrays, known as planes. There are an infinite number of different types of planes that can be drawn in a lattice and each type, or family, of planes intersects all lattice points. Again, rather than considering the entire lattice, all crystallographic planes can be described using the unit cell and *Miller Indices* [20]. For a given coordinate system, Miller indices for any given plane can be obtained by taking the reciprocal of the intercepts along each given axis weighted by the basis vectors along those axes. These indices are then transformed into their lowest integer form, hkl, with the particular plane then identified as (hkl). Negative indices are indicated using a bar notation, such that a negative h index is given as $\bar{h}$.

Of course, there are many cases where planes may be symmetrically equivalent, this is known as multiplicity. A group of symmetrically equivalent planes are noted as $\{hkl\}$. It is important to be aware of a caveat when working with Miller Indices and that is when describing crystals with a hexagonal structure. In this case, planes that are symmetrically equivalent can have different indices that are not obviously permutations of one another. For example, for a cubic crystal the directions [100], [010], [001], [$\bar{1}$00], [0$\bar{1}$0] and [00$\bar{1}$] are all symmetrically equivalent and have indices which are permutations of one another. Hexagonal crystals however have six-fold symmetry and one set of their equivalent symmetrical directions are [100], [110], [010], [$\bar{1}$00], [$\bar{1}\bar{1}$0] and [0$\bar{1}$0]. These indices are not obvious permutations of one another and so extracting their symmetry from just the indices is difficult. Consequently, Miller-Bravais indexing is used instead. This is a four-index convention. For planes the indices are $hkil$, where $i = -(h + k)$. While for crystal directions the indices are $uvtw$, where $u = (2U-V)/3$, $v = (2V-U)/3$, $t = -(U + V)$ and $w = W$. This gives the symmetrical hexagonal directions the new indices [2$\bar{1}\bar{1}$0], [11$\bar{2}$0], [$\bar{1}$2$\bar{1}$0], [$\bar{2}$110], [$\bar{1}\bar{1}$20] and [1$\bar{2}$10]. These are clearly permutations of one another and so the symmetry of these directions becomes apparent from the indices.

2.1.2 Types of Defect and Effects on Crystal Lattice

When learning basic crystallographic conventions, it is often easiest to consider a perfect crystal, i.e. one which has not been distorted. However, in reality, perfect crystals do not exist. Deviations from the perfect structure are known as defects [21]. This section discusses two important types of defect: *Point Defects* and *Extended Defects*.

Point Defects

A defect that occurs at or around a single lattice point is known as a point defect. The point defect itself does not extend any further into the lattice structure [16]. Three types of point defect will be described here: interstitial defects, vacancies and impurities. The latter of which is considered an extrinsic point defect [22].

A vacancy occurs when an atom has been removed from a lattice point, or atomic

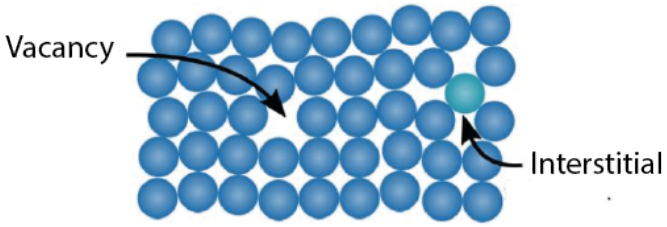

Figure 2.3: A crystal lattice distorted by a vacancy (atom has been removed from its atomic site) and an interstitial point defect (an atom inserted at a non-lattice/atomic site). Figure taken from [24].

site. They, like other point defects, are thermodynamically stable and may be formed when thermal fluctuations are such that an atom may be released from its site and become isolated at the surface of the material [20]. Vacancies reduce the Helmholtz free energy (F) of the crystal at a temperature T by:

$$\Delta F = \Delta U - T\Delta S \tag{2.2}$$

Where U is the crystal's internal energy and S is the configurational entropy of the vacancies in the crystal [23].

An interstitial defect occurs when an atom is present at a non-lattice site. This may be formed at the same time as a vacancy, when the displaced atom settles between lattice sites, or it may form in isolation. The former interaction has a lower formation energy. A vacancy and an interstitial are shown in Figure 2.3.

An impurity is also a type of point defect. It occurs when an impurity atom (a different atom to those in the crystal basis) is either substituted in place of a parent atom of the crystal or when taking up an interstitial location in the crystal [22]. Impurities can be intentional or unintentional. In semiconductors, the intentional addition of impurities to the crystal is known as doping and is used to alter the electrical properties of the material.

Extended Defects

Extended defects are exactly as they sound: structural defects that extend beyond the singular atomic size of point defects and propagate through a region of the crystal. Unlike point defects which can occur via thermal activation, extended defects occur due to imperfections in the crystal growth and material processing [21]. Three types of extended defect will be described here: volume defects, surface defects and line defects (known simply as dislocations).

Any change in orientation, crystal structure, state variables (such as polarisation characteristics, composition or structure) in a particular crystal volume with respect to the surrounding crystal is a volume defect [25]. The most important volume defect to understand in relation to this thesis is a *grain*. Grains are characterised as neighbouring regions of the crystal structure which are misoriented with respect to each other. When two regions of crystal are 'misoriented' with respect to one another, it means that there is a rotational transformation required to bring the reference frame of one region of the crystal into coincidence with the other.

The interface at which two misoriented grains meet is known as a *grain boundary* (Figure 2.4.). This misorientation is then facilitated by the presence of line defects known as a *dislocations* (discussed shortly), which subtends the boundaries of the misoriented regions. Neighbouring grains which differ in phase, i.e. chemical composition and/or changes in the crystal structure, meet at a *phase boundary* [25]. Both of these boundaries, when propagating through to the surface, can be types of surface defects. When performing crystallographic analysis on a particular sample, grain boundaries are often defined via a threshold misorientation (eg $> 5^{\circ}$). The interface is deemed a grain boundary if two regions are sufficiently misoriented above this threshold. This threshold can be different for different materials, and in some cases, when smaller misorientation occurs, the interface is termed a *subgrain boundary*. Grain boundaries can also be 'high angle' or 'low angle' grain boundaries- which are often distinguished by the dislocation content along the boundary. For example, low-angle grain boundaries generally contain ordered lines of separated dislocations, whereas high-angle grain boundaries are subtended by lines of dislocations with overlapping cores. Grain boundaries can affect

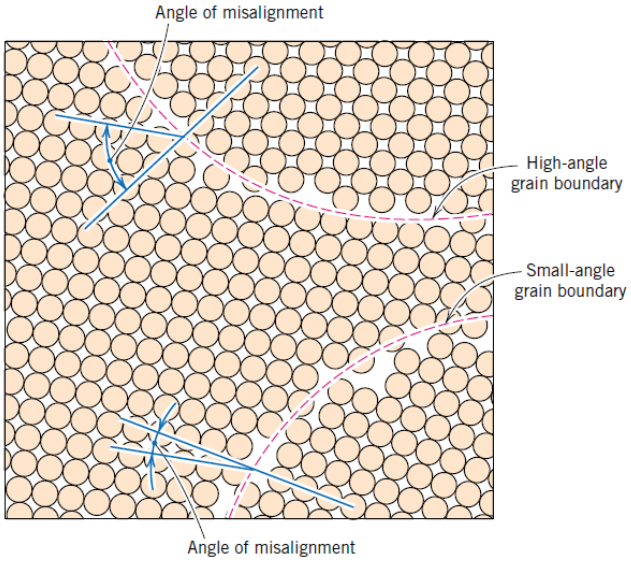

Figure 2.4: Three sections of the crystal lattice misoriented with respect to each other. Two grain boundaries are formed in the image: a high-angle boundary and a low-angle boundary. Figure taken from [28].

the electrical properties of materials, such as changing the conductivity of GaN [26,27].

The main defect around which this thesis is centered is a line defect known as a *dislocation*. Consider two planes of atoms, one on top of the other. Plastic deformation of crystalline material typically occurs when one plane of atoms slides over the other, resulting in a shear (Figure. 2.5). This is known as slip [29]. The slip direction is the direction of the shear, while the slip plane is the plane on which the slip occurs. In 1926 Frenkel [30] calculated the shear stress required for this to take place. However, this value for shear stress was much larger than that obtained by experimental methods when interrogating the minimum stress required to cause plastic slip [31]. The theoretical minimum was based on all of the bonds between atoms involved in the shear breaking during the slip, with new bonds forming after it. The discrepancy in experimental and theoretical values was explained simultaneously and separately by Polanyi, Taylor, and Orowan [31–33]. They stated that a very small stress is required for a slip of one single atomic spacing. This single unit slip then propagates across the plane along the shear direction. The boundary of this slip is a dislocation. It is worth noting that while this description of dislocation formation is based on deformation of the

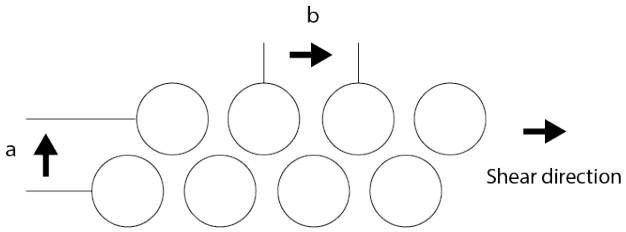

Figure 2.5: Atomic plane shearing with respect to a neighbouring plane due to an applied stress. a is the distance between planes and b is the spacing between atoms in the direction of the shear.

crystal lattice, in GaN dislocations are typically formed during epitaxial growth. Their origin and physical effects are described for the case of GaN in subsection 2.1.7 *Strain and Threading Dislocations in GaN* of this thesis. However, the geometry within the crystal lattice is discussed now for the case of three basic dislocation structures: edge, screw and mixed.

An edge dislocation occurs via an inplane-shear resulting in an incomplete plane of atoms (for *c*-oriented GaN this means the plane normal to the *c*-axis). Consider the structure in Figure 2.6a). An extra half plane of atoms inserted in the location ABCD (Figure 2.6b)) will cause neighbouring atoms to be displaced from their original lattice position, with the magnitude of the resulting distortion decreasing with increasing distance away from the dislocation line DC. This is what is known as an edge dislocation [21, 22]. Edge dislocations cause *in-plane* rotational distortion, i.e. the axis of this rotation is the surface normal.

A screw dislocation is formed when an out-of-plane shear distortion occurs (Figure 2.6c) and d)). This causes previously parallel planes of atoms to spiral, resulting in the effect observed in Figure 2.6f). This results in an out-of-plane rotation. A mixed dislocation is simply a combination of both an edge and a screw dislocation. In order to describe a dislocation and its effect on the lattice, a quantity known as a Burgers vector is used. In order to understand a Burgers vector, one must first understand a Burgers circuit.

An example of a Burgers circuit is a closed loop around a dislocation line in an otherwise perfect crystal lattice. If the dislocation line and its associated distortion are then removed, the Burgers circuit will no longer be closed. The vector required to close

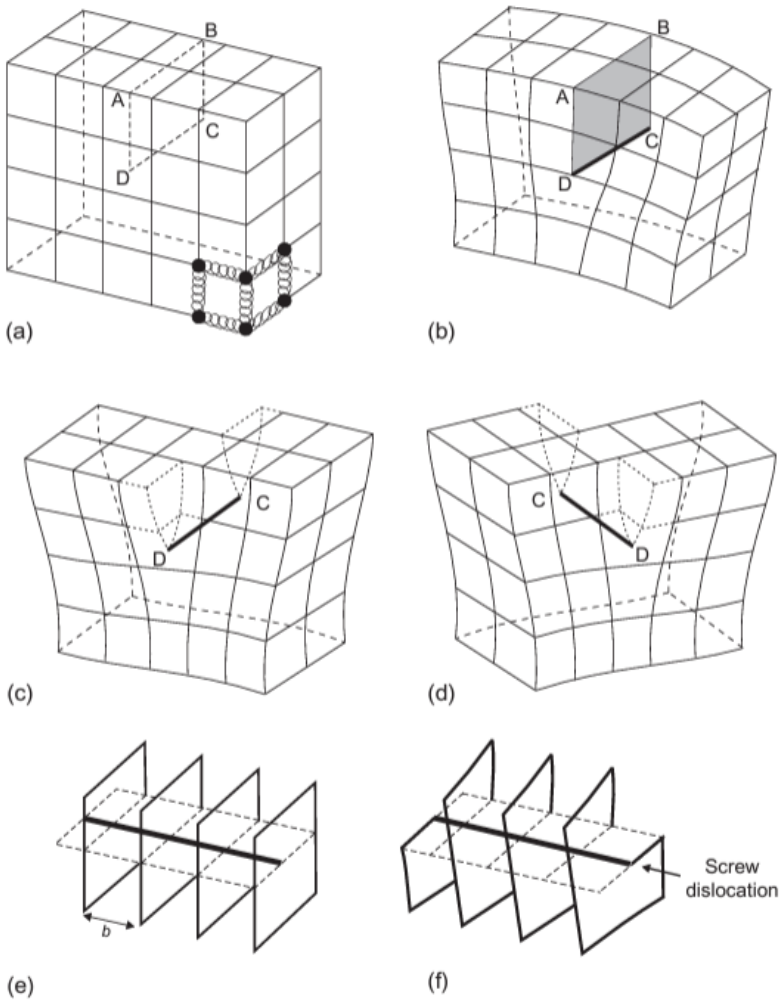

Figure 2.6: a) A perfect undistorted cubic crystalline lattice. b) The same lattice with a half plane of atoms inserted at ABCD (edge dislocation). c) A left-handed screw dislocation and d) a right-handed screw dislocation with dislocation line DC. e) Crystal planes in a perfect lattice with spacing b. f) The same crystal planes distorted by a right-handed screw dislocation. Figure taken from [22].

the second circuit is known as the Burgers vector, associated with the dislocation line in the distorted lattice [21, 22]. This can be seen in Figure 2.7. For a screw dislocation the Burgers vector is parallel to the dislocation line, while the Burgers vector for an edge dislocation is perpendicular to the dislocation line.

2.1.3 Strain

When considering crystal lattice distortion, it is useful to quantify the displacement incurred by parts of the crystal lattice. Any point on the lattice can be defined by a radius vector, **r** whose components are in the *x, y, z* Cartesian reference frame ($x_1 = x$, $x_2 = y$ and $x_3 = z$). Thus, when considering a distortion of the lattice, the lattice points are displaced, and the radius vector of a particular lattice point is altered, becoming $\mathbf{r}'$. Therefore, the overall displacement of an individual lattice point can be given by the *displacement vector*, $\mathbf{u} = \mathbf{r}' - \mathbf{r}$, whose components are:

$$\mathbf{u}_i = x'_i - x_i \tag{2.3}$$

Where x'_i are the components of **r'** and are themselves a function of the components x_i [34].

Now, for small strains, one can consider two points on the undeformed crystal lattice separated by an infinitesimal radius vector dx_i. It is then easy to see that after deformation by an infinitesimal displacement vector $d\mathbf{u} = du_i$, the new radius vector joining the same two points will be:

$$dx'_i = dx_i + du_i \tag{2.4}$$

With the magnitude of the vectors $d\mathbf{r}$ and $d\mathbf{r}'$ being $dr = \sqrt{dx_1^2 + dx_2^2 + dx_3^2 = dx_i^2}$ and $dr' = \sqrt{dx_1'^2 + dx_2'^2 + dx_3'^2 = dx_i'^2 = (dx_i + du_i)^2}$, respectively. This gives:

$$dr'^2 = dr^2 + \sum_{i=1}^{3}(2dx_i du_i + du_i^2) \tag{2.5}$$

Substituting $du_i = (\frac{\partial u_i}{\partial x_k})dx_k$ and $du_i^2 = (\frac{\partial u_i}{\partial x_k})dx_k(\frac{\partial u_i}{\partial x_l})dx_l$ yields:

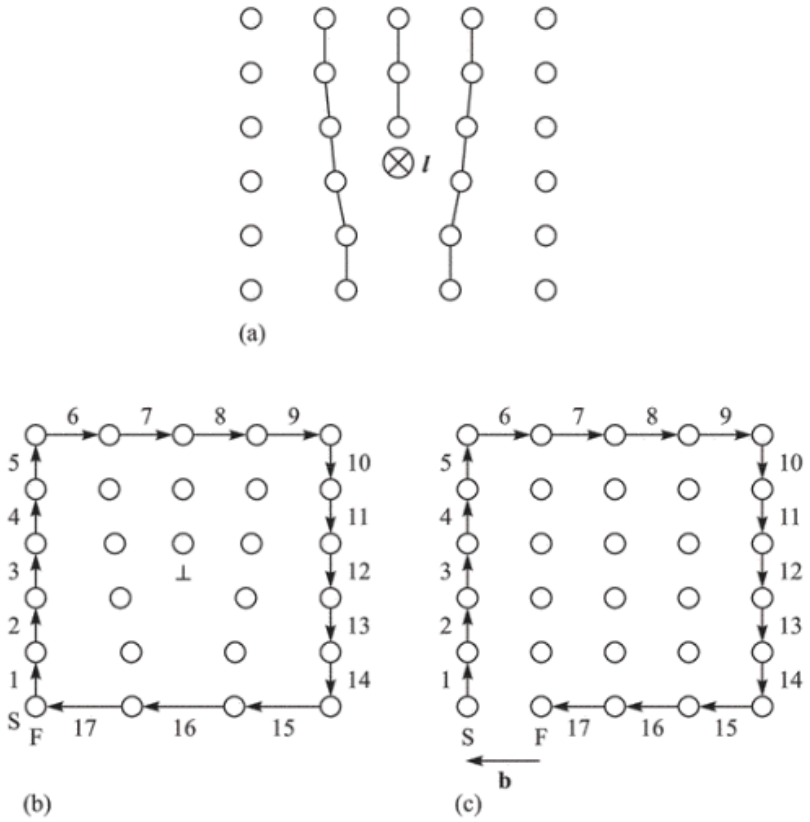

Figure 2.7: a) A dislocation line corresponding to an edge dislocation is shown in a). To define the Burgers vector of this dislocation, a closed circuit can be drawn around the dislocation line as in b). The start and end points of this circuit are marked by S and F, respectively. Drawing the same circuit around a perfect crystal lattice, as in c), will yield a circuit closure failure, as S and F are now at different lattice points. The Burgers vector of this edge dislocation is then the line SF and is denoted by **b**. Figure taken from [21].

$$dr'^2 = dr^2 + \sum_{i,k=1}^{3} (2\frac{\partial u_i}{\partial x_k} dx_i dx_k + \frac{\partial u_i}{\partial x_k}\frac{\partial u_i}{\partial x_l} dx_k dx_l) \tag{2.6}$$

Given the summation is taken over both i and k, $\frac{\partial u_i}{\partial x_k} dx_i dx_k$ and $\frac{\partial u_k}{\partial x_i} dx_i dx_k$ are both equivalent. The distance between two points on the lattice post-deformation is then:

$$dr'^2 = dr^2 + \sum_{i,k=1}^{3} 2\epsilon_{ik} dx_i dx_k \tag{2.7}$$

Where the tensor, ϵ_{ik} is the infinitesimal strain tensor:

$$\epsilon_{ik} = \frac{1}{2}(\frac{\partial u_i}{\partial x_k} + \frac{\partial u_k}{\partial x_i} + \frac{\partial u_l}{\partial x_i}\frac{\partial u_l}{\partial x_k}) \tag{2.8}$$

Generally, for crystal systems, and semiconductors in particular, strains will be small. Mathematically, this means the displacement will be significantly smaller than the overall distance between the points. Consequently, the factor $\frac{\partial u_l}{\partial x_i}\frac{\partial u_l}{\partial x_k}$ can, in most cases, be considered negligible and is often neglected when stating the equation for the strain tensor. This is a symmetrical tensor and is given in full by:

$$\begin{bmatrix} \epsilon_{xx} & \epsilon_{xy} & \epsilon_{xz} \\ \epsilon_{yx} & \epsilon_{yy} & \epsilon_{yz} \\ \epsilon_{zx} & \epsilon_{zy} & \epsilon_{zz} \end{bmatrix} \tag{2.9}$$

Where subscripts 1, 2 and 3 from Eq. 2.8 have been converted to x, y and z respectively to align with the Cartesian reference frame and $\epsilon_{xy} = \epsilon_{yx}$, $\epsilon_{xz} = \epsilon_{zx}$ and $\epsilon_{yz} = \epsilon_{zy}$ due to symmetry [35]. The three diagonal strains ϵ_{xx}, ϵ_{yy} and ϵ_{zz} are known as the normal (or principal) strains. They represent expansion/compression along the x, y, and z Cartesian directions, respectively. The distortion imposed then by these components is both a change in shape and a change in volume. The change in shape is referred to as *deviatoric* strain while the change in volume is *hydrostatic* strain. The hydrostatic strain is simply the average of the three normal strain components ($\epsilon_{hyd} = \frac{\epsilon_{xx}+\epsilon_{yy}+\epsilon_{zz}}{3}$). It is easiest to see the impact of hydrostatic strain on the full strain tensor when represented as a diagonal tensor of its own:

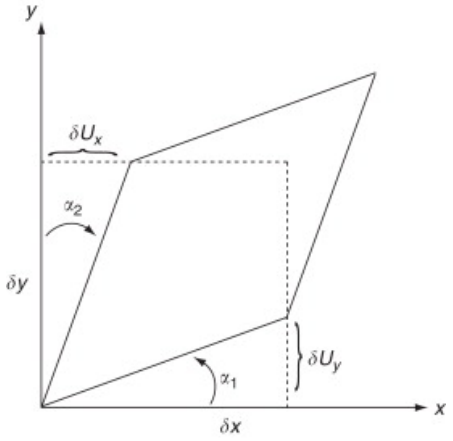

Figure 2.8: A cube distorted by shear strain in the xy plane. The shear strain can be given as a sum of the change in the displacement $\epsilon_{xy} = \frac{\partial U_x}{\partial y} + \frac{\partial U_y}{\partial x}$. Figure taken from [36].

$$\begin{bmatrix} \epsilon_{hyd} & 0 & 0 \\ 0 & \epsilon_{hyd} & 0 \\ 0 & 0 & \epsilon_{hyd} \end{bmatrix} \tag{2.10}$$

As is illustrated by this tensor, the off-diagonal components of the strain tensor, known as the shear strains, are unaffected by hydrostatic strain and so only constitute a change in shape. A cubic structure undergoing the shear strain $\epsilon_{xy} \neq 0$ is shown in Figure 2.8. As the distortion is small, the shear strain can be given as a sum of the change in the displacement $\epsilon_{xy} = \frac{\partial u_x}{\partial y} + \frac{\partial u_y}{\partial x}$.

The nature of shear strain also illustrates that there is a rotational component to crystal distortion. This is represented by an antisymmetric tensor ω_{ik} which will not be derived explicitly here but has components:

$$\omega_{ik} = \frac{1}{2}(\frac{\partial u_i}{\partial x_k} - \frac{\partial u_k}{\partial x_i}) \tag{2.11}$$

By considering the distortion described by this tensor, and the symmetric strain tensor, it becomes very easy to describe the total crystallographic distortion that results from defects such as dislocations.

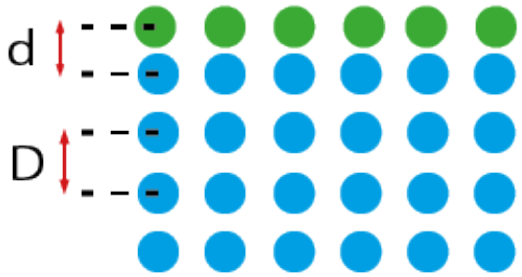

Figure 2.9: A lattice showing surface relaxation. The lattice spacing between the surface layer (blue) and the rest of the lattice (green), d, is smaller than the spacing within the rest of the lattice, D.

2.1.4 Surface Relaxation

As the experimental methods in this thesis concern the application of EBSD, and EBSD samples its information from close to the surface, it is important to understand the effects on the lattice imposed by this boundary and the additional effects that are at play compared to in the bulk of the sample. If the lattice is distorted, e.g. it is under tensile strain, the layers of atoms close to the surface boundary will experience a large asymmetry in the forces they experience [37]. The top layer, for example, is being 'pulled' by the layers of atoms below, but there is nothing to 'pull' the top layer upwards from above the surface boundary [38]. As such, the lattice spacing between the top layer and the lattice becomes smaller than the spacing further into the lattice. This contraction of the top layer, or surface, is known as *surface relaxation* (Figure 2.9.). Surface relaxation is energetically favorable and allows the crystal to lower its total energy [39]. This can be thought of as 'general surface relaxation', i.e. surface relaxation that exists purely due to the presence of a surface boundary. However, there is also surface relaxation associated with dislocations that thread to, or close to, the surface. This can cause a 'drooping' or relaxation of the material around the top of the dislocation line which reduces with increasing distance from the dislocation, an effect described by 'image forces' (the forces driving dislocations towards the surface to achieve a minimum energy configuration).

2.1.5 Displacement of the Lattice due to Threading Dislocations

Threading dislocations (TDs) are dislocations that extend, or thread, from the substrate/bottom layer or interface of a material to its free surface. They do so in order to minimise the free energy of the overall crystal system [40]. They are prolific in GaN and are the central focus of this thesis. Consequently, their effects on crystalline material must first be discussed.

The paths of TDs may be completely perpendicular to the surface, or they may be inclined, in which case they are known as *inclined* threading dislocations. Threading dislocations may interact with each other in numerous ways. Firstly, TDs with Burgers vectors of the same sign will repel each other. As such, it is common for edge TDs of the same Burgers vector to arrange themselves in a line normal to the slip plane. When this arrangement occurs with a high density of edge TDs, the associated distortion combines to produce a small rotation of the crystal lattice along the line. This is a source of a subgrain boundary or small angle tilt boundary [23]. TDs with Burgers vector of opposite sign will annihilate when meeting, reducing the overall TD density. Furthermore, TDs may intersect, resulting in a phenomenon known as jogging, where the dislocation's path through the material is perturbed.

Using isotropic elasticity, the displacement of the crystal lattice by edge, screw and mixed TDs parallel to the surface normal can be modelled. This involves considerations of both the general distortion by the Burgers vector of the TD and also the associated surface relaxation. This treatment requires a boundary condition known as the *traction-free boundary*. This is simply the assumption that the stress perpendicular to the surface, located at the surface, is zero [41]. As a result of this, the out-of-plane shear stresses must also be zero. The associated forces imposed by the surface relaxation of TDs are then known as *image forces*. This model is valid outwith the core of the dislocation (approximately 10 $\mathring{A}$). Within the core, a singularity occurs, and the model breaks down [41, 42].

The displacement field of a screw dislocation due to the Burgers vector in the infinite medium (u_i^{inf}) and the corresponding displacement due to the image forces related to the surface boundary (u_i^{img}) are:

$$u_x^{inf} = u_y^{inf} = 0 \tag{2.12}$$

$$u_z^{inf} = b_3 \frac{tan^-1(y/x)}{2\pi} \tag{2.13}$$

$$u_x^{img} = \frac{b_3 y}{2\pi(R-z)} \tag{2.14}$$

$$u_y^{img} = -\frac{b_3 x}{2\pi(R-z)} \tag{2.15}$$

$$u_z^{img} = 0 \tag{2.16}$$

Where x, y are the in-plane Cartesian coordinates and z is parallel to the TD line. In this convention, z is zero at the surface and increases into free space.
$R = \sqrt{x^2+y^2+z^2}$ and b_3 is the magnitude of the screw Burgers vector. The total displacement at position (x,y,z) is simply the sum of the infinite medium and image force terms [42].

Similarly, for an edge TD whose Burgers vector is parallel to x, the displacement field terms are:

$$u_x^{inf} = \frac{b_1}{2\pi}[tan^-1(\frac{y}{x}) + \frac{xy}{2(1-\nu)(x^2+y^2)}] \tag{2.17}$$

$$u_y^{inf} = \frac{-b_1}{2\pi}[\frac{1-2\nu}{4(1-\nu)} ln(x^+y^2) + \frac{x^2-y^2}{4(1-\nu)(x^2+y^2)}] \tag{2.18}$$

$$u_z^{inf} = 0 \tag{2.19}$$

$$u_x^{img} = \frac{\nu b_1}{4\pi(1-\nu)}[\frac{2xyz}{R(R-z)^2} + \frac{(1-2\nu)xy}{(R-z)^2}] \tag{2.20}$$

$$u_y^{img} = \frac{\nu b_1}{4\pi(1-\nu)}[(1-2\nu)ln(R-z) - \frac{(3-2\nu)z}{R-z} + \frac{(3-2\nu)y^2}{(R-z)^2} - \frac{2y^2}{R(R-z)}] \tag{2.21}$$

$$u_z^{img} = \frac{\nu b_1 y}{2\pi(1-\nu)}(\frac{1}{R} + \frac{1-2\nu}{R-z}) \tag{2.22}$$

Where b_1 is the magnitude of the edge Burgers vector and ν is Poisson's Ratio of the given material.

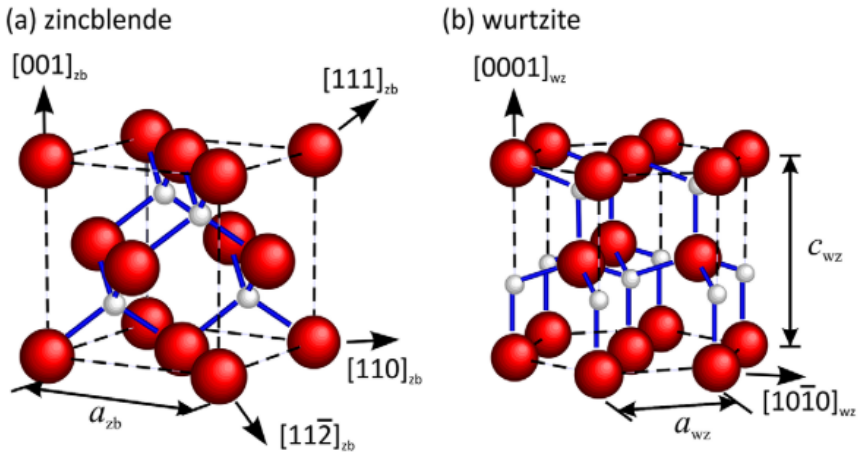

Figure 2.10: a) Cubic crystal structure of zincblende GaN. b) Hexagonal crystal structure of wurtzite GaN. Lattice parameters a and c are marked on both. Figure taken from [43].

2.1.6 Gallium Nitride

Crystal Structure and Properties

Gallium nitride (GaN) is a III-nitride semiconductor typically with a wurtzite crystal structure (hexagonal lattice), with four atoms per unit cell. This structure leads to wurtzite GaN being polar due to its lack of inversion symmetry along the c-axis, resulting in spontaneous polarisation. This is because the bond lengths in the a and c crystal directions are different, and so there is a non-net zero charge distribution in the crystal. Cubic GaN can also be grown, known as zincblende, as a way of reducing the strength of any internal fields that result from polarity [43]. The zincblende and wurtzite structures are shown in Figure 2.10. This thesis focuses solely on wurtzite GaN.

The wurtzite structure shown in Figure 2.10b) is c-oriented, meaning the c-axis is aligned with the cartesian z axis. As such, GaN grown in this way is referred to as c-plane GaN, i.e., the growth is along the c-axis. **a** and **c** are the basis vectors, as described in Section 2.1.1 *Bravais Lattice and Crystal Planes*, of the hexagonal structure. Their magnitudes a and c are the lattice constants, corresponding to the length of a side of the hexagon and the distance between vertically close-packed hexagons,

respectively. These are $a = 3.189\mathring{A}$ and $c = 5.186\mathring{A}$ [44].

Wurtzite GaN has a direct bandgap of approximately 3.4 eV, just on the edge of the ultra-violet [45, 46]. The effective mass of carriers, holes and electrons, is directly related to the band curvature. From the free electron model, the effective mass ($m*$) is inversely proportional to the curvature of the electron dispersion/band curvature [47]:

$$m*^{-1} = \frac{1}{\hbar}\frac{d^2E}{dk^2} \tag{2.23}$$

Where $\hbar$ is the modified version of Planck's constant, k is the wavevector associated with the electron, E is the energy of the electron and $\frac{d^2E}{dk^2}$ is the band curvature in reciprocal space. It is then easy to see that the greater the curvature, the smaller the effective mass and vice versa. This is because greater band curvature means electrons experience a more rapid change in energy for changes in wavevector, k, and so they can be 'accelerated' more quickly within the band (and therefore have a smaller 'effective' mass). At a temperature of 300 K, the longitudinal effective mass at Γ, the centre of the Brillouin zone, of electrons in the minima of the conduction band is $m_e = 0.20\ m_0$, while that of the holes in the uppermost valence band is $m_h = 0.32\ m_0$, where m_0 is the mass fo a free electron [48, 49].

GaN is also a piezoelectric material, meaning when external stress is applied to it, there is a redistribution of charges and polarisation occurs, spawning electric fields. Piezoelectric polarisation (P_E) therefore increases with strain and the P_E induced along the c-axis is given by the relationship:

$$P_E = e_{33}\epsilon_{zz} + e_{31}(\epsilon_{xx} + \epsilon_{yy}) \tag{2.24}$$

Where ϵ_{zz} is the strain along the c-axis, $\epsilon_{xx} = \epsilon_{yy}$ is the in-plane strain which is assumed to be isotropic and e_{33} and e_{31} are piezoelectric coefficients [50]. The piezoelectric coefficients for GaN are somewhat disputed, with recorded values falling the range between 0.63 and 1 Cm^{-2} for e_{33}, -0.32 and -0.49 Cm^{-2} for e_{31} and -0.3 and -0.33 Cm^{-2} for e_{15} [50–54].

In addition to piezoelectric polarisation, GaN also has spontaneous polarisation, P_S

which is relatively high [52]. This, in most cases, can be assumed to be isotropic [55] and when combined with P_E the total polarisation, P_{total}, of GaN can be given as:

$$P_{total} = P_E + P_S \tag{2.25}$$

The piezoelectric nature of GaN and its total polarisation mean that when the material is strained, there are significant implications on local carrier mobilities in the material, impacting Gan-based device performance. This is why it is of huge importance to be able to understand and reliably measure strain in GaN thin-films.

The change in the overall E-field (ΔE) as a result of polarisation (ΔP) is governed by the relationship:

$$\Delta E = \frac{\Delta P}{\epsilon_0(k-1)} \tag{2.26}$$

Where ϵ_0 is the permittivity of free space and k is the dielectric constant of GaN ($k = 8.9$).

Changes in the E-field can cause significant variations in the mobility of the carriers in GaN. For low E-fields the electron mobility (μ) is a constant, μ_0, known as the low field mobility. In this regime, the increase in electron drift velocity (ν) is roughly linear to the increase in the E-field [56]:

$$\nu = \mu_0 \times E \tag{2.27}$$

However, in the high-field regime, this linearity disappears as phonon and impurity scattering becomes increasingly more likely and the velocity saturates (ν_s). Consequently, the relationship between ν, E and μ must be modified to include a field dependence:

$$\nu(E) = \mu(E) \times E \tag{2.28}$$

Furthermore, there is a temperature dependence for both the low- and high-field mobility regimes, affecting when this saturation occurs. Figure 2.11 shows the relation-

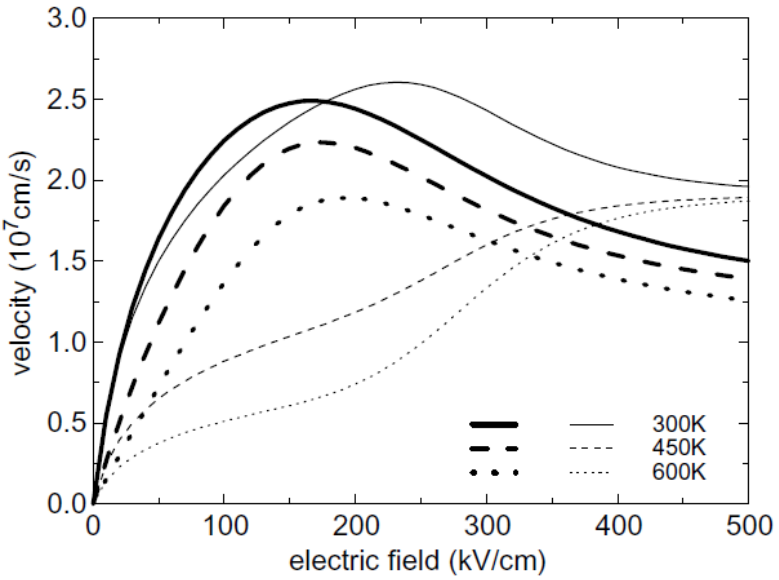

Figure 2.11: The dependence of electron drift velocity on electric field at various temperatures in wurtzite GaN is shown using a model from [56]. In the low-field regime drift velocity is roughly linearly related to E-field, resulting in a constant low-field mobility μ_0. At higher E-fields, phonon and impurity scattering occur to a much greater extent, saturating the velocity and resulting in a decrease in the now field-dependent mobility, $\mu(E)$. Figure adapted from [56].

ship between the E-field and drift velocity for electrons at various temperatures based on the model from [56].

As can be inferred from Fig. 2.11, beyond the saturation of the drift velocity, there is a significant decrease in electron mobility as the E-field continues to rise.

Growth: General

Due to the lack of bulk GaN substrates, the growth of GaN is most often heteroepitaxial, i.e., the GaN is deposited on a substrate of different chemical composition. The dominant substrates for GaN growth are sapphire, silicon, and silicon carbide, although developments are being made in producing GaN substrates [57,58]. Aside from HVPE, which was used to grow the early thin films [59], other epitaxial growth mechanisms for GaN include metal-organic vapor phase epitaxy (MOVPE), epitaxial lateral overgrowth (ELOG), and molecular beam epitaxy (MBE). The GaN thin films analysed

in this thesis were all grown via MOVPE on c-oriented sapphire. The process for this growth will now be briefly explained.

Growth: MOVPE of GaN on Sapphire

Under controlled pressure, reactants are transported into a reactor, where the sapphire substrate is located, via a vapor phase. These reactants are known as precursors, and for the production of GaN, the precursors are often NH_3 and $Ga(CH_3)_3$ [60] [61]. The precursors then dissociate and are adsorbed by the heated substrate, diffusing and forming layers of GaN until the growth process is complete [62]. For the thin-films used in this thesis, the sapphire substrate is c-oriented, meaning its c-axis is aligned with the z-axis of the reactor reference frame. Consequently, the growth direction of the GaN is also the c-axis.

One of the drawbacks of using a sapphire substrate for GaN thin films is the large lattice mismatch incurred (16%) [63]. This results in significant stresses in the first few layers of deposited GaN. To try to mitigate the effects of this, generally, a thin first section of GaN, known as a nucleation layer, is formed at a low temperature (e.g., 525 $°C$) [64] following the nitridation of the substrate layer. The remaining GaN will then be grown at a higher temperature (e.g., 1150 $°C$), accelerating the growth rate and allowing the formation of 3D GaN islands. These islands are then allowed to coalesce by changing the growth conditions once again such that lateral growth is favourable, transitioning to 2D growth and forming the full GaN thin film layer [65]. This second section will typically be at a thickness between several hundred nanometres to a few microns.

2.1.7 Strain and Threading Dislocations in GaN

When GaN is grown on c-oriented sapphire, due to the differences in crystal structure, in order to achieve the best lattice matching, there is an in-plane rotation of 30° between the two lattices [63]. This aligns the N atoms of GaN with the O atoms of Sapphire. Without this alignment, a much larger lattice mismatch persists. GaN is unbound in the c-direction but perpendicular to this, i.e. in-plane, the lattice parameter, a, of

Material	Lattice constant a	Lattice constant c	In-plane Thermal Expansion Coefficient
GaN	$a = 3.189\mathring{A}$	$c = 5.186\mathring{A}$	$5.59 \times 10^{-6}\ K^{-1}$
Sapphire	$a = 4.758\mathring{A}$	$c = 12.99\mathring{A}$	$7.5 \times 10^{-6}\ K^{-1}$

Table 2.2: Lattice parameters and thermal in-plane thermal expansion coefficients for GaN and sapphire

GaN is bound by the size of the lattice parameter of sapphire. As a result of this, the GaN must match the lattice parameter of sapphire in order to grow successfully on the substrate. In an ideal world, this would mean that both GaN and sapphire's lattice parameters, a, would share the same magnitude. However, from the previous discussion on crystal growth, it is known that there is in-fact a mismatch between their in-plane lattice parameters of up to 16%. Sapphire has $a = 4.758\ \mathring{A}$ compared to $a = 3.189\mathring{A}$ for GaN [66].

This mismatch results in the in-plane tensile strain of GaN on sapphire as its lattice parameter extends to match that of sapphire's. However, as the growth typically occurs at high temperatures, the thermal expansion coefficients of the material must also be accounted for [67]. The lattice parameters and thermal expansion coefficients for both GaN and Sapphire are given in Table 2.2

As a result of the thermal mismatch (26%), during cooling sapphire shrinks considerably faster than the GaN. This effect dominates the overall lattice/thermal mismatch and results in compressively strained GaN. This strain is symmetrical in-plane, resulting in what is known as biaxial strain. In this case the strain in the x-direction, ϵ_{xx} is equal to the strain in the y-direction, ϵ_{yy}.

In addition to the strain, defects are also formed near the substrate interface. These defects include threading dislocations, which have their own associated strain distributions. The predominant Burgers vectors for the edge, screw and mixed TDs in GaN are $\frac{1}{3}[11\bar{2}0]$, [0001] and $\frac{1}{3}[11\bar{2}3]$ respectively. Figure 2.12 shows a cross-sectional image of GaN on sapphire where the lines threading vertically from the substrate to the surface are TDs. Typically, the density of TDs in GaN ranges from $\times 10^8$ cm^{-2} to $\times 10^{10}$ cm^{-2}, which is considerably higher than for other III-V semiconductors [68].

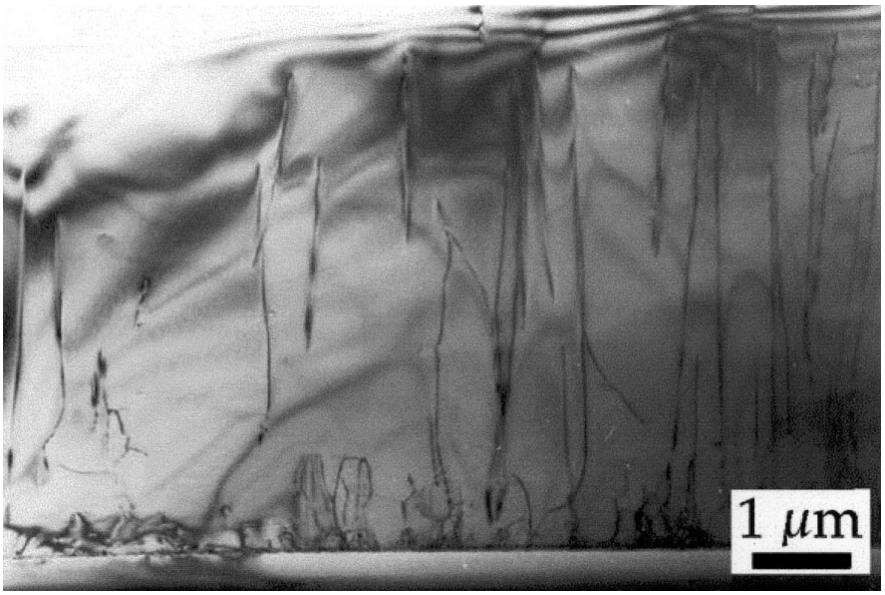

Figure 2.12: Cross-sectional TEM image of GaN on a sapphire substrate. Vertical lines threading from the substrate to the surface are threading dislocations. The small loops of dislocations near the substrate are known as misfit dislocations. Figure taken from [6].

The origin of TDs is still a point of contention in literature. One of the first explanations, supported by TEM studies [7, 69], was that TDs form at coalescence boundaries where the film may be heavily misoriented. Any twist (in-plane misorientation) at the boundary would lead to the formation of edge TDs to support the misorientation, while any tilt (out-of-plane misorientation) results in screw TDs forming [7, 69]. Combinations of tilt and twist would then result in mixed TDs [7, 69]. However, this idea has since been challenged by various other studies, some of which have access to better statistics via AFM measurements [70–73]. The study by Oliver *et al.*, for example, found no increase in TD density at coalescence boundary locations [70]. Some alternative explanations have been suggested, such as TDs developing from defects in the nucleation layer of GaN [74], and some studies have even suggested that formation at coalescence boundaries is in-fact growth condition dependent [75]. Still, ultimately, there is no current theory for TD generation that is unanimously accepted.

2.2 GaN-based Devices and Impact of TDs

The GaN thin films investigated in this thesis are suitable for use in high electron mobility transistor (HEMT) [76–79] and light-emitting diode (LED) [59,80–82] devices. However, the existence of TDs in GaN has a deleterious effect on the two most important characteristics that dictate the performance of GaN-based LED and HEMT devices. These characteristics are the carrier mobility for HEMTs and radiative recombination for light emission in LEDs. This section will discuss in more detail how TDs impede their performance.

2.2.1 Impact of TDs on Device Performance

For some time now, TDs have been known to be sources of non-radiative recombination for minority carriers in nominally undoped (n-type) GaN [8,9]. When TD spacing falls below the minority carrier diffusion length (the length a carrier travels, on average, before recombining), non-radiative recombination effects significantly impact the efficiency of the device. The minority carriers in n-type GaN are holes. The relative hole density near a dislocation can be given by:

$$p(r) = G\tau[1 - exp\frac{-r}{L_p}] \tag{2.29}$$

then the relative light emission efficiency can also be described by:

$$\eta = 1 - (\frac{2r_0}{L_d})^2 - \frac{8}{L_d^2}\int_{r_0}^{\frac{L_d}{2}} rexp(-\frac{r - r_0}{L_p})dr \tag{2.30}$$

where G is the generation rate of holes, r is the distance from the dislocation, r_0 is the 'dead zone' (the region around the dislocation where the minority carrier density is assumed to be zero), τ the hole lifetime, $L_d = N_d^{-1/2}$ is the mean separation of dislocations, N_d is the dislocation density and L_p the hole diffusion length in n-type GaN [8,9]. The consequence of this is that higher threading dislocation densities and/or lower threading dislocation spacing leads to reduced efficiencies. While density and spacing may seem directly correlated, the clustering of TDs must also be considered, as

thin films with low TD densities (TDDs) on the large scale may still suffer from regions of high clustering, and therefore low TD spacing, on the small scale.

Several suggestions exist throughout the literature as to why TDs act non-radiatively. Firstly, the presence of TDs has been correlated to regions of negative charge surrounding them [83, 84]. This has led to the suggestion that TDs produce 'trap states' [85]. These are intermediate states near the valence band which 'trap' carriers resulting in an increase in non-radiative recombination. Additionally, TDs are known to getter, or trap, point defects and impurities in their vicinity. These can also impact the electronic structure of GaN near the TDs [84].

The strain relaxation as a result of TD formation also causes local changes in the E field due to piezoelectric polarisation [86]. This produces local variation in the band gap, and as a consequence light emission. Any changes in band gap or band curvature will also be reciprocated in the effective mass of carriers (see Eq. (2.23)) and therefore carrier mobility. Reductions in carrier mobility via this mechanism are significant and can significantly degrade the performance of GaN based HEMT devices, requiring much larger gate voltages to produce higher carrier mobility [87].

Additionally, carrier mobility in HEMT devices can be further impacted by the Coulomb carrier scattering imposed by TDs [88, 89]. This scattering occurs due to the negatively charged areas surrounding the TDs. Both higher densities of TDs and lower carrier concentrations enhance the impact of this effect on carrier mobility.

2.3 Experimental Techniques and Analysis

2.3.1 Scanning Electron Microscopy

Scanning Electron Microscope Components

The scanning electron microscope (SEM) is a scientific instrument used for the imaging and quantitiative analysis of many different materials. It does so by scanning an electron beam over the surface of a material, producing signals such as backscattered electrons and x-rays (more on this in Section 2.3.1 *SEM: Beam-sample interaction*), which can then be measured by the user via a variety of detectors. Typical energies for the electron

beam in an SEM are between 1 keV and 30 keV, with currents in the nA range.

In general, an SEM is composed of three sections: an electron column, a specimen chamber (where any detectors will be located), and a corresponding computer used to control the experiment. The primary element of the electron column is the electron source. In modern-day SEMs, this is typically a tungsten filament, which emits electrons via thermionic emission or a field emission source (Schottky or cold field emission) [90]. Ideally, the electron beam produced by either of these mechanisms needs to be stable in current density and of a small diameter. Diffuse electron beams are much harder to converge/focus, resulting in reduced spatial resolution, while inconsistent current density can produce unwanted fluctuations in signal, increasing the noise of measurements. Once emitted, the electrons will pass through a series of electromagnetic lenses. This part of the optics can vary from microscope to microscope but generally involves a condenser lens, which initially converges the electron beam, followed by an objective lens, which converges the beam once more before interacting with the sample. Apertures can also be used between lenses to limit the divergence of the beam. Finally, the beam is scanned/rastered via charged scanning coils, which deflect the beam in the x and y directions. The electron column is held at vacuum to prevent the scattering of the electron beam from air or other impurities. The beam's characteristics, such as current, diameter, and energy/voltage, can be varied via the control computer. This computer also allows the user to optimise the beam, such as performing lens alignment, focusing the beam on the sample, and reducing astigmatism.

The specimen chamber is where the sample to be imaged/analysed is loaded by the user. This involves mounting the sample on a mechanical stage, which can be manipulated and moved below the beam either manually or electronically. Like the electron column, the chamber is also held at a vacuum; however, for samples that charge (high electrical conductivity), there are cases in which introducing a vapor to provide a low vacuum in the specimen chamber is beneficial. The chamber also houses the detectors operated by the user. For EBSD, this is typically a charged coupled device (CCD) or complementary metal oxide semiconductor-based (CMOS) detector coupled to a phosphor screen. Figure 2.13 shows a schematic of a basic SEM setup.

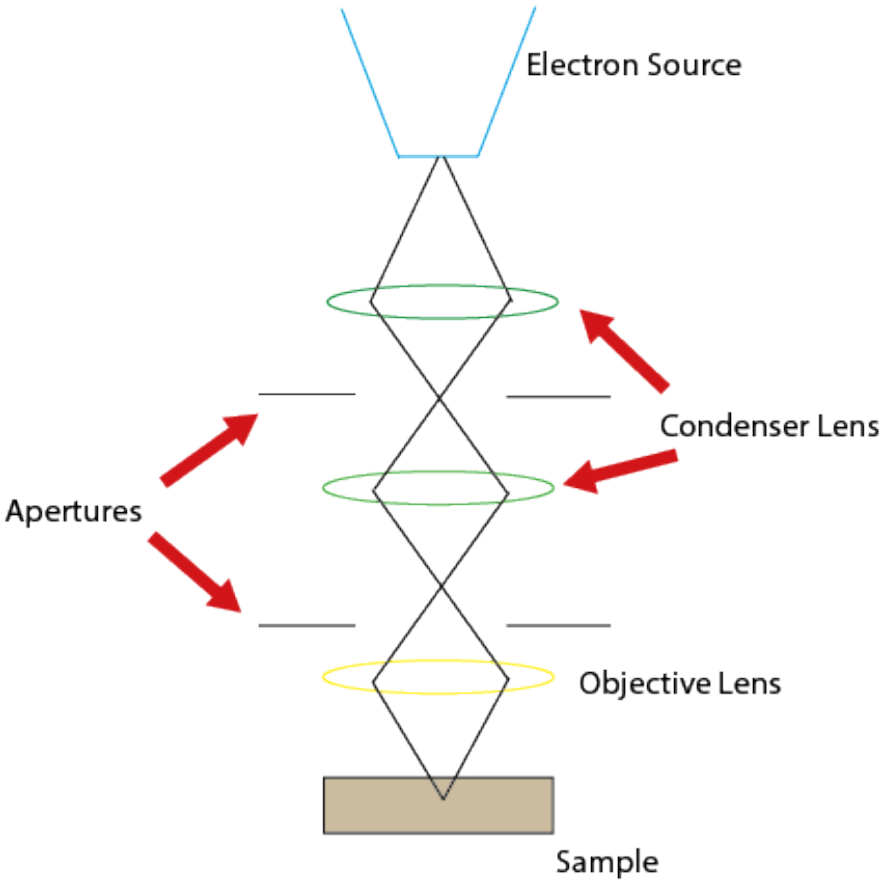

Figure 2.13: Schematic of a scanning electron microscope (SEM).

As well as providing control over the beam characteristic and microscope alignment, the control computer also facilitates the use of third-party software to sync detectors with the beam scan and control acquisition parameters for imaging.

SEM: Beam-sample interaction

Upon impacting a flat sample, beam electrons will penetrate the surface and undergo elastic and inelastic scattering processes. For elastic scattering, electrons undergo high-angle scattering due to the electrostatic interaction with atomic nuclei [90, 91]. This high angle scattering, for non-relativistic electrons, from an atomic nucleus is described by the differential Rutherford cross-section [91, 92]:

$$\Omega_R(\theta) = \frac{e^4 Z^2}{16(4\pi\epsilon_0 E_0)^2} \frac{d\Omega}{sin^4(\theta/2)} \tag{2.31}$$

Where e is the electron charge, Z is the atomic number of the sample/specimen, E_0 is the beam energy, θ is the scattering angle, and ϵ_0 is the permittivity of free space. This treatment is based on the assumption that scattering is purely elastic from atomic nuclei and that the atomic nuclei are at fixed positions and are so massive (relative to electrons) that they are unmoved during scattering. The Rutherford cross-section also ignores the wave behaviour of electrons. A more complete expression that does take this behavior into account requires wave mechanics which quickly becomes very complex and is unnecessary for the scope of this thesis. The Rutherford cross-section can be further modified for the screening effect of bound atomic electrons (effectively reducing the positive charge of the nucleus), and relativistic beam electrons to give [91]:

$$\Omega_R(\theta) = \frac{\lambda_R^4 Z^2}{64\pi^2 a_0^2} \frac{d\Omega}{[sin^2(\theta/2) + \frac{\theta_0^2}{4}]^2} \tag{2.32}$$

Where a_0 is the Bohr radius of the scattering atom, θ_0 is the screening parameter, and λ_R is the electron wavelength corrected for relativistic effects. For SEM beam energies, relativistic effects are an unnecessary consideration, however electron screening is an important consideration for when the beam electron is far from the atomic nucleus, resulting in lower angle scattering.

For inelastic scattering, variations on the Bethe expression for the ionisation cross-section can be used [91]:

$$\Omega_T = (\frac{\pi e b_s n_s}{E_0 E_c}) log(\frac{c_s E_0}{E_c}) \tag{2.33}$$

where n_s is the number of electrons in the ionised subshell, b_s and c_s are constants for that shell, and E_c is the ionisation energy. This, like the Rutherford cross-section, assumes electrons are non-relativistic and must be modified for relativistic electrons, such as those in high-energy transmission electron microscopy (TEM) measurements.

The region within the specimen where all of this elastic and inelastic scattering occurs is known as the interaction volume. The size of this volume is dependent on the beam diameter, but predominantly the beam energy and specimen density (ρ). The straight-line depth of the interaction volume (R_e) in microns can be described by the empirical formula from Kanaya and Okayama [93]:

$$R_e = \frac{0.0276A}{\rho Z^{0.889}} E_0^{1.67} \tag{2.34}$$

where A is the specimen's atomic weight. A corollary of this is that the further a beam electron travels into a specimen, the more likely it is to lose a significant amount of its energy. The model assumes that the beam is sufficiently focused such that its diameter plays no role in influencing the path of the electrons inside the material.

As well as elastic and inelastic scattering, diffraction effects can also occur. This happens when a beam electron is incident on a crystal plane of the material such that the Bragg condition for diffraction is fulfilled [94]:

$$2 d_{hkl} sin\theta_{hkl} = n\lambda \tag{2.35}$$

Where d_{hkl} is the interplanar spacing, θ_{hkl} is the Bragg angle for the particular plane (see Figure 2.14.), n is the order of reflection and λ is the associated De Broglie wavelength of the incident electron. As λ is dependent on the energy of the electron, it is therefore dependent on both the beam energy and the number of inelastic scattering processes before diffraction. Electrons of a particular wavelength have an associated

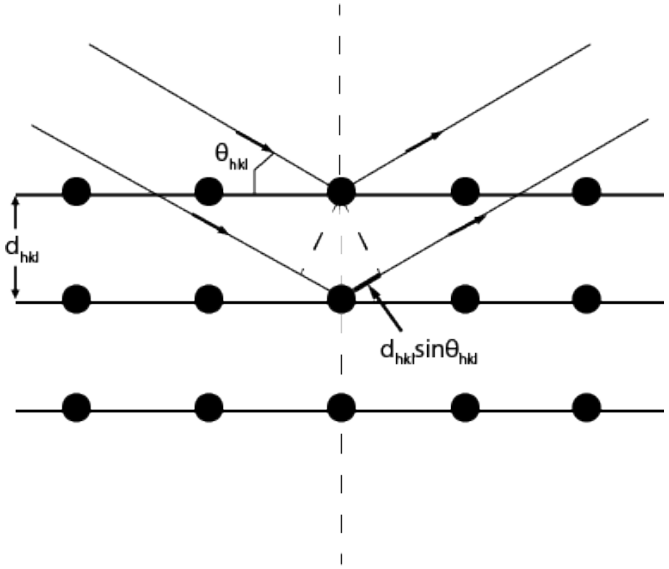

Figure 2.14: Bragg diffraction

wave vector, $\mathbf{k}$ given by:

$$\mathbf{k} = \frac{2\pi}{\lambda} \tag{2.36}$$

Upon incidence on a crystal plane at the Bragg angle (θ_{hkl}), the electron's outgoing wave vector after diffraction will be $\mathbf{k}'$ with a magnitude equal to its incoming wave vector $\mathbf{k}$ by the conservation of energy. For samples where the thickness is such that inelastic scattering does not dominate, diffuse scattering is significant. Diffuse scattering is the elastic, or quasi-elastic (i.e. very small loss of energy), scattering of electrons. These electrons will then have a variety of wave vectors $\mathbf{k}$. As such, when they are incident on a family of crystal planes at the Bragg angle (θ_{hkl}) and undergo diffraction, due to the cylindrical symmetry of the Bragg condition and variety of wave vectors, the electrons are diffracted not in lines but as a conical distribution. This is known as a Kossel cone [91]. For $\pm hkl$ two Kossel cones are generated.

The beam electrons that are scattered and/or diffracted such that they resurface and exit the specimen are termed *backscattered electrons* (BSEs). Other than these, there is a vast array of different types of signal produced in the interaction volume that can be collected and measured outside of the specimen in the SEM chamber. The majority of

this other signal is produced from the inelastic interaction of beam electrons with the sample. Examples include: bremsstrahlung x-rays produced with energy proportional to the loss of energy by beam electrons which interact with nuclei and lose momentum; secondary electrons (< 50 meV) ejected from the specimen by beam electrons; Auger electrons and characteristic x-rays which may be emitted when an atom ionised by the beam returns to its ground state; photons produced form the recombination of electron-hole pairs after excitement by the electron beam (cathodoluminescence).

2.3.2 Simulating Beam-Sample Scattering via Monte Carlo

A popular method of simulating the electron beam-sample scattering is via Monte Carlo simulations. These are statistical simulations of electron trajectories inside a material. A user-defined number of electrons with a specific initial energy are incident at a point on the surface boundary of the chosen material (imitating a point-like electron beam), and their paths and energies are then dictated by inelastic and elastic scattering models (such as the Rutherford and Bethe cross-sections outlined here). The paths of the electrons within the material are tracked until either their entire energy is absorbed via inelastic scattering or until the electrons are backscattered from the surface of the material. Materials are modeled as a sequence of horizontal planes, with their density dictated by either the atomic/weight fraction of each element appearing in the material's chemical formula or, if available, by the known density value for a given material in g/cm^3. In the Monte Carlo simulation software CASINO v2.42 [95] (used later in this thesis), the material is assumed to be homogeneous. Fig. 2.15 shows a Monte Carlo simulation run in the CASINO software for 1000 electrons at a beam energy of 20 kV inside a 900 nm thick GaN film.

Monte Carlo simulation programs for scattering processes such as CASINO do not, however, account for diffraction processes, meaning the simulation of electron trajectories is not complete. As such, BSE intensities and angular distributions are not adequately reproduced by Monte Carlo simulations [96]. Incorporating these diffraction processes, therefore, remains an important challenge in developing Monte Carlo simulations for EBSD [97–99]. However, Monte Carlo simulations *can* still be useful

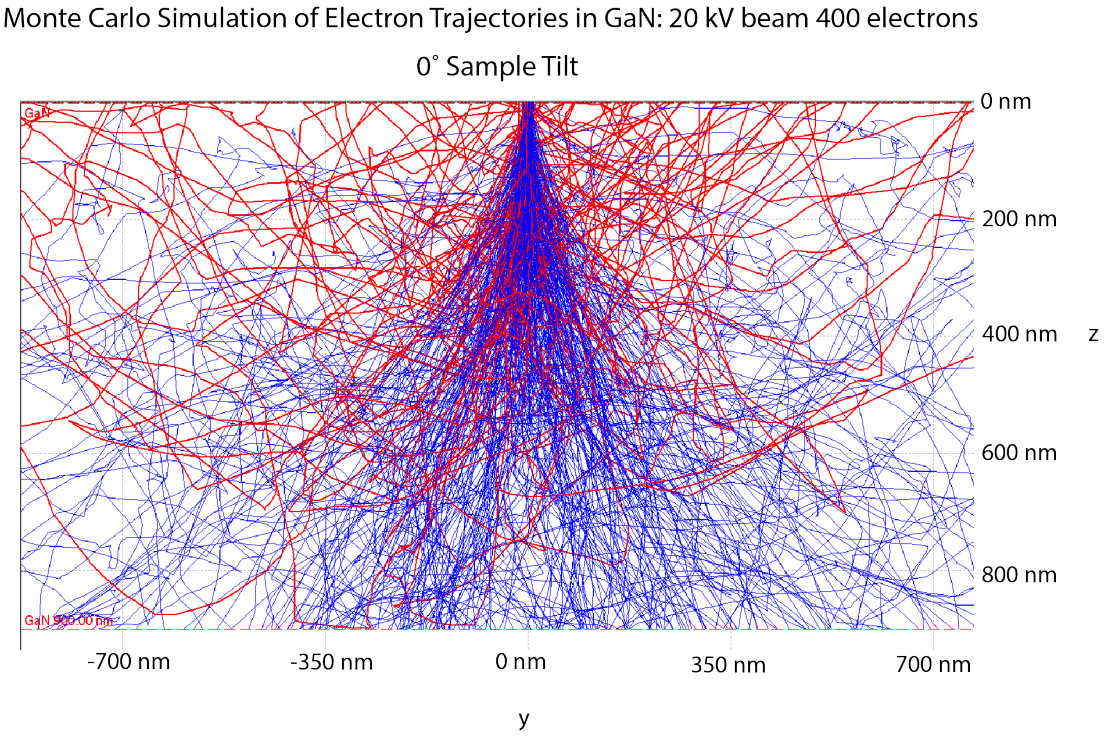

Figure 2.15: Monte Carlo simulation of electron trajectories produced in CASINO [95] using the Mott interpolated cross-section for scattering processes. In this case, the sample is normal to both the beam and the z-axis(no tilt). The trajectories of 1000 electrons simulated for a 20 kV electron beam in a 900 nm thick GaN film. Blue lines show the paths of electrons whose energy is fully absorbed by the material, and red lines show the paths of electrons that are backscattered and resurface from the material. The simulation is viewed in the yz plane.

in estimating a ball-park average depth for the electron distribution in a material as well as visualising the symmetry, or asymmetry, of the distribution of scattering electrons within the material. As long as the limitations of the simulations are understood, and the accuracy of depth calculations is treated with large enough error, there is still value in performing Monte Carlo simulations for general scattering processes related to EBSD.

2.3.3 Electron Backscatter Diffraction (EBSD)

Electron backscatter diffraction (EBSD) is a quantitative measurement performed in the SEM via the collection of backscattered beam electrons by a pixelated detector as the beam rasters across the specimen. This section introduces EBSD in two parts. Firstly, the scattered and diffracted electrons that make up the BSEs are treated as a whole, and the basic geometry and setup of EBSD is then explained. Not differentiating between diffracted BSEs and scattered BSEs at this point makes it easier to explain the general parts of EBSD that apply to both. In the second half of the section, the separate signals of scattered BSEs and diffracted BSEs will be explained by discussing the signal acquired by EBSD measurements- electron backscatter patterns (EBSPs).

EBSD: Geometry and Acquisition

The proportion of beam electrons which are backscattered from a material is described by the backscatter coefficient (η) [100]:

$$\eta = \frac{N_{BSE}}{N_B} \tag{2.37}$$

Where N_{BSE} is the number of backscattered electrons and N_B is the number of beam electrons incident on the specimen. While η will of course change with the atomic number Z of the material, it can also be optimised for any particular material by titling the sample stage in the SEM. This increases the proportion of backscattered electrons as the beam penetrate a shorter distance into the specimen. In fact, in EBSD, the SEM stage is generally tilted to 70°. While further tilting towards 90° would increase η even more, it also means the BSE signal comes from even closer to

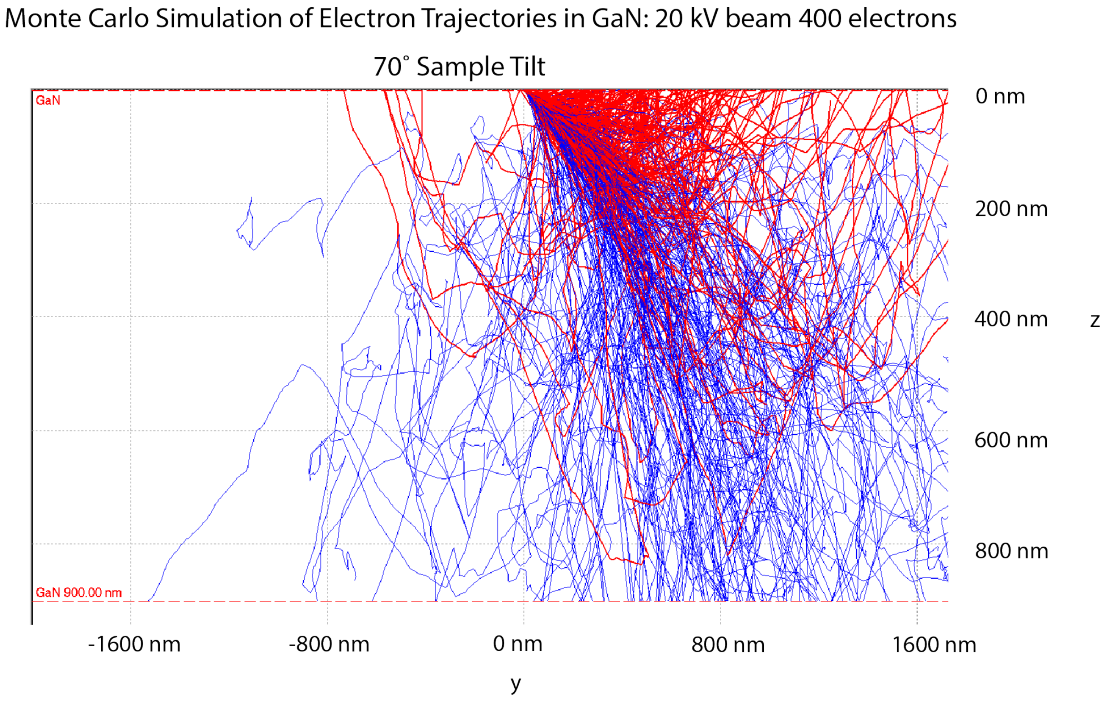

Figure 2.16: Monte Carlo simulation of electron trajectories produced in CASINO [95] using the Mott interpolated cross-section for scattering processes. The sample is tilted 70° around the horizontal, with the z-axis normal to the titled surface. The trajectories of 1000 electrons are simulated for a 20 kV electron beam in a 900 nm thick GaN film. Blue lines show the paths of electrons whose energy is fully absorbed by the material, and red lines show the paths of electrons that are backscattered and resurface from the material. The simulation is viewed in the yz plane. Due to the sample tilt, the interaction volume (region containing the beam electrons within the sample) is elongated significantly in the y direction.

the surface. This can result in topographical effects dominating the BSE signal with a lack of crystallographic information from within the sample. Figure. 2.16 shows a Monte Carlo simulation for the paths of 20 keV beam electrons incident on a tilted (SEM stage tilted 70°) GaN sample. The region of the GaN encompassing the incident electron paths is the interaction volume discussed earlier. The size of this interaction volume governs the spatial resolution of EBSD.

EBSD is performed with a set distance (step-size) between each point in the raster scan. Generally speaking, the smaller the step size, the better the spatial resolution of the resulting information, as there is greater sampling across the specimen. However, if the step size encroaches on the lateral size of the interaction volume, measurements

become subject to oversampling and reach a spatial resolution limit. Consequently, for optimal spatial resolution, on the first assumption, the interaction volume needs to be minimised. This can be done by reducing the beam energy and beam diameter when measuring a particular material. Moreover, the tilting of the SEM stage introduces an asymmetry in the interaction volume. This is in the form of an elongation in the tilt (y) direction. This can be easily seen by comparing the untilted Monte Carlo simulation (Figure. 2.15) with the tilted one (Figure. 2.16). Therefore, the lateral spatial resolution is also asymmetric, with better spatial resolution in the x-direction than in the y-direction. This is an important consideration when quoting lateral spatial resolution and also when simulating EBSD measurements.

At each point in the raster scan, the beam is dwelled for a user-defined time, and the BSEs are collected by a pixelated detector. This is typically a charged coupled device (CCD) or complementary metal oxide semiconductor (CMOS) device optically coupled to a phosphor screen. The phosphor screen acts as an intermediary between the BSE distribution and the camera sensor, converting the electron energy into light which can then be collected at the sensor. However, a fairly recent development is the direct electron detector (DED). This allows for the direct collection of BSEs and the most common DED in EBSD applications is the hybrid DED [101–103]. This is composed of a thin slab of semiconductor material (Si or GaAs, for example) which absorbs the energy of the incident electrons, producing electron-hole pairs proportional to this energy. These are then collected by electrodes and processed through an application specific circuit (ASIC) for readout. All work carried out in this thesis was with a CCD or CMOS phosphor detector.

The distribution of BSEs collected at the detector during each dwell in the raster scan is known as an electron backscatter diffraction pattern (EBSP). For a scan that dwells $M \times N$ times in an area A, an EBSD dataset will therefore have $M \times N$ EBSPs. The details of the BSE distribution, EBSP formation and the information which can be derived from EBSD will now be discussed in detail. Figure 2.17. shows the typical experimental setup for EBSD.

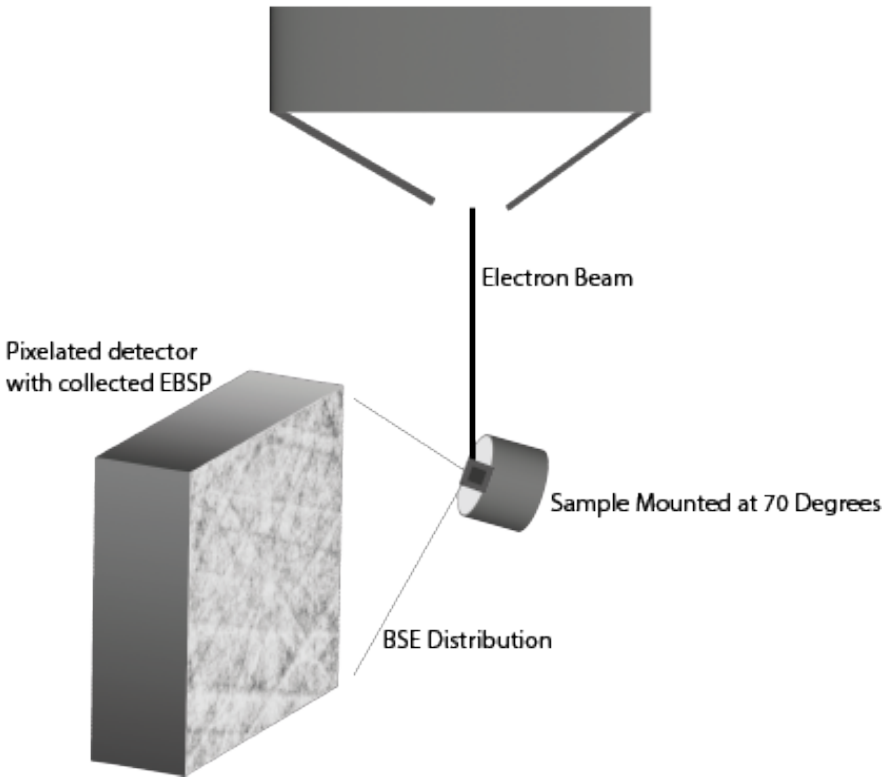

Figure 2.17: EBSD setup within the SEM. The sample is tilted to 70° for optimal BSE signal. A section of the BSE distribution is intersected by a pixelated detector. The resulting image from dwelling the beam at a particular point in the scan is an electron backscatter pattern (EBSP).

EBSD: Diffraction and Electron Backscatter Patterns (EBSPs)

An EBSP from GaN, produced with a beam energy of 20 kV in a Schottky field emission microscope is shown in Figure 2.18a). An EBSP is composed of two distinct parts: Kikuchi bands and a diffuse background. These parts have been separated from one another in Figure 2.18b) and c) by a fast Fourier transform for clarity. Kikuchi bands are pairs of lines formed from the outgoing diffraction of BSEs. They are the regions of the Kossel cones intercepted by the EBSD detector. They appear as lines because the solid angle of the Kossel cones covered by the detector is relatively small compared to the curvature of the cones. These lines/bands are, therefore, a 2D projection of the material's crystal planes, meaning an EBSP is closely related to a 2D projection of the material's crystal structure. The energy of the diffracted electrons forming these bands is typically within 3% of the beam energy [104]. The angular width of each Kikuchi band is two times the Bragg angle. This relationship between band width and Bragg angle means that lower beam energies will produce wider Kikuchi bands. Similarly, BSEs that have been strongly inelastically scattered and, therefore, are of significantly lower energy may have also been diffracted on their way out at wider angles, resulting in them contributing diffusely to the background. The other component of the diffuse background is all the other BSEs which have not been diffracted on their way out of the sample. The relative intensity of these BSEs is a function of the number of beam electrons which have been diffracted on their way *into* the material and do not resurface. The higher the proportion of incoming beam electrons diffracted, the fewer electrons there are that are being backscattered. Consequently, the diffuse background is still modulated by diffraction effects even if no diffraction information is directly derivable from the not-diffracted BSEs themselves. The diffuse background makes up the majority of the intensity in an EBSP, with Kikuchi bands accounting for around 10-15% of the overall intensity [105].

The intensities of Kikuchi bands in EBSPs have been successfully simulated and modelled using a Bloch wave approach to the dynamical theory of electron diffraction [98, 106, 107]. Understanding this is important for much of the underlying physics used in the pattern-matching approach to extract strain and misorientation information from

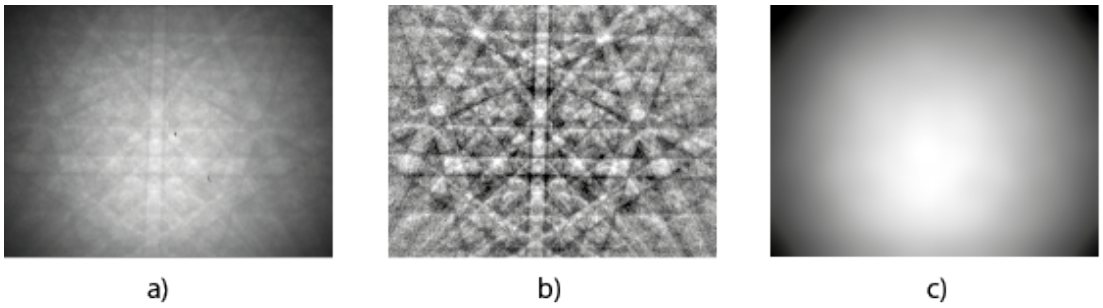

Figure 2.18: a) A raw electron backscatter pattern (EBSP) containing both a diffuse background a Kikuchi bands. A fast-Fourier transform has been used to decompose a) into just the signal from the Kikuchi bands, b), and just the diffuse background, c). b) is formed from the diffraction of low-energy-loss backscattered electrons from crystal planes on their way out of the sample, while c) is predominantly formed from inelastically scattered backscattered electrons with no direct diffraction information. The solid angle covered by an EBSD detector is typically $> 90°$, and for this particular pattern it is closer to $100°$.

EBSD datasets in this thesis (See Section 2.3.4 *Indexing*).

By understanding the probability densities of diffraction and elastic/inelastic scattering processes and their distribution within the crystal, it is possible to extrapolate how these processes are projected onto the EBSD detector screen. This involves careful consideration of the electrons' associated wavefunctions inside the crystal and the corresponding probability density at and between atomic positions. The wave function, ψ, inside a crystal can be given by the superposition of Bloch waves [94]:

$$\psi(\mathbf{r}) = \sum_j c_j \; exp(2\pi i \mathbf{k}^{(j)} \cdot \mathbf{r}) \sum_g C_g^{(j)} exp(2\pi \mathbf{g} \cdot \mathbf{r}) \tag{2.38}$$

Where $\mathbf{k}^j$ are the associated wave vectors of the Bloch waves and c_j and C_g^j are expansion coefficients. The wavefunction can be determined by solving for these (see [94]). It is fair to assume, given their high-angle scattering, that BSEs are predominantly scattered from atomic nuclei. The probability density of the wavefunction at the atomic positions in the crystal can be found ($\psi\psi*$). The dynamically backscattered intensity from depth t_1 to t_2 is then [94]:

$$I_{DYN} \propto \sum_{n,i,j} Z_n^2 B^{ij}(t_1, t_2) \sum_{\mathbf{g},\mathbf{h}} C_{\mathbf{g}}^{(i)} C_{\mathbf{h}}^{(j)*} \times exp(-B_n s^2) exp[2\pi i(\mathbf{g\text{-}h}) \cdot \mathbf{r}_n] \tag{2.39}$$

With atomic positions $\mathbf{r}_n$, atomic number Z, expansion coefficients $C_{\mathbf{g}}^{(i)}$ and $C_{\mathbf{h}}^{(j)*}$, Debye-Waller factors $exp(-B_n s^2)$ and a depth integrated interference term $B^{ij}(t_1, t_2)$ of the Bloch waves i and j. The EBSP can then be calculated using this intensity relationship for electrons with well defined wave vectors at each point in a crystal.

For a given scattering direction, a perhaps more intuitive but more general representation of this is to say that the observed intensity is simply the integral over all electrons scattered in direction (θ, ϕ) and subsequently diffracted out of the material with energies between the primary energy (beam energy), E_p, and a lower limit, often zero, across a depth from the surface to the maximum penetrated depth, t_{max} [94]:

$$I_B \propto \int_0^{E_p} dE \int_0^{t_max} dt \; D \; [n_B(\theta, \phi, \theta_{in}, \phi_{in}, E, t] \tag{2.40}$$

Where $(\theta_{in}, \phi_{in}$ is the incident beam direction, n_b is the initial distribution function of beam electrons, and D is an operator symbolising the diffraction process of these electrons.

The treatment involving Eq. (2.40) not only allows for EBSPs to be simulated but also for their intensity distribution to be understood. The high-intensity parts of the Kikuchi bands (their centres) correspond to regions in the crystal where the diffraction probability density coincides with areas of high diffuse scattering (atomic positions along crystal planes). Conversely, the low intensity parts of Kikuchi bands (their edges) corresponds to regions within the crystal where the diffraction probability density coincides with areas of low, or no, diffuse scattering (between atomic planes).

2.3.4 Indexing

As the Kikuchi bands in EBSPs are related to the crystal planes of the material, this allows crystal structure, misorientation and strain information to be extracted from an EBSD dataset. The extraction of crystal planes and their orientation relative to one

another from an EBSP is known as indexing. There are several approaches to doing this; two of these (Hough Indexing and Pattern Matching) will be explained in the following sections.

Hough Indexing

The first step to indexing is identifying the crystal planes present in an EBSP. This requires knowledge of the positions of the Kikuchi bands within an EBSP. Traditionally, the Hough transform has been used to do this [108]. This is related to the Radon transform [109], which will also be used in Chapter 6 of this thesis. The Hough transform is performed on the band signal only, with the diffuse background subtracted (as in Figure 2.18b)). In the Hough transform straight lines passing through each pixel (x_i, y_i) in the image, $I(x, y)$, are converted into 'Hough-space' via the parameterization [108]:

$$\rho = x_i cos\theta + y_i sin\theta \tag{2.41}$$

Where ρ is the distance from the origin and θ is the angle of the straight line normal. Consequently, a unique straight line in the image corresponds to a point in Hough-space (θ_i,ρ_i). So for every straight line passing through a point (x_i,y_i) in the image, a 'vote' is given in Hough-space. The accumulation of these votes along a Kikuchi band results in a strong intensity at a point in Hough space (θ_i,ρ_i). Figure 2.19. shows the conversion of Kikuchi bands in a filtered EBSP to intense points in Hough-space.

To relate the identified bands to the crystal structure, a transformation from the Cartesian detector reference frame to the crystal reference frame must occur. This involves rotating the Cartesian detector reference frame into coincidence with the Cartesian reference frame of the sample. The Cartesian basis vectors can then be converted to crystal basis vectors by application of a structure matrix, **A** [110]. This is then the origin from which orientation is measured. The further rotation required for the EBSP bands to match the exact lattice orientation at each point is generally described using Euler angles. Euler angles are three consecutive rotations around given axes such that two structures are brought into coincidence. These three rotations are known as *pitch*, *yaw*, and *roll*. In EBSD the Bunge convention [111] for Euler angles is most commonly

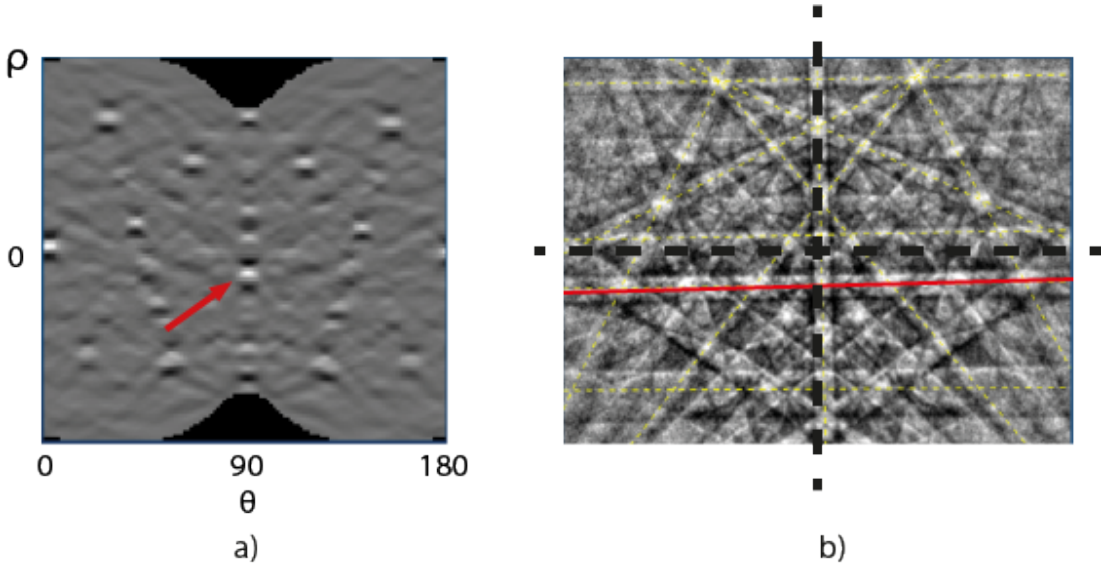

Figure 2.19: a) Hough-space corresponding to the filtered EBSP in b). Using the Hough transform, Kikuchi bands in b) are converted into points in Hough-space with parameters ρ (the distance of the band from the origin marked by the intersection of the two dashed lines) and θ (the angle of the line normal to the origin). The bright dot in a) identified by the red arrow corresponds to the Kikuchi band in b) marked by the red line.

used. This involves a rotation of ϕ_1 around the z-axis, a rotation of Φ around the x-axis and a final rotation of ϕ_2 around the new z-axis. This is more formally expressed as [110]:

$$\mathbf{O} = \mathbf{R}_{z(\phi_2)}\mathbf{R}_{x(\Phi)}\mathbf{R}_{z(\phi_1)} \tag{2.42}$$

Once in the crystal reference frame, angles between bands can be successfully calculated and compared to a list of theoretical interplanar angles for a given structure produced via kinematical structure factor calculations. These kinematical calculations are performed for reflectors (bands) with the highest intensities and the experimental data is subsequently fitted, finding the best solution for the orientations of the bands. For an EBSD dataset with $M \times N$ patterns spanning an area A, the misorientation from point to point is then simply found by comparing the relative orientations of the EBSPs at those points.

Pattern-Matching

The angular resolution of the basic Hough-based approach is limited, for high-speed implementations, to around 0.5° [112]. Moreover, when using detector binning of neighbouring pixels of the detector for lower resolution EBSPs and therefore faster operation and lower storage space- the angular sensitivity is reduced further. These limitations impose hurdles for the analysis of GaN where typical misorientations can often be below the 0.5° threshold. As such, the indexing used in this thesis is done via a pattern-matching approach developed by Aimo Winkelmann, as described in [113,114].

This approach generates dynamically simulated EBSPs at each point in the EBSD dataset for the given detector-sample geometry and crystal orientations output by the Hough transform which is typically calculated in commercial software. By using the Hough transform output as a starting point, the orientation parameters of the dynamically simulated patterns are then changed to maximise the normalised cross-correlation coefficient between each experimentally obtained pattern and the simulated patterns. The normalised cross-correlation coefficient is simply a measure of how similar two images are, with a value of 1 meaning the images are identical and 0 meaning the images share no similar features. The orientation of the crystal corresponding to a particular EBSP is then simply the orientation of the simulated pattern, which gives the highest normalised cross-correlation value. This approach has an approximate angular resolution of 0.03° and performs well at high pattern binning [114].

2.3.5 Deriving Strain from EBSPs

As with misorientation, strain (and therefore changes in lattice parameter) in a material results in a corresponding deformation of the EBSPs collected from that material (see 2.20). Earlier in this thesis, the concepts of deviatoric (change in shape) and hydrostatic (change in volume) strain were introduced. EBSPs are insensitive to hydrostatic strain. This is because hydrostatic strain, a change in volume, affects all normal strain components equally according to Eq. 2.10 and so there is no corresponding change in inter-planar angles on the EBSP pattern.

In order to measure the deviatoric strain, a relative approach is often taken where

an EBSP in a dataset is chosen as a reference, and the distortion of the other EBSPs with respect to this is calculated for the different strain and lattice rotation tensor components [12, 115–118]. Consequently, EBSD does not find absolute strain, but rather relative strain. The reference EBSP is generally chosen from a region in the dataset that is assumed to be minimally strained. However, it is unavoidable that there will be some residual strain in the pattern. Once the reference EBSP is chosen, it is subdivided into a user-defined number of regions of interest (ROIs). By comparing the translations/shifts ($\mathbf{q}$) of the features within the ROIs with respect to all other EBSPs in the dataset, the strain can be calculated. These shifts are related to the displacement gradient tensor ($\mathbf{a}$) via [115]:

$$\mathbf{q} = \mathbf{Q} - (\mathbf{Q} \cdot \hat{\mathbf{r}})\hat{\mathbf{r}} \tag{2.43}$$

where:

$$\mathbf{Q} = \mathbf{a}\hat{\mathbf{r}} \tag{2.44}$$

and $\mathbf{a}$ is the displacement gradient tensor:

$$\begin{bmatrix} \frac{\partial u_1}{\partial x_1} & \frac{\partial u_1}{\partial x_2} & \frac{\partial u_1}{\partial x_3} \\ \frac{\partial u_2}{\partial x_1} & \frac{\partial u_2}{\partial x_2} & \frac{\partial u_2}{\partial x_3} \\ \frac{\partial u_3}{\partial x_1} & \frac{\partial u_3}{\partial x_2} & \frac{\partial u_3}{\partial x_3} \end{bmatrix} \tag{2.45}$$

where $\mathbf{u} = (u_1, u_2, u_3)$ is the displacement at the position $\mathbf{x} = (x_1, x_2, x_3)$ in the sample, with the shift/translation $\mathbf{q} = (q_1, q_2, q_3)$ in the EBSP measured perpendicular to the direction $\mathbf{r} = (r_1, r_2, r_3)$ along the selected feature.

The magnitude of $\mathbf{Q} \cdot \hat{\mathbf{r}}$ is along the direction $\hat{\mathbf{r}}$ and therefore cannot be determined. However, combining the equations for the individual components of $\mathbf{q}$ gives the following simultaneous equations, which can be solved for different $\hat{\mathbf{r}}$ within the different ROIs to yield the strain and lattice rotation tensors [115]. Figure 2.20. shows the different types of EBSP distortion observed for each part of the deviatoric strain tensor.

$$r_1 r_3 [\frac{\partial u_1}{\partial x_1} - \frac{\partial u_3}{\partial x_3}] + r_2 r_3 \frac{\partial u_1}{\partial x_2} + r_3^2 \frac{\partial u_1}{\partial x_3} - r_1^2 \frac{\partial u_3}{\partial x_1} - r_1 r_2 \frac{\partial u_3}{\partial x_2} = r_3 q_1 - r_1 q_3 \tag{2.46}$$

$$r_1 r_3 [\frac{\partial u_1}{\partial x_1} - \frac{\partial u_3}{\partial x_3}] + r_1 r_3 \frac{\partial u_3}{\partial x_2} + r_3^2 \frac{\partial u_2}{\partial x_3} - r_1^2 \frac{\partial u_3}{\partial x_1} - r_2^2 \frac{\partial u_3}{\partial x_2} = r_3 q_2 - r_2 q_3 \tag{2.47}$$

The method used in this thesis for the determination of strain values shares many similarities to the one described above but incorporates the pattern-matching approach discussed in the previous section. For this approach, the simulated patterns are distorted not in their orientation parameters (as for the calculation of misorientation) but rather in their lattice parameters. For a wurtzite structure c and a are the parameters being distorted. By changing these parameters relative to one another, the simulated EBSPs are tetragonally distorted, and recognisable shifts within the patterns are visible [119, 120]. By simulating EBSPs with varying c/a ratios and maximising the normalised cross-correlation coefficient for each experimental EBSP, a best fit for the distortion is obtained. A simulated reference pattern is generated from an existing EBSP in order to incorporate the correct sample-detector geometry, and relative strain values are calculated with respect to this.

The ability to derive both relative orientation and strain from EBSPs makes EBSD an extremely useful technique for investigating the crystallography of semiconductor materials.

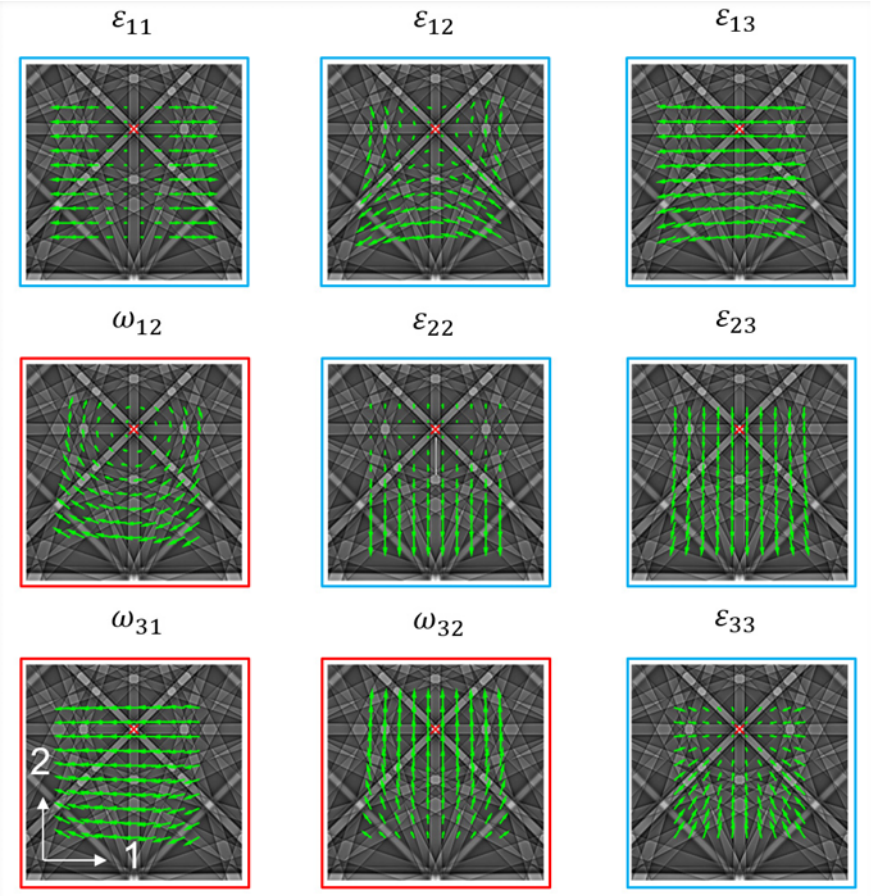

Figure 2.20: EBSP pattern distortion for the symmetric part of the strain tensor (e_{ij}) and the antisymmetric part of the strain tensor (w_{ij}). Figure taken from [118].

Chapter 3

Imaging Threading Dislocations

3.1 Introduction

Performing dislocation analysis for nitride semiconductors in the scanning electron microscope (SEM) has numerous benefits. Firstly, there is minimal sample preparation required. For many of the techniques performed in the SEM, samples do not have to be electron transparent, as with transmission electron microscopy (TEM). In addition to this, when imaging dislocations, the statistics are significantly greater than those in TEM cross-section measurements; i.e. one dataset simply includes a greater number of dislocations to be sampled. This is because large regions of the sample surface (e.g. 10 μm^2) can be imaged in a relatively short time (of the order of minutes) with high spatial resolution (40 nm for a 20 keV beam).

Alongside the quantitative orientation and strain information that EBSD can provide, it is imperative to have images of the threading dislocations themselves. By obtaining these, the user has the ability to quickly determine TD densities, which have direct implications on carrier mobilities and non-radiative recombination (see Section 2.1.7 *Strain and Threading Dislocations in GaN*), and analyse TD distributions which can have significant local variations and as such impose large local differences in device properties. Images of TDs can also aid identification of TD types present, which can be extremely useful for investigating the individual electronic properties of dislocation types which is still somewhat disputed in literature [121].

Traditionally, in the SEM, images of threading dislocations have been acquired with electron channelling contrast imaging (ECCI) which uses back- and/or forescatter diodes (BSDs, FSDs) to acquire images [12, 14, 122–136]. This is done by monitoring the change in the scalar intensity of the backscattered electron yield as the electron beam scans continuously over the sample surface. Threading dislocations will be observable if the sample is placed such that the electron beam is incident on crystal planes of the sample at close to the Bragg angle, the condition for Bragg diffraction, which will influence the elastic and inelastic scattering of the incident electron beam inside the sample. In this condition, known as a 'diffraction condition', any change in crystallographic orientation or lattice constant due to strain will produce a change in the proximity to the local Bragg angle, and correspondingly a change in the BSE yield based on the diffraction effects. In ECCI images, TDs generally appear as dots with black-white contrast.

Rather than using individual hardware diodes, a pixelated detector can be utilised to image dislocations. At each point on the sample where the beam is dwelled, rather than simply collecting a scalar intensity with individual diodes, an angular distribution of backscattered electrons in the form of an EBSP is collected. Despite the lack of direct crystallographic diffraction features in the diffuse background, the total yield and the large-scale angular distribution of the background electrons is, however, modulated by the diffraction effects of incident beam electrons, as explained previously (see Section 2.3.3 *Electron Backscatter Diffraction*).

A pixelated detector has much greater versatility than a diode for sample surface imaging. Firstly, the detector can be segmented via post-acquisition image processing techniques, to produce diode-like images, from anywhere across the pixel array. Here, the scalar intensity change of the BSE yield is simply monitored in specific, user-defined areas on the pixelated detector as the electron beam moves from point to point on the sample [137–143]. This method is known by various names, including virtual FSD, hybrid FSD, synthetic BSE, pattern region of interest analysis system (PRIAS) or EBSD dark field imaging mode using a virtual aperture; and here it is simply referred as virtual diode (VD) imaging. In doing this, a diode is effectively

moved around in the SEM chamber, which means images of the same area with differing dominant contrast mechanisms can be produced [140, 142–145]. Another benefit of using a pixelated detector is that changes in the distribution of the BSE yield can be monitored in these user-defined regions. This is done by treating the intensity distribution as a mass density and monitoring the changes in the x and y positions of this mass density as the electron beam scans from point to point on the sample. This is known as centre of mass (COM) imaging [105, 142]. VD imaging, based on the angular distribution of backscattered electrons, can also be carried out in a differential mode, by observing the relative ratio of intensities in different virtual diodes. Using three virtual diode intensity ratios, orientation colour contrast can be produced from polycrystalline materials [146]. Moreover, for multiphase materials, where neighbouring phases may have a high enough variation in electron scattering effects, large COM shifts may be measurable such that compositional changes are detectable. This could be particularly useful in geological applications of EBSD.

In this chapter, results are presented from performing VD imaging on an N-polar GaN thin film by using a pixelated detector with the sample placed in a diffraction condition. For the same sample and diffraction condition, the VD-like detector segmentation is then combined with COM imaging, exploring the combined imaging technique of VDCOM. For both VD and VDCOM imaging, separate images from the same sample area are produced showing either threading dislocations or threading dislocations and surface steps. The underlying physics behind the signal produced in these images is discussed. The ability to controllably produce images showing both surface steps and threading dislocations allows one to identify whether threading dislocations terminate a step and therefore have a screw component or alternatively do not terminate a step and are therefore edge dislocations [22]. The suitability of both techniques for imaging dislocations and surface steps is also compared, where it is illustrated that VDCOM produces consistent signal-to-noise across both dislocation and surface step and dislocation images, whereas VD imaging does not due to signal-to-noise issues inherent in the sample-detector geometry of the experimental setup. The applicability of VDCOM imaging is then demonstrated across a range of other nitride thin films, each exhibiting

different dislocation and step densities. Finally, for a Ga polar sample, VDCOM and ECCI are compared.

3.2 Materials and Acquisition

The N-polar GaN sample is a 900 nm thick N-polar GaN thin film grown by metal-organic vapor-phase epitaxy (MOVPE) on a sapphire substrate. The N-polar GaN was induced by high temperature (1150 °C) nitridation in an environment of ammonia and H_2, followed by an estimated 25 nm thick low temperature (525 °C) GaN nucleation layer and a 900 nm thick high temperature (1150 °C) N-polar GaN layer. This sample was provided by the University of Sheffield.

There are three Ga-polar samples used in this chapter. The first is a 1600 nm thick thin film grown on a *c*-plane sapphire substrate via MOVPE. A 30 nm GaN nucleation layer was grown at 525 °C. This layer was annealed briefly at a temperature of 1023 °C prior to the epitaxial growth of the sample. More information on the growth process is available in [147]. This sample was used in previous collaborations with the growers at the University of Sheffield. The second Ga-polar sample is a 2150 nm thick GaN thin film grown by MOVPE on a commercial AlN template from Kyma Technologies. The template consisted of a 50 nm thick nanocolumnar crystalline AlN nucleation layer grown epitaxially by plasma vapor deposition onto a sapphire substrate. The growth temperature for the GaN layer was 1060 °C with H_2 as the carrier gas. TMIn was used as a surfactant. This sample was used in previous collaborations with the growers at the University of Bath. The third (used for the ECCI comparison) is a sample provided by the University of Cambridge grown on sapphire using a 2D-3D growth method similar to that found in [70].

The AlN sample is a 6.6 μm thick thin film overgrown on a nanopatterned sapphire substrate (nPSS) with a miscut of 0.1° towards the sapphire *m*-plane. The overgrowth was performed in planetary MOVPE reactor with a constant reactor pressure of 50 mbar and H_2 serving as a carrier gas. More details on the nPSS fabrication and the AlN overgrowth process can be found in [148]. This sample was used in previous collaborations with the growers at the University of Bath.

All EBSD datasets were acquired using a variable pressure field emission gun SEM (FEI Quanta 250) equipped with an Oxford Instruments Nordlys EBSD system with a sample tilt of 70°. The beam voltage for the N-polar GaN sample and AlN sample was 20 kV with a map step size of 30 nm and 55 nm, respectively. The beam voltage used on the other two GaN samples was 30 kV with a map step size of 25 nm. All image processing was performed on raw, as-acquired EBSPs, i.e. no diffuse background removal was used for any of the image processing techniques.

3.3 Virtual Diode Imaging

The virtual diode technique is a post-acquisition image processing technique that effectively segments a pixelated detector, such as an EBSD detector, into smaller 'virtual' diodes. In this case it was performed and developed using image processing code written in Python. After collecting a full dataset of EBSPs spanning an area of the sample, the user can define the same small region on each EBSP where the change in intensity can be monitored, going from one EBSP to the next (i.e. effectively moving across the sample). A simple example of this is as follows. A dataset contains $M \times N$ EBSPs, spanning an area on the sample surface. The EBSPs were binned down into 7×7 arrays from their original resolution of 256×336. By segmenting into seven rows, the virtual diode can be 'moved' up and down the screen, collecting signal from different depths in the sample with the rows containing enough intensity that the final image has relatively good signal. After doing this, a particular row was selected and the intensity within that row was summed to a single scalar value. This was performed for all EBSPs in the dataset. By then plotting each scalar value for each EBSP in the dataset in an array, a virtual diode image was obtained. The steps for this are illustrated in Figure 3.1. This process can be repeated for the other six rows, obtaining seven virtual diodes in total.

The value of using this virtual diode method is that one effectively moves a diode up and down in the chamber and image from different locations. By doing this one can take several images with one dataset where each image may have different features, such as crystallographic or topograhical features, dominating the overall contrast. This happens because as the BSE yield is explored in different areas in the BSE distribu-

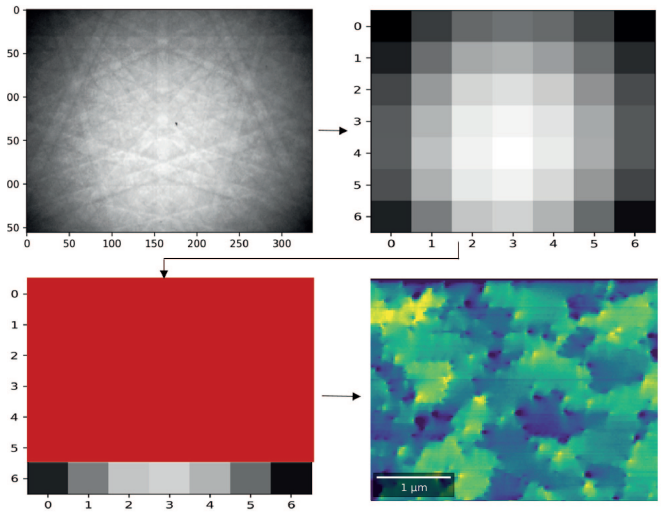

Figure 3.1: Work flow of virtual diode processing method. Each EBSP in a dataset is binned into a smaller array (here 7×7). The bottom row is then chosen and the intensity is summed across the same row for all EBSPs, generating as many scalar intensity values as there are EBSPs. These values are then plotted giving a resulting image of the sample surface.

tion, a signal from different depths within the sample is collected. The effect of how sample depth information is related to detector position is explored in [144]. The contrast recorded with different virtual diodes is heavily dependent on sample topography, detector-sample geometry and electron beam voltage [105].

It is important to note that VD images can be formed from an area of any size or shape, or even single pixels, in the as-acquired EBSPs. However, as the area of the EBSP sampled becomes smaller, the signal-to-noise ratio (SNR) reduces, affecting the clarity of the resulting VD images.

The virtual diode method was performed on the N-polar GaN sample by segmenting the screen into 20 rows and summing the signal in each row for each EBSP. 20 rows were chosen in this case as they maximised the variation in contrast observed. Shown in Figure 3.2 are the VD images acquired from the top row (a) and the bottom row (b) of the N-polar GaN sample. The top and bottom rows demonstrate best the variation between VD images in terms of dominant contrast.

The virtual diode images initially showed dark horizontal lines, unrelated to crystallographic changes in the sample. This was potentially caused by either sample charging

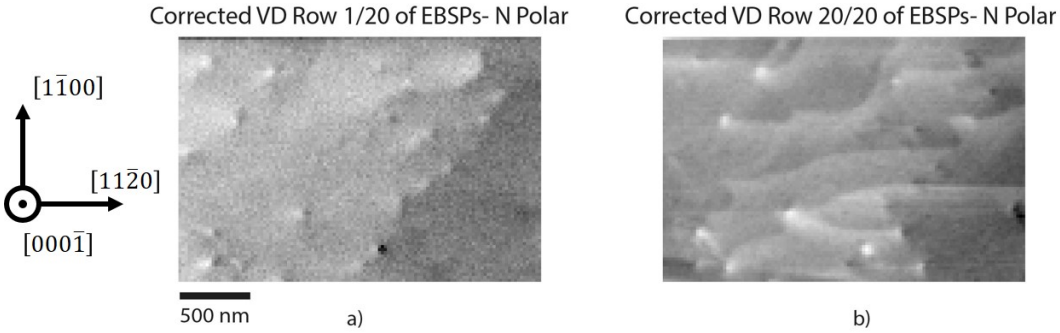

Figure 3.2: a) VD image produced from monitoring intensity changes in the top 5% of rows in EBSPs for N-polar GaN sample. b) VD image produced from the bottom 5% of rows in EBSPs for N-polar GaN sample. These images have been corrected for unwanted signal changes via the application of a median function to the VD dataset (see Supplementary Information).

or fluctuation in the beam current. This was consistent across all the VD images much like a watermark. This was corrected for by taking the median value of each pixel across the dataset and subtracting the result from each image in the dataset. This removed the features common to each image in the dataset (the horizontal lines). The corrected images are those shown in Figure 3.2.

Inspecting the VD image produced from the intensity distribution in the top row (Figure 3.2a)) shows that mainly dislocation contrast is observed, dots with black-white contrast on the sample surface. This is due to the same effect as discussed for ECCI previously, where changes in crystallographic orientation result in a change in the proximity of the incident beam to the Bragg angle; meaning fewer or greater number of electrons are diffracted through the sample.

Figure 3.2b) shows contrast which is dominated more by the surface steps on the sample. The dislocations which terminate these steps also show strong contrast as they are at the interface between the steps and the rest of the sample, while dislocations that do not terminate steps are fainter than in Figure 3.2a). The signal due to topography is now exceeding the signal due to changes in orientation of the crystal. To understand why this change in contrast occurs between the top and bottom row we must consider the detector-sample geometry of the setup (Figure 3.3a)). With the sample inclined at 70° to the horizontal, the electrons incident on the bottom of the screen are at a

grazing angle to the sample, making them more surface sensitive. These electrons are shadowed by the atomic steps, resulting in changes in the BSE yield.

Additionally, it can be seen in Figure 3.2 that the signal-to-noise in row 1/20 is less than that in row 20/20. This is also as a result of the geometry. As the sample is inclined, the volume of beam electrons within the sample (known as the interaction volume) is elongated in the sample y direction [94]. As such, electrons will favour the forward direction when exiting the sample [142], leading to an asymmetry in the BSE yield going down the detector screen. This can be confirmed by plotting a graph of the intensity recorded in each pixel row of the detector (Figure 3.3b)). This effect could be reduced by lowering the screen to increase electron incidence at the top of the screen and improve the signal, however as can be inferred from the shape of the distribution, this may mean less signal elsewhere on the screen.

3.4 Centre of Mass Imaging

While VD imaging monitors the changes in the intensity of the backscattered electrons incident on regions of interest on the detector, other characteristic properties of the angular distribution of the electrons on the pixelated detector can also be monitored [105, 142, 149]. For example, the position of the centre of mass of the BSE intensity distribution ($\mathbf{r}_{COM}$) is found for each EBSP using:

$$\mathbf{r}_{COM} = \frac{1}{\Sigma_P I(x_p, y_p)} \begin{pmatrix} \Sigma_N \; x_N \cdot I(x_N, y_N) \\ \Sigma_M \; y_M \cdot I(x_M, y_M) \end{pmatrix} \tag{3.1}$$

Where $I(x_p, y_p)$ is the intensity measured at pixel P. The x and y coordinates of each pattern's COM are stored in two separate arrays, one for x values and one for y values. These arrays are normalised by simply subtracting their mean value from each element contained in them. For a dataset with $M \times N$ EBSPs, there is then $2 \times M \times N$ values. The two separate arrays are then plotted, producing COMx and COMy images, respectively (Figure 3.4).

As with VD imaging, it is demonstrated here that the EBSPs can also be segmented for COM imaging (VDCOM), providing images with different dominant contrast mech-

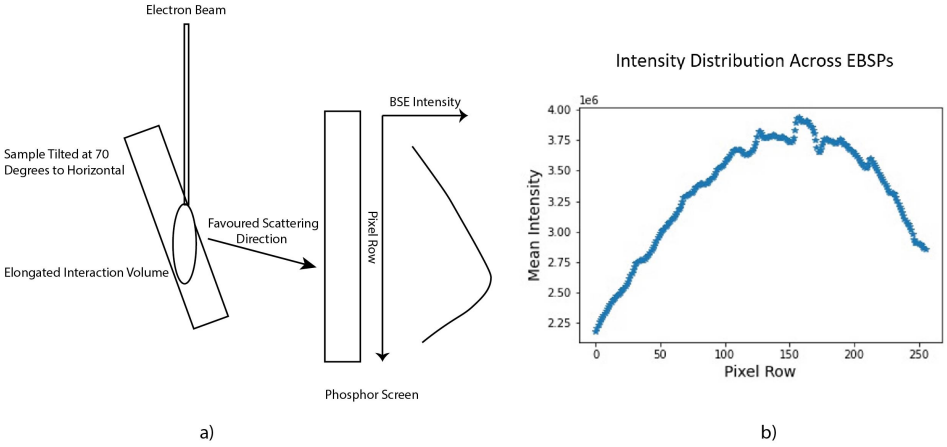

Figure 3.3: a) Effect of sample tilt on interaction volume is shown. Due to 70° tilt the interaction volume is elongated in the y direction resulting in an asymmetrical backscattered electron intensity distribution on the phosphor screen of the detector. This distribution shows the forward direction is favoured by electrons exiting the sample surface. b) Distribution of BSE signal from the first pixel row to the last on the detector.

anisms from one EBSD dataset. For example, COM analysis can be performed for the upper half and the lower half of each EBSP resulting in four VDCOM images. However, unlike traditional VD imaging, where binning can be high, it is important to understand that for higher binning for VDCOM imaging, smaller changes in the COM position are much less detectable. This can mean that shifts in COM images smaller than the resolution of the highly binned diodes are not detected and the resulting VDCOM images, therefore, show less contrast where a dislocation/crystal distortion is present. It is also important to note that as with VD imaging, the contrast obtained by VDCOM imaging when using a particular section of the EBSPs is strongly dependent on sample-detector geometry, surface topography and beam energy [142]. This is outlined in the following sections where an explanation for the observed VDCOM images is given for the particular detector geometry, sample and beam energy used in acquiring the N-polar GaN thin film dataset used in the present chapter.

3.5 Virtual Diode Centre of Mass Imaging

The following subsections '*VDCOMy*' and '*VDCOMx*' describe in detail the contrast exhibited from using VDCOM imaging on the N-polar GaN thin film sample.

The explanation for the contrast revealed in each image is particular to the sample-detector geometry, sample topography and beam energy used in this research. The explanation cannot be applied for every instance of VDCOM imaging where one or more of these variables changes. Both VDCOMy and VDCOMx did not exhibit the horizontal lines the VD method did. This is because unwanted changes in the incoming beam current should not affect the position of the COM of the outgoing BSE distribution, highlighting an important advantage that COM imaging has over VD imaging.

3.5.1 VDCOMy

VDCOMy images were plotted by segmenting each EBSP into a top half and a bottom half. This gives two virtual diode regions per EBSP. The centre of mass/intensity was then calculated as described previously for the top half and bottom half of the EBSPs

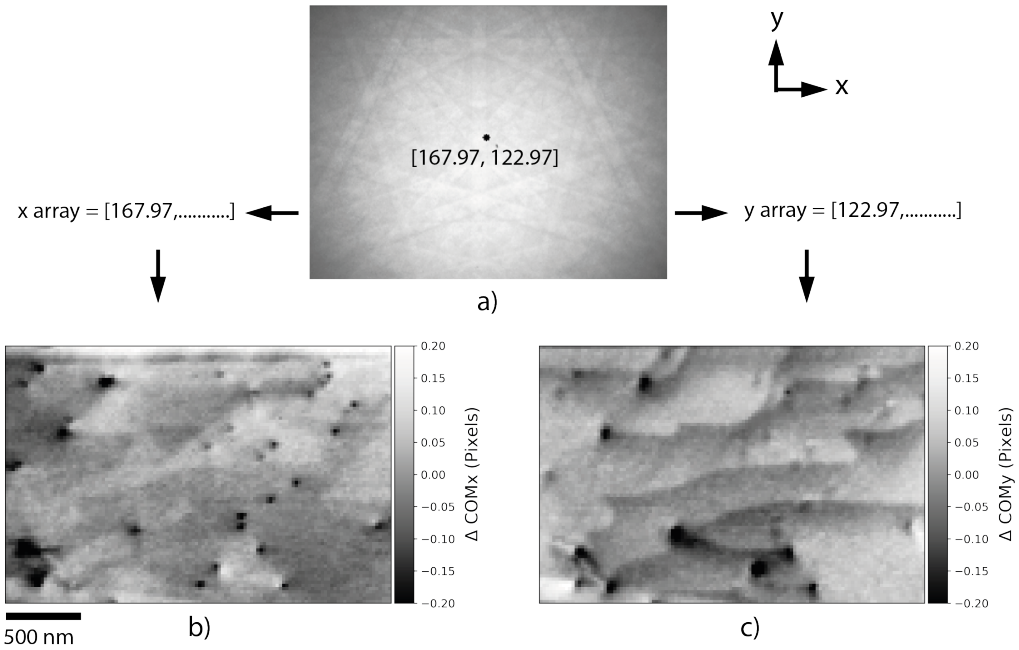

Figure 3.4: COM imaging. The centre of the intensity distribution of each EBSP is found for COM analysis and is marked by the black dot in the example EBSP, a). The x and y coordinates of the COM for every EBSP are plotted in two separate arrays and normalised by the mean value. These arrays are plotted giving COMx (b) and COMy (c) images respectively. Note here there is no detector segmentation, the COM images are produced from the COM of the entire EBSP. The images shown are from the 900 nm thick N-polar GaN sample.

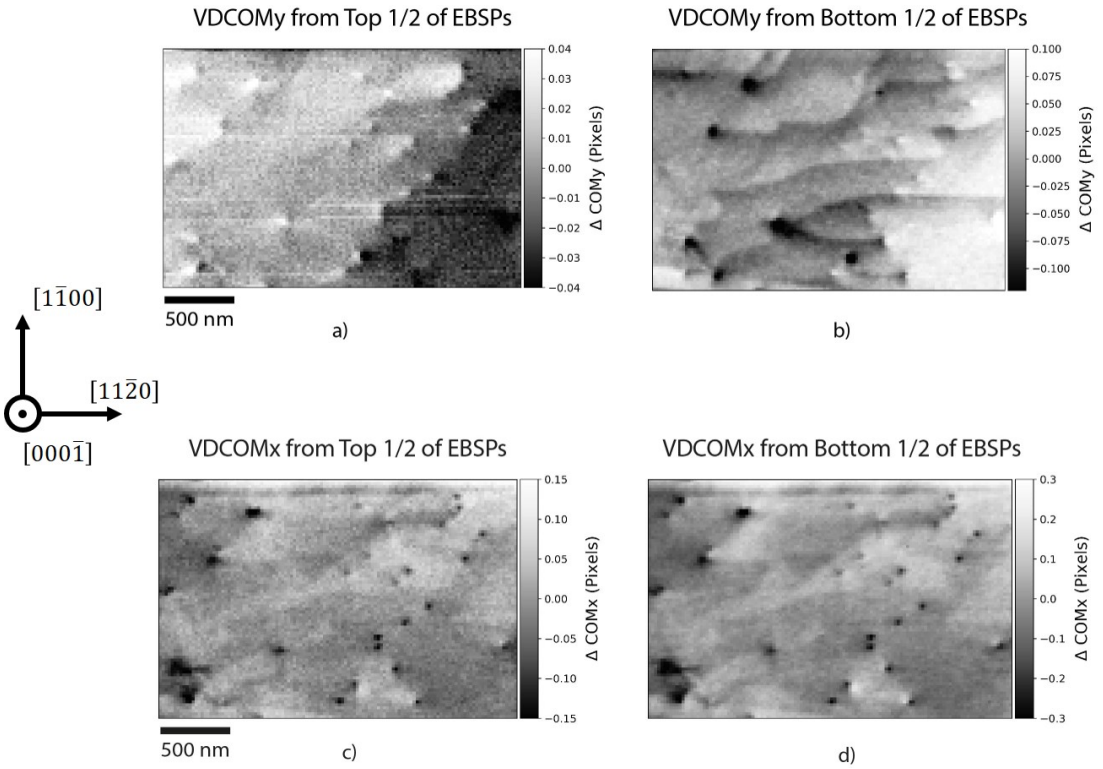

Figure 3.5: VDCOMy image produced from the a) top half and b) bottom half of EBSPs in the N-polar GaN dataset. VDCOMx image produced from the c) top half and d) bottom half of EBSPs in the N-polar GaN dataset.

separately. The deviation in the y position of each centre of mass value from the mean was then plotted for both subsets of data, giving two images: VDCOMy from the top half of all EBSPs and VDCOMy from the bottom half of all EBSPs (Figure 3.5).

Inspecting both VDCOMy images (Figures 3.5a) and b)), we see that the signal produced is very similar to that in the VD images (Figure 3.2). Again where there are dislocations, the BSE yield will vary and so the shape of the outgoing distribution will change. The direction in which the outgoing electrons are scattered and diffracted will also change as the orientation of the the crystal changes near dislocations. Both result in change in COMy.

Furthermore, for the VDCOMy produced from the bottom half of EBSPs, the image is formed from those electrons scattered at a grazing angle, meaning the contrast is particularly surface sensitive. When the beam scans in close proximity to steps, the electrons leaving the sample with grazing incidence will travel through a slightly

greater depth to escape the sample. This results in a small shift in the y component of their backscattered direction, producing contrast in the resulting VDCOMy image. Additionally, any shadowing due to surface steps may cause a change in the BSE distribution shape, and correspondingly a change in the COMy position.

3.5.2 VDCOMx

As with the VDCOMy images, the VDCOMx ((Figures 3.5c) and d)) images resulted from segmenting each EBSP into a top half and a bottom half.

There was significantly less variation in the dominant contrast mechanism for each VDCOMx image. In fact, surface steps were largely absent. Additionally, many of the dislocations were resolved as smaller dots, in contrast to the spots with clear black-white contrast in the VDCOMy images. This made it easier to discern the number of dislocations present in the sample area, as some dislocations are very close to one another. The contrast is consistent with expectations, as COMx analysis is generally less sensitive to topography [105]. In the case of the surface steps observed in the sample and geometry used, the absence of surface steps in VDCOMx could possibly be explained by the fact that changes in the position of the BSE distribution in the x direction occur only due to shadowing. This is not the case for VDCOMy where changes in the COMy position occur due to the fact that electrons with grazing incidence are backscattered in the y direction slightly more when exiting near a step.

3.6 VD and VDCOM Suitability for Threading Dislocation Imaging

When inspecting the quality of images produced by VD and VDCOM methods, their suitability for imaging dislocation distributions in nitride thin films can be assessed. For the VD method, it is only possible to produce images showing only dislocations by placing the virtual diode at the top of the screen for this particular experimental setup (Figure 3.2a)). Due to the sample detector geometry, this means that unfortunately, signal-to-noise is poor in these images, resulting in a fairly low-quality image of the

dislocation distribution. While the detector screen could physically be moved inside the SEM chamber to improve the signal-to-noise at the top of the screen, the asymmetry of the BSE distribution would mean there would be less signal at the bottom of the screen, deteriorating the surface step images. This however is not an issue with VDCOM imaging, as the insensitivity to surface steps that VDCOMx exhibits here means that images from the bottom of the screen are obtained with high signal and high dislocation contrast, while reducing the effect of topography (Figure 3.5c)). The dislocations also appear as small black dots, making them easily resolvable from one another, as opposed to the strong black-white contrast in the VD image showing just dislocations. While this shows a clear advantage of using VDCOM over VD, VD does have greater versatility in that VD images can be formed from small areas of the detector. This means there is greater flexibility in where the virtual diode can be placed when monitoring intensity changes, compared to monitoring the change in position of the distribution, which requires a large enough area that these changes are detectable. However, for this particular case, VDCOM is clearly superior to VD imaging in the range and quality of images it can produce.

3.7 VDCOM Applicability for Other Nitride Thin Films

Here the applicability of VDCOM across three other nitride thin films, exhibiting a range of dislocation densities, is investigated. Figures 3.6 a)–c) show VDCOMy images produced from the bottom half of EBSPs for two different Ga-polar GaN thin films and an AlN thin film, respectively. VDCOMy images were chosen as they exhibit contrast from both steps and dislocations in these samples. The dislocation densities are 3×10^8 cm^{-2}, 2×10^9 cm^{-2} and 1×10^9 cm^{-2} for a), b) and c) respectively. For comparison, the dislocation density for the N-polar sample discussed earlier is of the order of 1×10^8 cm^{-2}.

Inspecting the images for the two GaN films (Figures 3.6a) and b)), it becomes possible to understand the limitations on imaging GaN thin films with the VDCOM technique. Surface steps can easily be identified in Figure 3.6a), although where they terminate is less clear than that in Figure 3.5b), meanwhile individual dislocations are

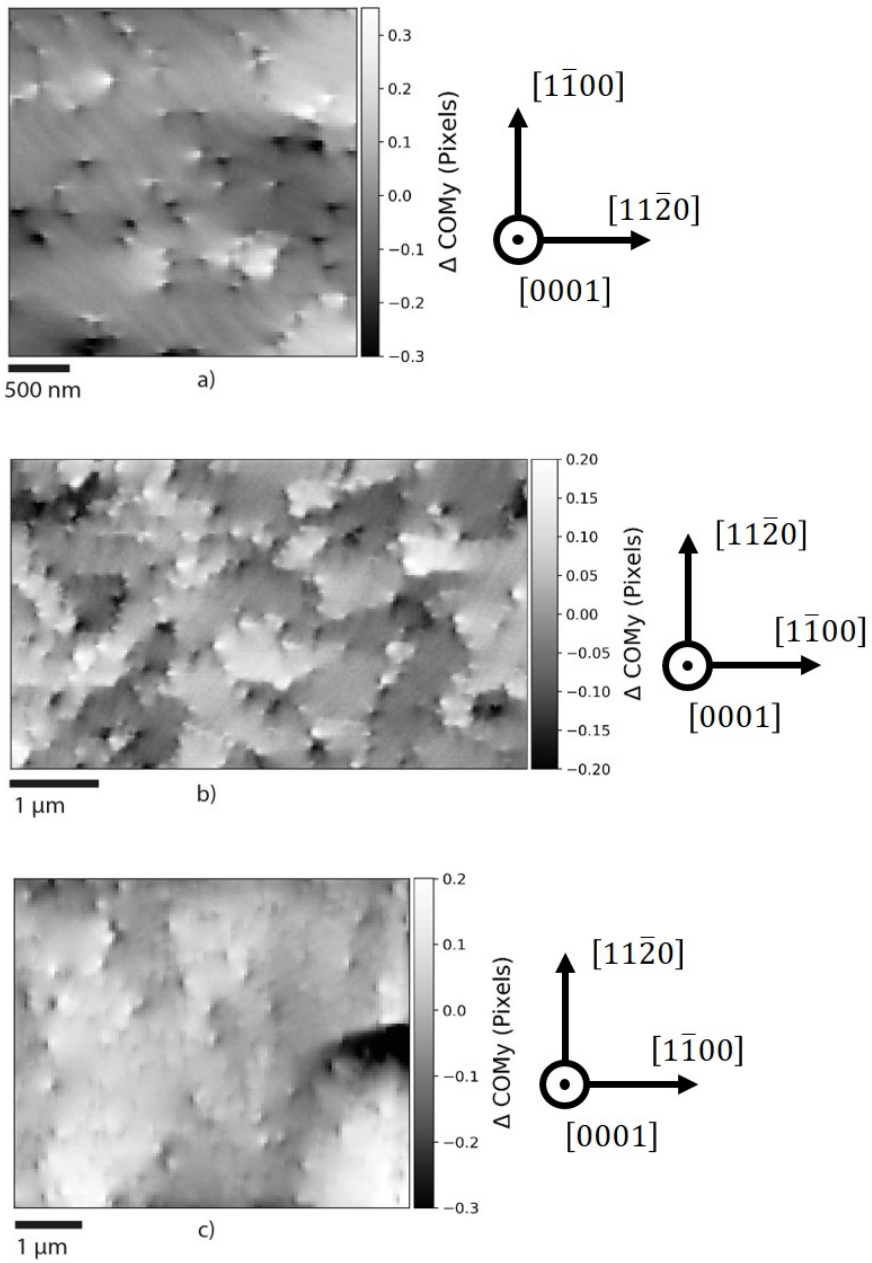

Figure 3.6: VDCOMy images produced from bottom half of EBSPs from a a) 1600 nm thick Ga-polar GaN thin film with a dislocation density of 3×10^8 cm^{-2}, b) 2150 nm thick Ga-polar GaN thin film with a dislocation density of 2×10^9 cm^{-2} and c) 6.6 μm thick AlN thin film with a dislocation density of 1×10^9 cm^{-2}.

completely resolved. However, as the dislocation and step densities increase again going to the Ga-polar GaN sample shown in Figure 3.6b), it becomes much harder to resolve individual steps, although it is still clear that they are present. Here, dislocations are still just as prominent as in Figures 3.6a) and 3.5b) and there is even strong subgrain contrast where subgrains are decorated by the dislocation distribution. The strong dislocation and weak step contrast occurs in the higher density samples because as the step density increases, steps are more difficult to fully resolve and their effect on the intensity distribution is averaged out, allowing the dislocation contrast to stay dominant.

This effect is also apparent when moving to other materials such as AlN thin films (Figure 3.6c). This sample exhibits a relatively high dislocation density (1×10^9 cm^{-2}) and surface step density. The individual dislocations are still fully resolvable, while the surface step contrast is significantly decreased.

While it is unfortunate that individual steps and where they terminate cannot be fully resolved in the samples shown in Figure 3.6, it highlights an important limitation of the imaging technique. As the step density approaches the spatial resolution of EBSD, the ability to both resolve surface steps and determine where they terminate significantly decreases. Improving spatial resolution, and therefore further optimising VDCOM imaging by going to lower beam voltages is the subject of ongoing research.

Ultimately, here it can be demonstrated that VDCOM imaging is still a useful method for imaging individual dislocations and dislocation distributions at relatively high dislocations densities in nitride thin films, while surface steps become more difficult to resolve for higher step densities.

3.8 Comparison of VDCOM with ECCI

Both ECCI and VD are dependent upon the scalar variation in BSE yield, which is a result of the modulation of diffraction effects of the electron beam upon incidence with the sample. Consequently, they are formed from the exact same signal mechanism and their differences, should the detectors share the same geometry, should be non-existent for the same acquisition parameters. Consequently, the comparison between VD and

VDCOM can also be extended to the comparison between VDCOM and ECCI. For a case where the user is simply interested in the imaging of threading dislocations, does not require images with different dominant contrast mechanisms, and does not require any underlying crystallographic information, it is recommended that ECCI is used due to the significantly lower requirements for data storage and shorter acquisition times. Figure 3.7 shows a comparison between a VDCOMy bottom half image and an ECCI image of the same area for a Ga-polar GaN thin film. The ECCI was taken using forescatter diodes attached to the bottom of the pixelated detector. The images were acquired in a sample-detector geometry in which topography is suppressed- which is best for a comparison where only threading dislocations are of interest.

The notable difference between 3.7a) and b) is the much greater signal to noise in a). However, this is a result of much longer exposure due to the requirement of collecting high-signal EBSPs that would be used in further quantitative analysis. In total the effective time taken to acquire the VDCOMy image is around 30 minutes, with post-processing times of approximately 2 minutes. In contrast, the ECCI image was acquired in approximately 1-2 minutes and required no post-processing. Had the ECCI acquisition time been increased, the signal and image quality would be very similar between a) and b).

Ultimately, the advantages of using VDCOM over traditional ECCI are only particularly relevant when either: a) EBSD will be performed anyway to quantitatively analyse a sample or b) flexibility is required in being able to move the detector around the chamber and images with different contrast mechanisms are of interest.

3.9 Summary

The use of a pixelated detector for nitride thin film imaging allows greater flexibility than the hardware diodes that have traditionally been used in SEM based dislocation imaging. By using a pixelated detector, the user can define multiple 'virtual' diodes of different shapes and sizes, which can be located in any position across the pixel array. By monitoring how the total intensity recorded in these virtual diodes changes as the beam moves across the sample, different images of the same sample surface can be

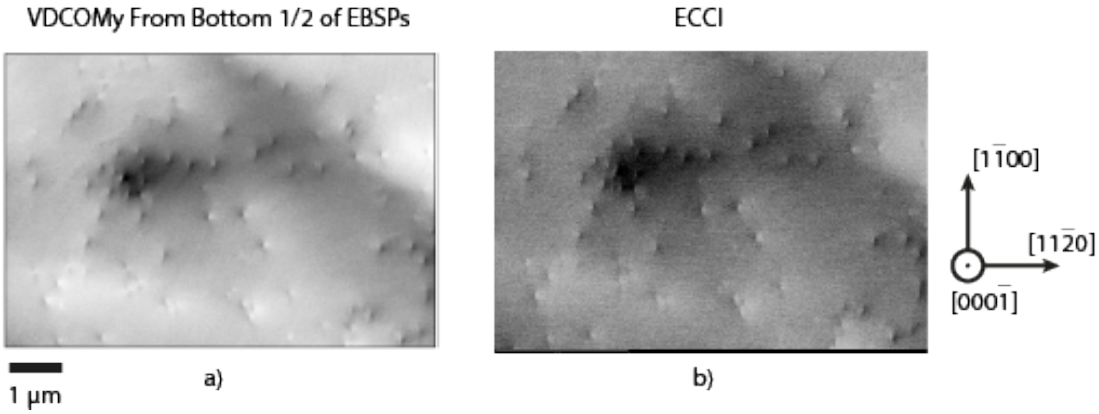

Figure 3.7: a) VDCOMy image formed from the bottom half of EBSPs for a Ga-polar GaN thin film (step size 25 nm) and b) the same area on the GaN thin film imaged from measuring the BSE yield with a hardware diode from a continuous scan of the beam (ECCI). The VDCOMy image can be seen to have a higher signal to noise due to the longer dwell time compared to the ECCI image, however both images show effectively the same features.

produced showing different dominant contrast mechanisms. In this chapter it has been shown how one can controllably produce surface images of an N-polar GaN thin film using the VD method which show either dislocations or surface steps and dislocations.

Another advantage of using a pixelated detector is that the change in position of the recorded BSE distribution can also be monitored as the electron beam is scanned across the sample (known as centre of mass imaging). It has been shown that by applying COM imaging within virtual diodes (VDCOM imaging), one can again control the type of contrast dominating the images produced by this technique; showing either dislocations or surface steps and dislocations. VDCOM has the advantage over regular (full EBSP) COM imaging in that it has the potential to offer better refinement of the type of image contrast obtained (topography, dislocations, etc). This can be particularly helpful when contrast from one type of feature is highly suppressed in the original COM image. Here, the placement of virtual diodes and resulting VDCOM analysis can improve this contrast by measuring the COM shift in parts of the EBSPs where the BSE contribution from the other, more dominant effect, should be less.

It has been demonstrated that VDCOM produces images of both dislocations and dislocations and surface steps with high signal-to-noise, by utilising the fact we can

monitor changes in the backscattered electron intensity distribution in both the x and y positions. Meanwhile, VD imaging can also produce images of dislocations or dislocations and surface steps, but due to the asymmetry of the intensity distribution across the detector screen, one image will inevitably have a poorer signal-to-noise ratio. While this is advantageous for the VDCOM technique, VD imaging is more flexible in that the virtual diodes can be significantly smaller when measuring the change in the magnitude of the BSE yield than when measuring changes in the position of the BSE distribution. This is purely because as smaller virtual diodes are used for VDCOM, the area over which changes in the COM are detectable is much smaller, reducing the signal-to-noise in the resulting VDCOM images. VDCOM is, however, also unaffected by unwanted modulations in beam current or charging, as demonstrated with the N-polar dataset used here, whereas VD imaging suffers from this.

Ultimately, from the data sampled here, it is suggested that for dislocation analysis, VDCOM imaging provides the best images in that different features can be emphasised and the resulting images have high signal-to-noise.

The applicability of VDCOM as an imaging technique has been investigated across other thin film samples with varying surface step densities and dislocation densities. It is clear that at high surface step densities it no longer becomes possible to identify where surface steps terminate, although they are still visible. Despite this, at higher dislocation densities, VDCOM is still able to resolve individual dislocations and images exhibit subgrain contrast. This provides valuable information on dislocation distributions on the surface of nitride thin film samples. Finally, a comparison of VDCOM with ECCI was carried out where it was stressed that VDCOM provides significantly greater flexibility in producing high-signal images with varying contrast mechanisms. However, if solely imaging threading dislocations is of interest, with no further analysis or multi-contrast imaging required, then ECCI is a much faster and more data-storage-friendly technique.

Chapter 4

Simulating Strain and Lattice Rotations in GaN

4.1 Introduction

When interrogating the strain and lattice rotation distributions associated with TDs using EBSD, it is extremely useful to have reliable simulations to provide context for the measurements. In the case of this thesis, the EBSD analysis involved comparing in-plane and out-of-plane misorientation and strain measurements to try to identify TD types. In order to do this analysis effectively, simulations were produced to see how each type of TD (screw, edge, and mixed) would affect the individual strain and lattice rotation components. This could then provide a mechanism through which different TD types can be distinguished.

As the magnitudes of wurtzite GaN's lattice parameters, a and c, are different, the material is anisotropic. However, for simplicity, GaN is often treated as though it was isotropic in elasticity calculations [150]. This assumption has been shown to be valid with good agreement between experimentally calculated isotropic and anisotropic elastic constants [151]. Thus, wurtzite GaN can be described with one value for Poisson's Ratio, ν. This is the ratio of the transverse contraction to longitudinal extension of an object experiencing strain and is given by [152]:

$$\nu = \frac{C_{13}}{C_{11} + C_{12}} \tag{4.1}$$

where C_{13}, C_{11} and C_{12} are elastic constants. For c-axis oriented GaN grown via MOVPE, much like the samples analysed in this thesis, Poisson's ratio has an experimentally measured value of 0.183 ± 0.003 [152]. Consequently, by using Poisson's ratio and the equations for the isotropic elastic displacement of the lattice due to TDs (Eqs. 2.11-2.21), it is possible to simulate the strain and lattice rotations due to threading dislocations normal to the surface in GaN. For inclined TDs, the treatment must be expanded upon. These simulations also correspond to the strain distributions *outside* of the dislocation core. Including the dislocation core with this treatment results in a singularity, so alternative non-linear approaches for this are needed. Fortunately, simulating the dislocation core is of little relevance to current EBSD measurements due to the spatial resolution limits imposed by the technique (25 nm step size compared to an approximate TD core radius of 1 nm). As EBSD measures *relative* strain and misorientation, the magnitudes and, to some extent, the precise distributions of the local strain and lattice rotations measured in large EBSD maps cannot be accurately compared with simulations without knowledge of how the large-scale, 'background' strain and lattice rotation distributions evolve across a given GaN sample. This is because minor variations in this large-scale strain/orientation can increase or reduce measured relative strain/orientation values. However, what the simulations do provide is the opportunity to understand how different types of TDs affect different strain/rotation components individually, as well as getting an idea of the spatial range of these effects.

It is important to consider exactly what information from the simulations can be compared to real EBSD measurements. In Section 2.3.5 *Deriving Strain from EBSPs* it was explained that EBSD is insensitive to hydrostatic strain. Consequently, in this chapter two shear components (ϵ_{zx} and ϵ_{yx}) will be simulated as these have no hydrostatic component. These components also allow for the comparison between in-plane strain (ϵ_{yx}) and out-of-plane strain (ϵ_{zx}), which is useful for comparing the effects of screw, mixed, and edge TDs. The lattice rotations ω_{yx} and ω_{zx} will be simulated to compare in-plane and out-of-plane rotations. In the first instance, these simulations

will be done at the surface boundary for a completely flat GaN sample with a step size of 25 nm (the same step size used in measurements reported later on in the thesis). Further simulations will then be performed at a fixed depth below the sample surface, corresponding to the sampling depth of an EBSD measurement at a beam voltage of 20 kV (see Figure 4.6 for typical range). This provides information about how the strain fields and lattice rotations evolve for particular TDs (screw, edge, and mixed) and will likely be a more accurate simulation of what EBSD measures, compared to the surface simulation. Finally, the shear strain simulations will be performed taking into account the minimum measurable strain imposed by the strain resolution of strain calculations via pattern matching, the deleterious effects of the size of the BSE interaction volume on the spatial resolution, as well as the reduced resolution in the detector y direction caused by the elongation of the interaction volume due to sample tilting. This will only be done for shear strains in this chapter, as those are the strains that have been mapped by EBSD further on in this thesis. As this is a fairly crude approach and only meant to give a rough understanding of how the measurements are influenced, it will only be demonstrated on the shear strain and not the lattice rotations. The perturbed simulations are to get an idea of how the true strain field (and similar measurements) may be distorted when measuring with EBSD. All simulations in this chapter were written in Python.

4.2 Derivation of Isotropic Strain and Lattice Rotations for Threading Dislocations

For the small strains observed in GaN, a simplified version of Eq. 2.8 can be used to generate the strain fields of TDs:

$$\epsilon_{ik} = \frac{1}{2}\left(\frac{\partial u_i}{\partial x_k} + \frac{\partial u_k}{\partial x_i}\right) \tag{4.2}$$

such that ϵ_{yx} and ϵ_{zx} are given by:

$$\epsilon_{yx} = \frac{1}{2}(\frac{\partial u_y}{\partial x_x} + \frac{\partial u_x}{\partial x_y}) \tag{4.3}$$

and

$$\epsilon_{zx} = \frac{1}{2}(\frac{\partial u_z}{\partial x_x} + \frac{\partial u_x}{\partial x_z}) \tag{4.4}$$

respectively. The lattice rotations can similarly be calculated using Eq. 2.11, which will be quoted here again for accessibility:

$$\omega_{ik} = \frac{1}{2}(\frac{\partial u_i}{\partial x_k} - \frac{\partial u_k}{\partial x_i}) \tag{4.5}$$

The differential terms in these expressions can be derived by differentiating the terms from Eqs. 2.12-2.22. This was done by hand initially and then checked with Wolfram Alpha. Including both image force (surface relaxation) and infinite medium terms where appropriate, these differential terms for edge TDs come out to be:

$$\frac{\partial u_x}{\partial x_y} = \frac{b_1}{2\pi}[\frac{x}{x^2+y^2} + \frac{x^3 - xy^2}{2(1-\nu)(x^2+y^2)^2}] + \frac{\nu b_1}{4\pi(1-\nu)}[\frac{-2xy^2z}{R^3(R-z)^2} - \frac{4xy^2z}{R^2(R-z)^3} + \frac{2xz}{R(R-z)^2} + \frac{(1-2\nu)x}{(R-z)^2} - \frac{2(1-2\nu)xy^2}{R(R-z)^3}] \tag{4.6}$$

$$\frac{\partial u_y}{\partial x_x} = \frac{-b_1}{2\pi}\frac{1}{4(1-\nu)}[(1-2\nu)\frac{2x}{x^2+y^2} + \frac{4xy^2}{(x^2+y^2)^2}] + \frac{\nu b_1}{4\pi(1-\nu)}[\frac{(1-2\nu)x}{-zR+R^2} + \frac{(3-2\nu)xz}{R(R-z)^2} - \frac{2(3-2\nu)xy^2}{R(R-z)^3} + \frac{2xy^2}{R^3(R-z)} + \frac{2xy^2}{R^2(R-z)^2}] \tag{4.7}$$

$$\frac{\partial u_x}{\partial x_z} = \frac{\nu b_1}{4\pi(1-\nu)}[\frac{-2xyz}{R(R-z)^2} - \frac{4xyz(z/R-1)}{R(R-z)^3} + \frac{2xy}{R(R-z)^2} + \frac{2(1-2\nu)xy}{R(z-R)^2}] \tag{4.8}$$

$$\frac{\partial u_z}{\partial x_x} = \frac{\nu b_1}{2\pi(1-\nu)}[\frac{-xy}{R^3} - \frac{(1-2\nu)xy}{R(R-z)^2}] \tag{4.9}$$

where $R = \sqrt{x^2+y^2+z^2}$, ν is Poisson's ratio and b_1 is the magnitude of the edge Burgers vector in the x direction. Similarly, the differential terms for screw TDs are:

$$\frac{\partial u_x}{\partial x_y} = \frac{b_3}{2\pi}[\frac{1}{R-z} - \frac{y^2}{R(R-z)^2}] \tag{4.10}$$

$$\frac{\partial u_y}{\partial x_x} = -\frac{b_3}{2\pi}[\frac{1}{R-z} - \frac{x^2}{R(R-z)^2}] \tag{4.11}$$

$$\frac{\partial u_x}{\partial x_z} = \frac{b_3}{2\pi}[\frac{y}{R^2-zR}] \tag{4.12}$$

$$\frac{\partial u_z}{\partial x_x} = -\frac{b_3}{2\pi}[\frac{y}{x^2+y^2}] \tag{4.13}$$

where b_3 is the magnitude of the screw Burgers vector. For all of these equations, the dependence on R comes purely from the surface relaxation/image force terms which change with increasing distance from the surface boundary. The Burgers vector/infinite medium terms are not dependent on Z assuming a line direction perpendicular to the free surface. Generating the strain and lattice rotation fields for a mixed TD requires the sum of the screw and edge differential terms.

4.3 Simulation of Shear Strain and Lattice Rotations in GaN at the Surface Boundary

The strain and misorientation data shown in this thesis were taken such that the x-axis of the detector reference frame was aligned with the crystallographic direction $[11\bar{2}0]$. As such, edge TDs with Burgers vectors $\frac{1}{3}[11\bar{2}0]$ will have their entire Burgers vector oriented in the x direction. To simplify te simulations, it will be assumed that all edge TDs have their Burgers vectors oriented this way. While this is likely not true, edge Burgers vectors oriented in different directions will only change the spatial distribution

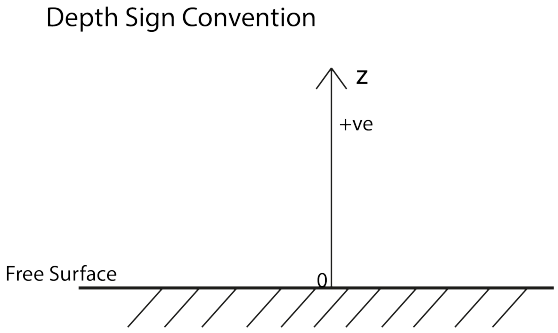

Figure 4.1: z-axis sign convention used for simulations. The z value is zero at the free surface and decreases with depth into the sample.

of the associated strain and lattice rotations, and not the calculated magnitudes or whether in-plane/out-plane components are affected (the primary goal of these simulations). Staying with this alignment then for simulation purposes means that b_1 in Eqs. 4.6-4.9 has magnitude a, where a is the lattice parameter of GaN, equal to the total magnitude of the edge Burgers vector. Similarly, the z-axis of the detector reference frame was aligned with [0001], meaning the magnitude of b_3 is the entire magnitude of the screw Burgers vector, which is equal to the lattice parameter c. Of course, the Burgers vectors can be positive or negative, denoting their direction (left/right for an edge, up/down for a screw). For the simulations in this chapter, only the positive direction (right and up respectively) is used. The sign convention for depth is chosen such that $z = 0$ at the free surface and increases into free space, meaning sub-surface depth has a negative z value. This is illustrated in Fig. 4.1. Inserting the corresponding values for the lattice parameters into Eqs. 4.7-4.13 where necessary, setting $z = 0$, using $\nu = 0.183$, and combining differential terms in accordance with Eq. 4.2 and 4.4 allows one to produce simulations of strain and lattice rotations at the surface boundary of GaN.

4.3.1 Shear Strain

Fig. 4.2 shows the various components of edge and screw TDs contributing to the in-plane shear strain ϵ_{yx} and their combined effects for a mixed TD. Edge TDs contribute both infinite medium and surface relaxation terms, as shown in a) and b). Comparing

them both, it is immediately obvious that the surface relaxation term is considerably smaller, and it can therefore be inferred directly that the shear strain ϵ_{yx} associated with edge TDs is dominated by the infinite medium strain associated with the Burgers vector. This can be seen by plotting the combined strain for an edge TD, shown in c). Unlike for an edge TD, as the Burgers vector of a screw TD in GaN lies completely out-of-plane, there is no ϵ_{yx} infinite medium strain associated with a screw TD. There is, however, a large contribution from the surface relaxation of the screw. This is shown in d) and is comparable in magnitude to the magnitude of the entire contribution from the edge. e) shows the ϵ_{yx} shear strain associated with a mixed TD which is a combination of the effects of the screw and edge components.

Unlike ϵ_{yx}, the out-of-plane shear component ϵ_{zx} is zero at the surface for edge, screw, and mixed TDs (Fig. 4.3). This is a consequence of the traction-free boundary condition imposed on this treatment, which requires that stress at the surface, normal to the surface is zero (discussed previously in Section 2.15 *Displacement of the Lattice due to Threading Dislocations*). However, the screw TD does have non-zero magnitude in its infinite medium and surface relaxation terms, but these are equal and opposite and so cancel for the screw TD as a whole (Fig. 4.3b) and c)).

4.3.2 Lattice Rotations

Fig. 4.4 shows the various components of edge and screw TDs contributing to the in-plane lattice rotation ω_{yx} and their combined effects for a mixed TD. The infinite medium term for edge TDs, a), increases while the surface relaxation, b), reduces to zero when compared with the corresponding in-plane shear strain terms in Fig. 4.2. Similar to the in-plane shear, ϵ_{yx}, the in-plane lattice rotation also has a strong surface relaxation component for screw (and therefore mixed) TDs.

The change in sign from Eq. 4.2 to Eq. 4.5 means that, unlike the out-of-plane shear, the out-of-plane lattice rotation is non-zero for all TDs at the surface (Fig. 4.5). The edge TDs have a low contribution from surface relaxation only, while screw TDs show much stronger contributions from infinite medium and surface relaxation terms which are now additive and not self-cancelling. Consequently, the out-of-plane lattice

rotation for mixed TDs is strongly dominated by the screw TD total contribution.

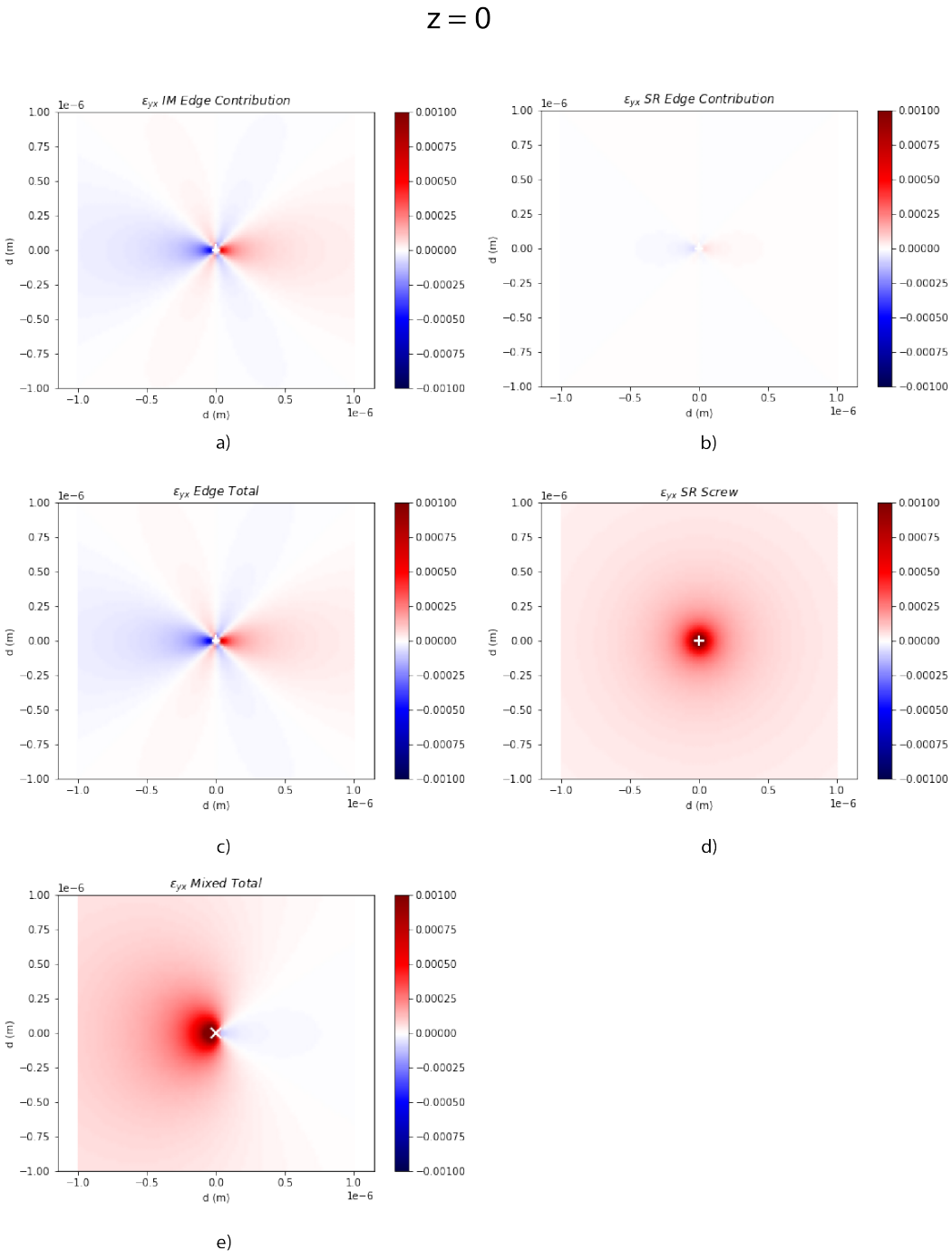

Figure 4.2: Simulations of shear strain component ϵ_{yx} in c-oriented GaN at the surface boundary, with a step size of 25 nm. a) shows the infinite medium (IM) term for an edge TD. b) shows the surface relaxation (SR) term for an edge TD. c) shows the combined effect of IM and SR edge TD terms. d) shows the effect of a screw TD on ϵ_{21} which is purely surface relaxation. e) shows the total effects of a mixed TD.

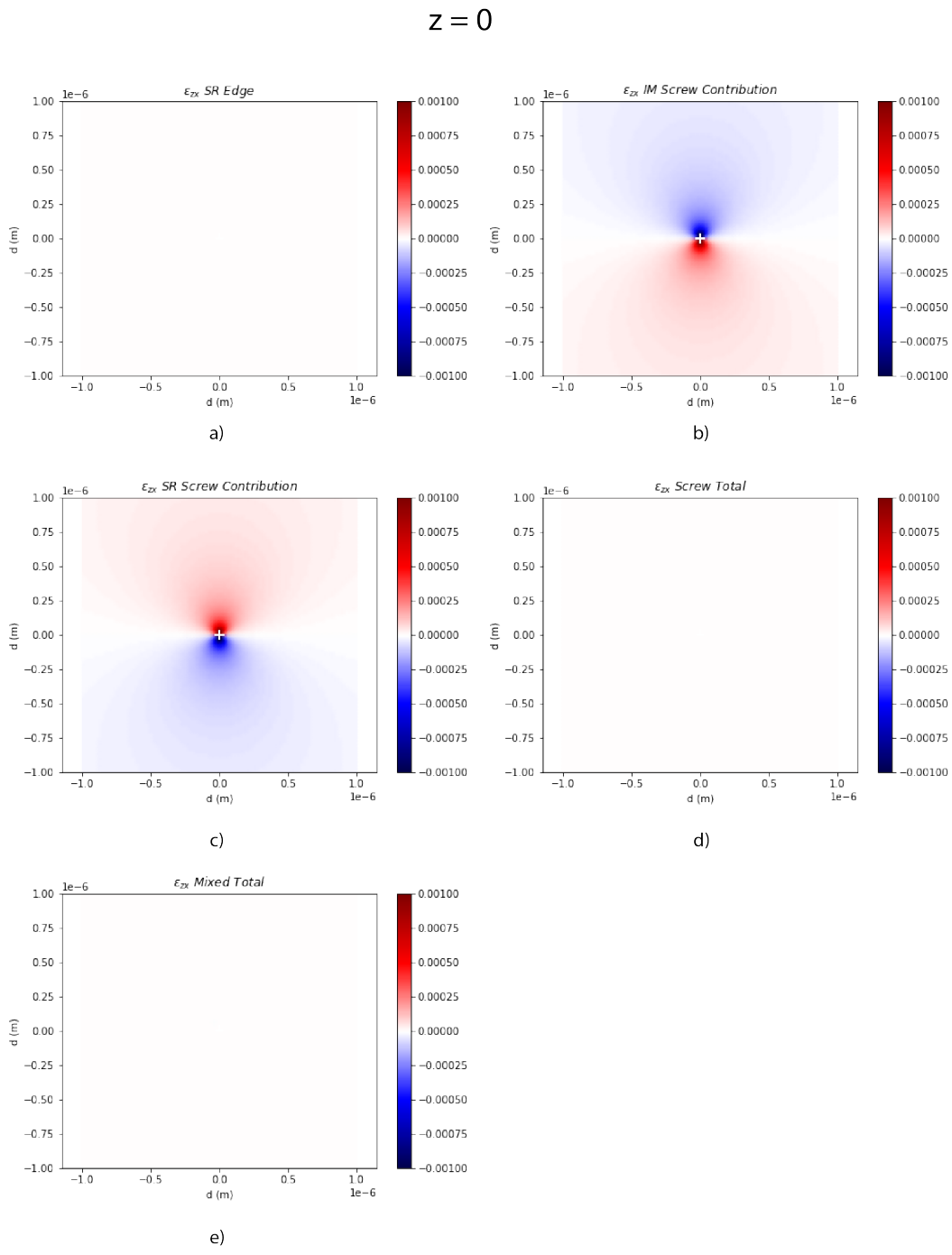

Figure 4.3: Simulations of shear strain component ϵ_{zx} in c-oriented GaN at the surface boundary, with a step size of 25 nm. a) shows the surface relaxation (SR) term for an edge TD. b) shows the infinite medium (IM) term for a screw TD. c) shows the SR term for a screw TD. d) shows the total effect of a screw TD. e) shows the total effects of a mixed TD.

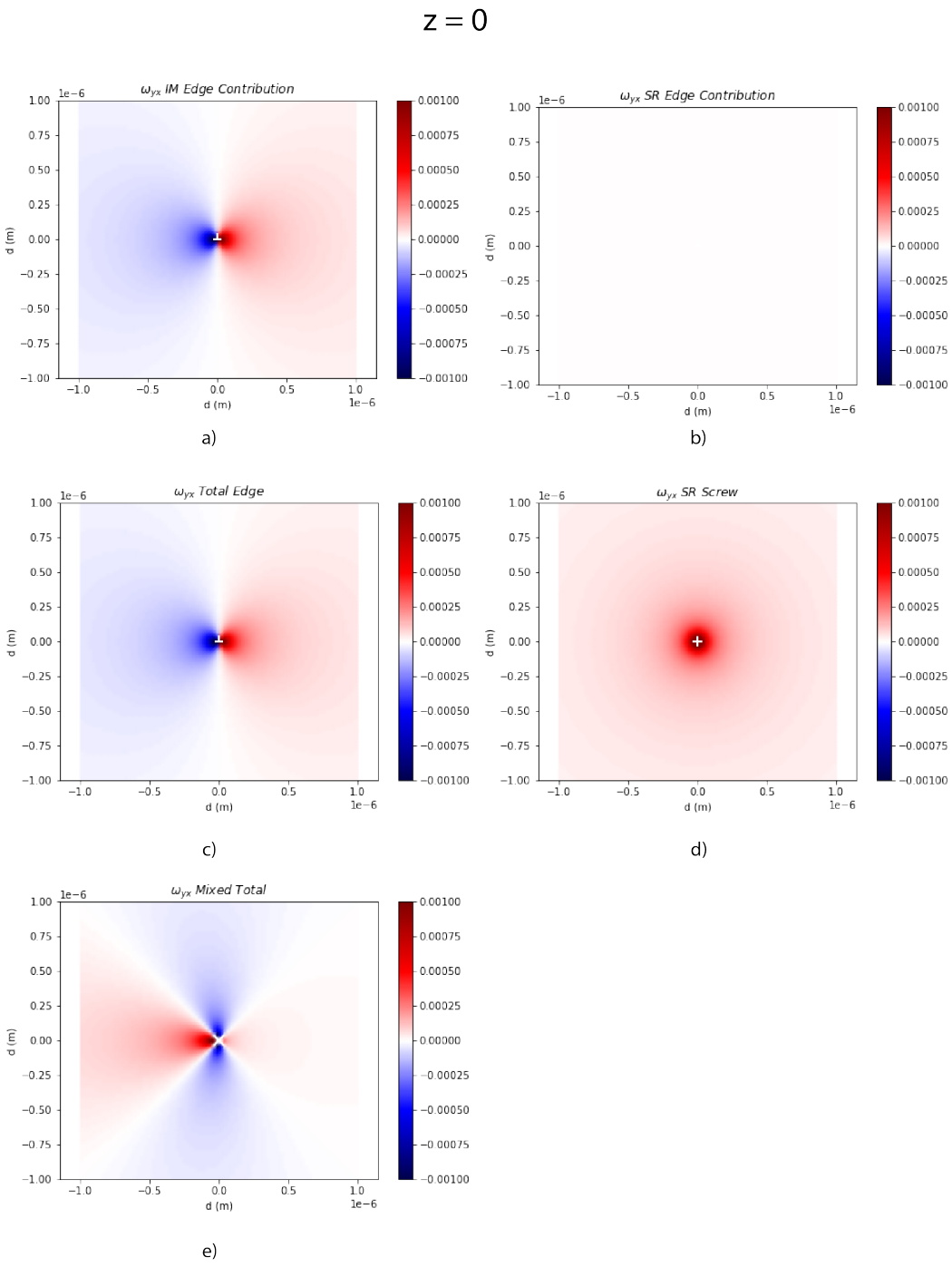

Figure 4.4: Simulations of lattice rotation ω_{yx} in c-oriented GaN at the surface boundary, with a step size of 25 nm. a) shows the infinite medium (IM) term for an edge TD. b) shows the surface relaxation (SR) term for an edge TD. c) shows the combined effect of IM and SR edge TD terms. d) shows the effect of a screw TD on ω_{yx} which is purely surface relaxation. e) shows the total effects of a mixed TD.

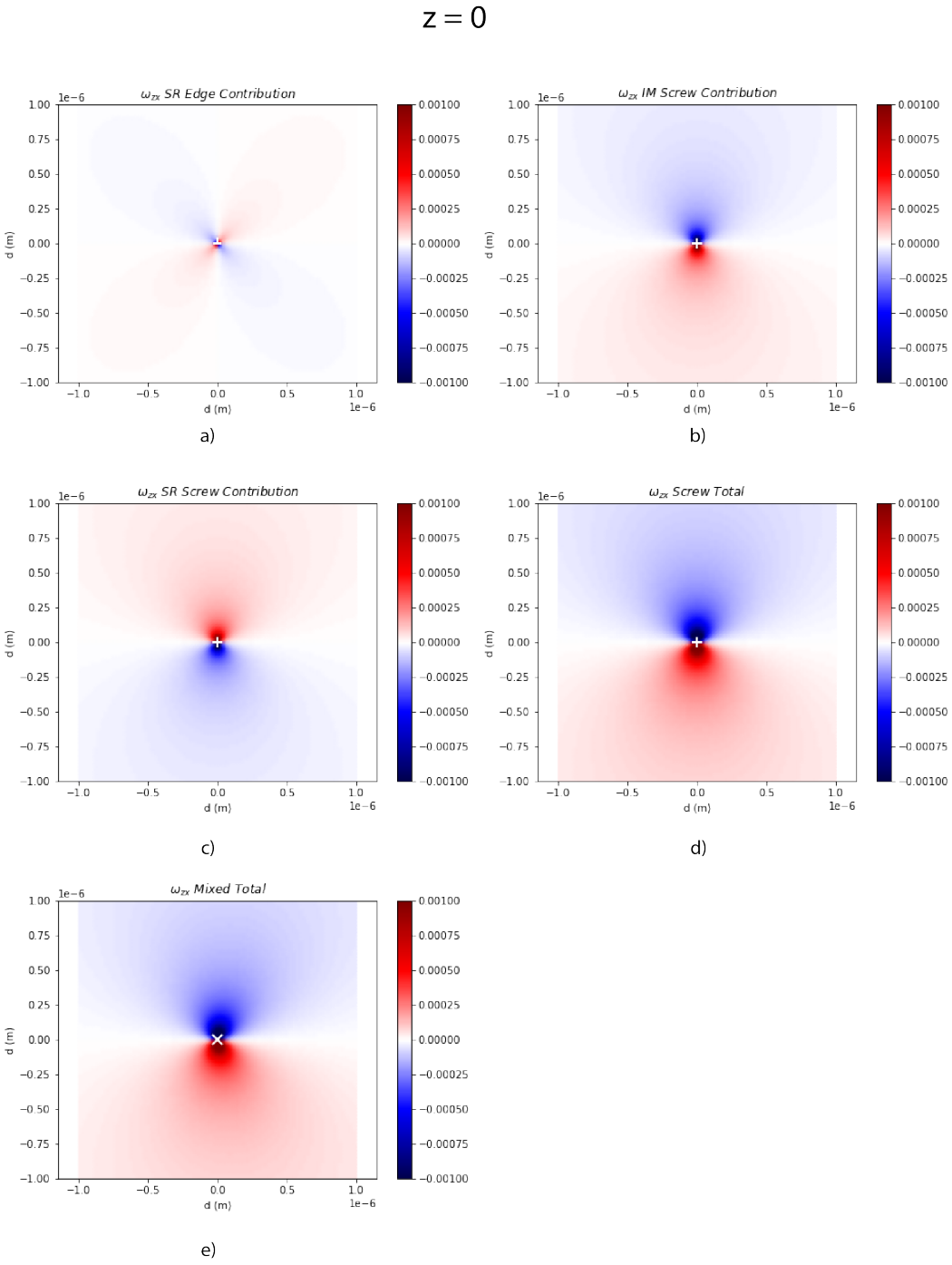

Figure 4.5: Simulations of lattice rotation ω_{zx} in c-oriented GaN at the surface boundary, with a step size of 25 nm. a) shows the surface relaxation (SR) term for an edge TD. b) shows the infinite medium (IM) term for a screw TD. c) shows the SR term for a screw TD. d) shows the total effect of a screw TD. e) shows the total effects of a mixed TD.

4.4 Simulation of Strain and Lattice Rotations in GaN at Fixed non-zero z

In order to estimate the depth from which the EBSD comes from it can be useful to perform computational Monte Carlo simulations with simulation parameters close to the experimental ones. As such Fig. 4.6 shows the paths of simulated electrons in a 900 nm thick GaN film tilted to 70° for a 20 keV beam (same energy used for experimental data in this thesis unless stated otherwise). 1000 electron paths were simulated in total, however as the quantitative information is derived from the Kikuchi bands in the EBSPs and these are formed from close-to-beam-energy electrons, a threshold was imposed such that only the paths of electrons with a minimum energy of 19.4 keV (3% below beam energy) were recorded. The red paths in Fig. 4.6 highlight the BSEs, while the yellow paths trace out absorbed beam electrons. The simulation was performed using the Mott interpolated total cross-section and does not include diffraction effects which are prevalent in EBSD measurements. The incorporation of diffraction effects requires a much more sophisticated and computationally intensive model, which would for the purposes of this chapter likely be unnecessary as all that is required is a ball-park depth for the BSEs contributing to the EBSPs. As can be seen from Fig. 4.6, most high-energy BSEs come from within the first 20 nm of the sample. As such, -20 nm is the value chosen for z for the following shear strain and lattice rotation simulations.

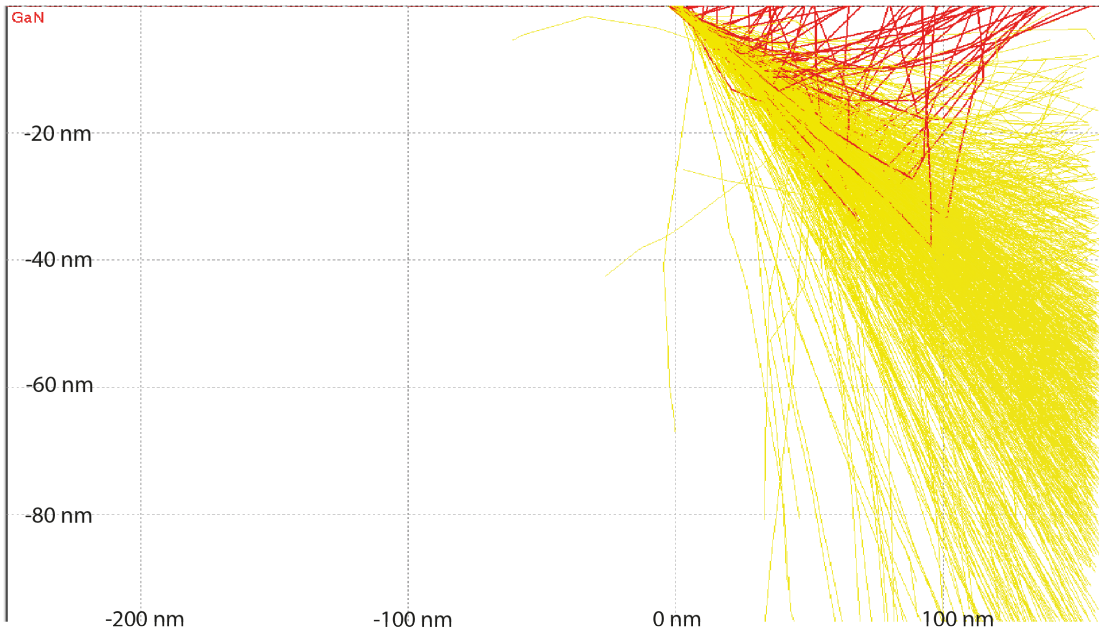

Figure 4.6: Monte Carlo simulation of 1000 electron paths in GaN with an initial beam energy of 20 keV and a minimum energy cut-off of 19.4 keV (3% below the beam energy). Red lines are the paths of electrons that resurface with energy 19.4 keV or more, while yellow lines are the paths of electrons whose paths terminate in the sample or that resurface with less than 19.4 keV. The red paths give an approximate sampling depth for the Kikuchi bands in an EBSP.

4.4.1 Shear Strain

The main difference between the ϵ_{yx} components shown in Fig. 4.2 for the surface boundary and Fig. 4.7 for 20 nm below the surface is the reduction in the magnitude of the surface relaxation terms of screw and edge (and correspondingly mixed) TDs in the latter. This is easy to understand as surface relaxation effects should reduce with depth into the surface, where effects of a free boundary are less prominent, and the material becomes more like the bulk crystal. This reduction in surface relaxation has even more prominent effects on ϵ_{zx} when evaluated 20 nm below the surface (Fig. 4.8). For edge TDs, there is a brief increase in surface relaxation on moving away from the first surface layer, however this decays quickly into the bulk. While possibly counter-intuitive, this is because- despite being equal and opposite at the surface- the differential term $\frac{\partial u_z}{\partial x_x}$ decays slower than the term $\frac{\partial u_y}{\partial x_x}$ when moving away from the

surface. As the surface relaxation associated with an edge TD is the sum of these two terms, there is a non-zero magnitude just below the surface. This is consistent with previous literature [42]. The surface relaxation associated with screw TDs below the surface now decreases, meaning it no longer cancels the infinite medium term, and there is a non-zero shear strain present associated with screw TDs. While the distribution decays quickly away from the centre of the TD, the magnitude is relatively high, close to the centre. This is also the dominant contributing factor to the strain profile of a mixed TD at 20nm depth (Fig. 4.8e)).

4.4.2 Lattice Rotations

The lattice rotations ω_{yx} and ω_{zx} are also affected by decreases in surface relaxation terms (Fig. 4.9 and 4.10 respectively). The screw TDs have a reduced associated shear strain ω_{yx}, reducing that of the mixed TD as well. And for ω_{zx}, edge and screw both have reduced surface relaxation, decreasing their total associated ω_{zx} shear strains and that of the mixed TD also.

4.5 Perturbed Measurement of Shear Strain Simulations

To estimate how the true strain fields may be distorted in the final EBSD maps, it is important to consider two of the main limiting factors of a real EBSD strain measurement. These are, the spatial resolution limits due to the interaction volume and the strain resolution limit of the pattern matching approach for strain measurement.

As has already been discussed, due to the 70° tilt of the sample, there is an elongation of the interaction volume causing the spatial resolution in the y-direction to be worse than that in the x-direction. In order to incorporate the effects of this, a two-step process shall be performed. The first step of this is to actually assume the sample is flat and consider the size of the interaction volume, which in a flat geometry will be symmetric. Fig. 4.11 shows a Monte Carlo simulation of 1000 electrons incident upon a 900 nm thick GaN sample oriented normal to the beam (i.e. flat). Again, the Monte Carlo simulation has been limited to only electrons within 3% of the incident beam

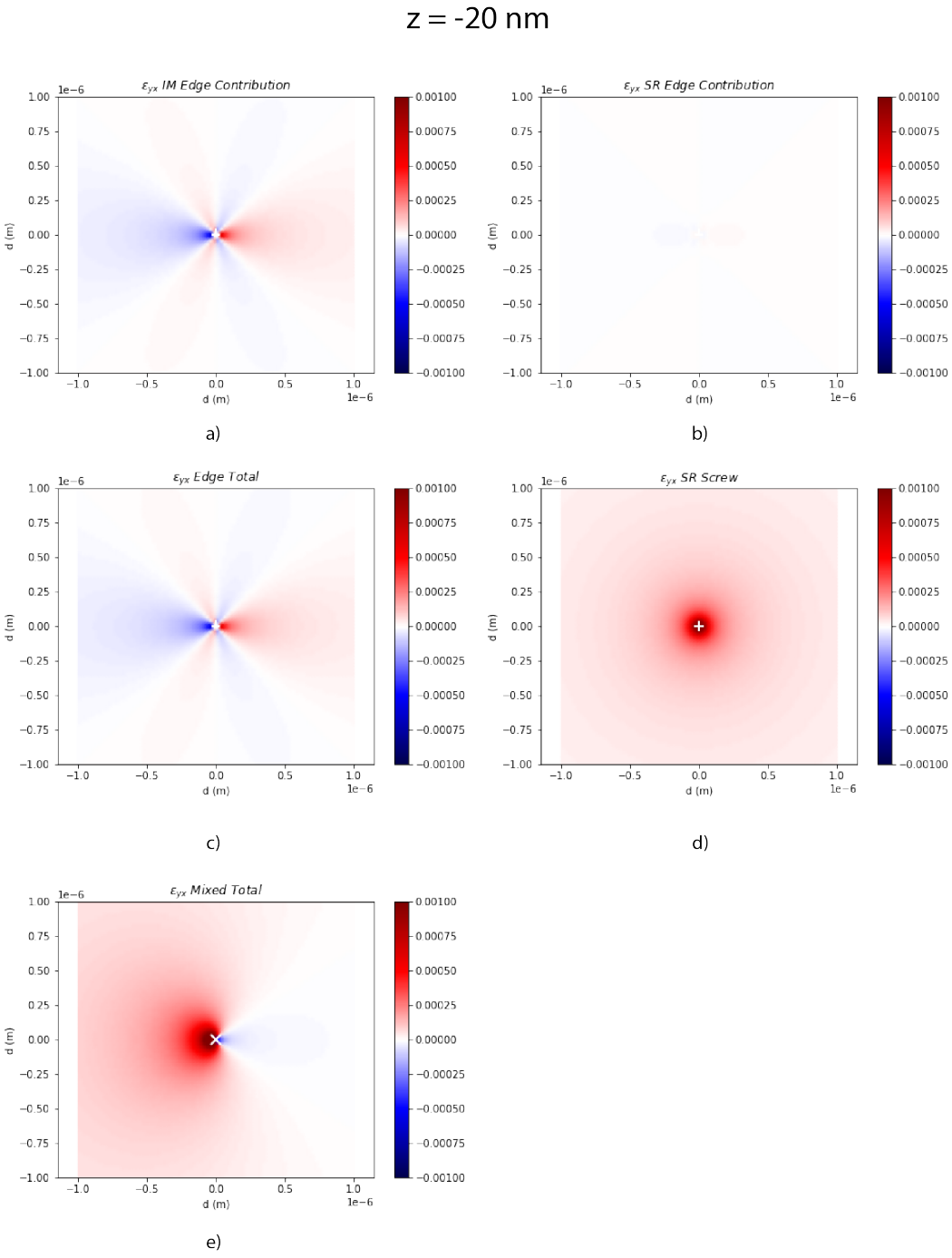

Figure 4.7: Simulations of shear strain component ϵ_{yx} in c-oriented GaN at 20 nm below the surface boundary, with a step size of 25 nm. a) shows the infinite medium (IM) term for an edge TD. b) shows the surface relaxation (SR) term for an edge TD. c) shows the combined effect of IM and SR edge TD terms. d) shows the effect of a screw TD on ϵ_{yx} which is purely surface relaxation. e) shows the total effects of a mixed TD.

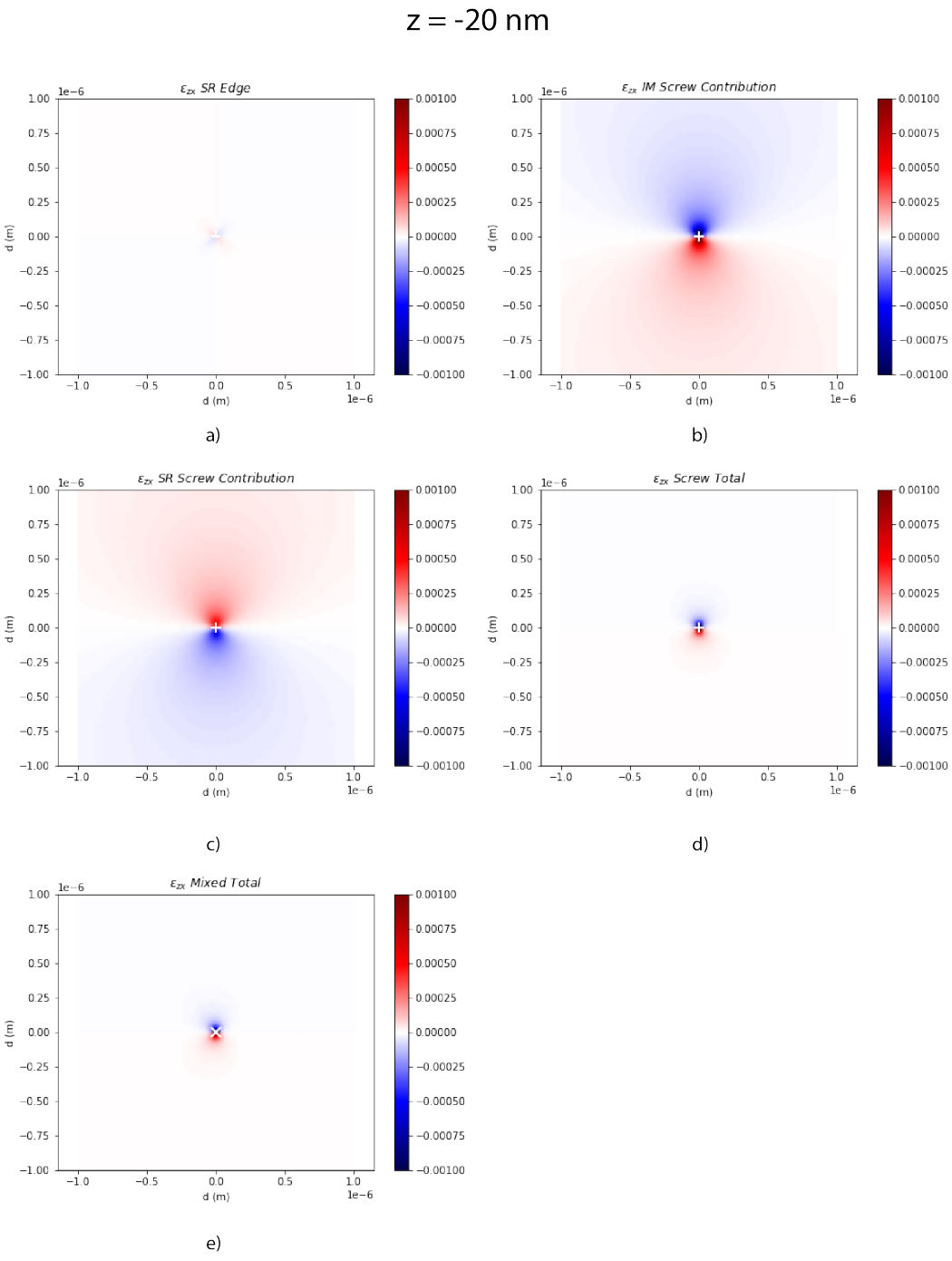

Figure 4.8: Simulations of shear strain component ϵ_{zx} in c-oriented GaN at 20nm below the surface boundary, with a step size of 25 nm. a) shows the surface relaxation (SR) term for an edge TD. b) shows the infinite medium (IM) term for a screw TD. c) shows the SR term for a screw TD. d) shows the total effect of a screw TD. e) shows the total effects of a mixed TD.

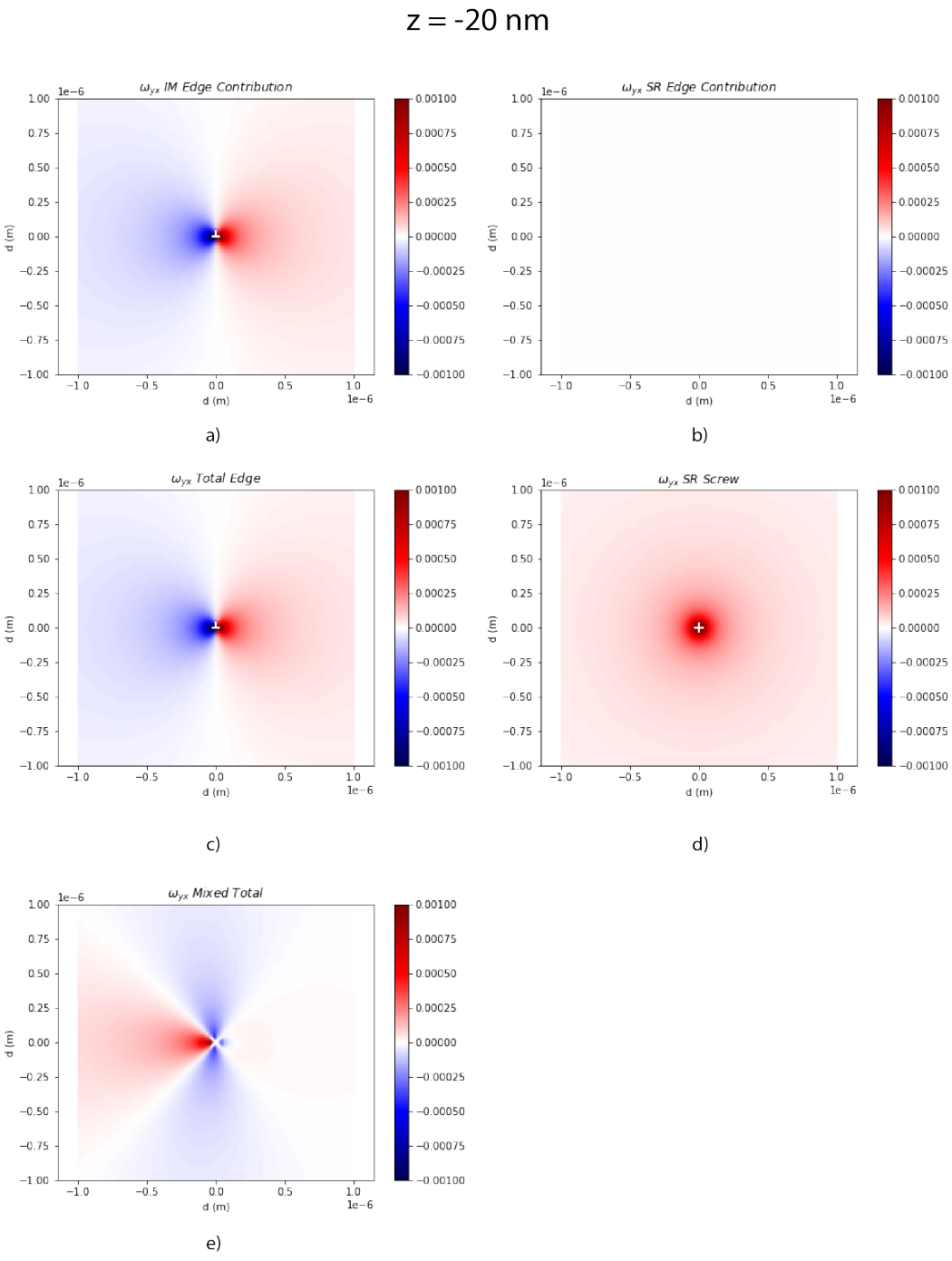

Figure 4.9: Simulations of lattice rotation ω_{yx} in c-oriented GaN at 20 nm below the surface boundary, with a step size of 25 nm. a) shows the infinite medium (IM) term for an edge TD. b) shows the surface relaxation (SR) term for an edge TD. c) shows the combined effect of IM and SR edge TD terms. d) shows the effect of a screw TD on ω_{yx} which is purely surface relaxation. e) shows the total effects of a mixed TD.

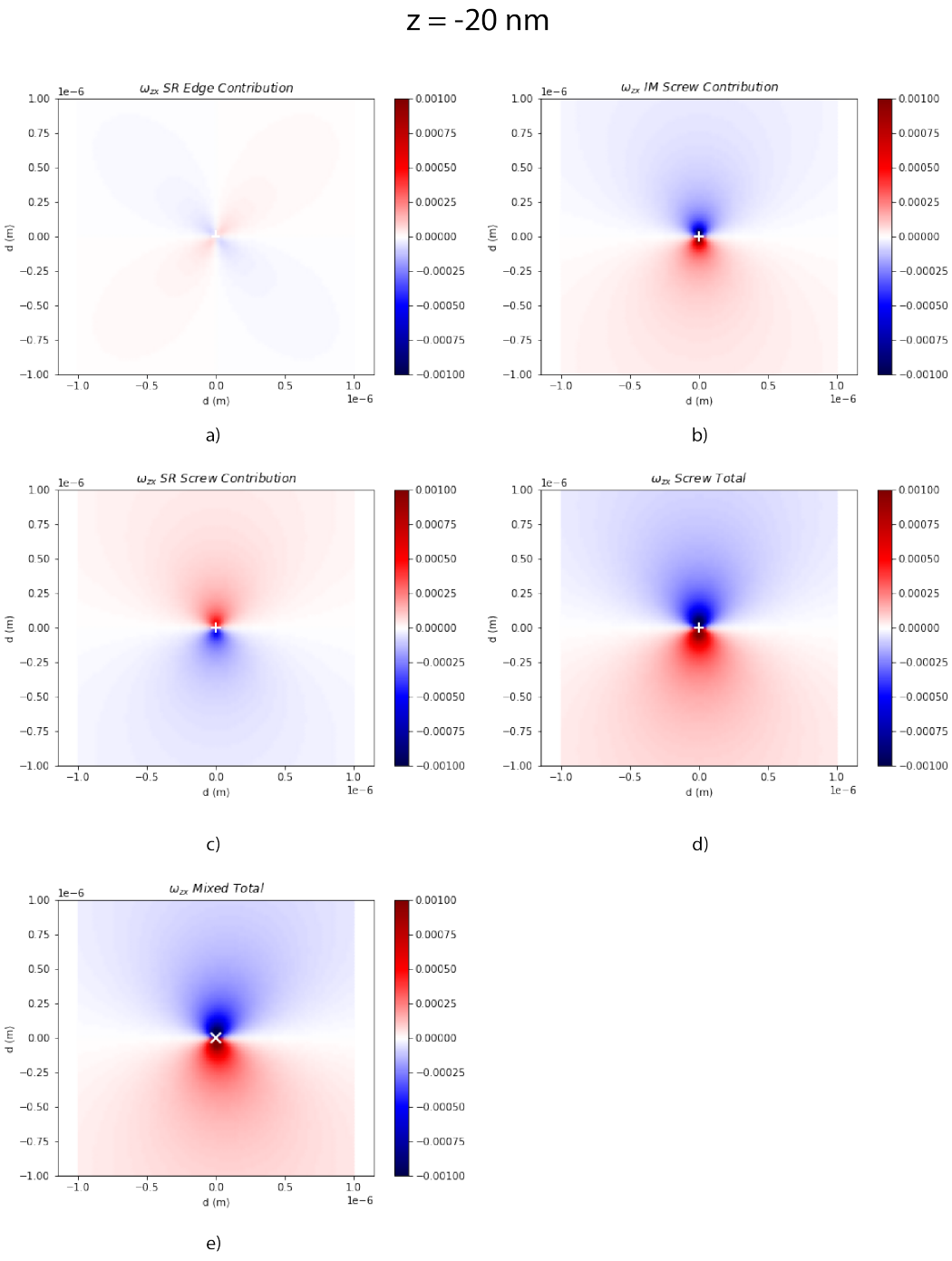

Figure 4.10: Simulations of lattice rotation ω_{zx} in c-oriented GaN at 20nm below the surface boundary, with a step size of 25 nm. a) shows the surface relaxation (SR) term for an edge TD. b) shows the infinite medium (IM) term for a screw TD. c) shows the SR term for a screw TD. d) shows the total effect of a screw TD. e) shows the total effects of a mixed TD.

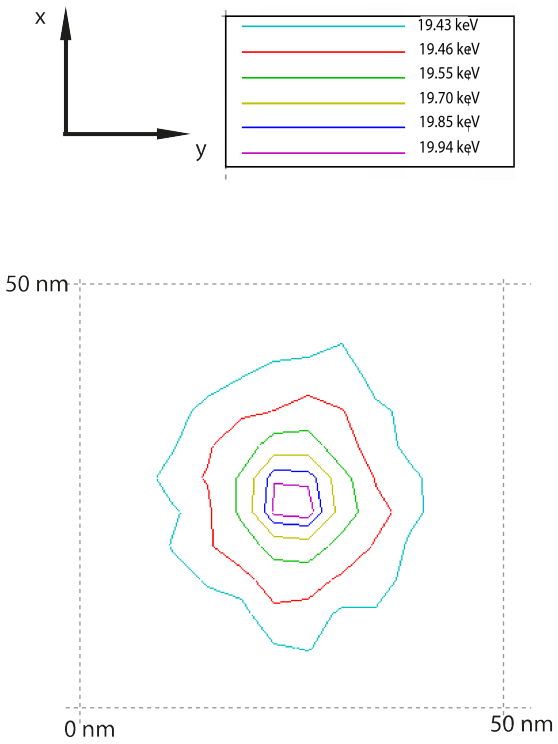

Figure 4.11: x-y plane view of a Monte Carlo simulation of 1000 electrons incident on a flat 900 nm thick GaN thin film. The minimum energy of the plotted electrons is 19.4 keV. This shows the approximate size of the interaction volume from which BSEs diffract out of the sample. The coloured lines represent the average energy by position of the electrons in the interaction volume. This Monte Carlo simulation model takes only scattering into account and not diffraction processes.

energy (20 keV). The outer light blue line is the boundary of the interaction volume while other concentric lines represent increases in electron energy from 19.4 keV up to 20 keV. The approximate size of the interaction volume is then 40 nm, where the interaction volume is roughly symmetric (becoming more symmetric in shape as the simulated electron number approaches infinity). For an EBSD measurement with a step size of 25 nm in this geometry, information from each point (pixel) in the raster scan will overlap with neighbouring pixels. To take this effect into account, the simulated maps can then be binned to reduce the effective step size to closer to 40 nm. The binning simply means that values within intervals of 40 nm of each other are replaced by a single value representative of them both.

The elongation due to tilting can then be visualised by plotting the same Monte

Carlo plot as in Fig. 4.11 but with a 70° tilt (Fig. 4.12). The elongation of the interaction volume in the y-direction increases to 3-4 times that in the x-direction. Consequently, further binning of the simulations can be performed in the y-direction to simulate the effects of this. However, this is not as simple as increasing the binning by a factor of 3-4. In fact, consulting Fig. 3.3, it can be seen that when the beam is incident on a tilted sample, the interaction volume samples a region mostly below the point at which the beam is dwelling (negative y direction in specimen coordinates). This means when binning further in the y-direction, greater weight must be given to the contributions from below each pixel than from above. This is important and has a significant impact on the final perturbed strain distribution. This is straightforward in Python and means that for every pixel in the strain simulation, there is a contribution from the 2-3 pixels below as well. When there are dipoles oriented around the x-axis in the strain simulations, as in Fig. 4.8d) for example, this means the upper lobe of the dipole is sampling the one below it, reducing the overall effective strain measured at that point. Meanwhile, the bottom lobe of the dipole samples the the no-strain region below it, meaning its value stays the same. This creates asymmetry in the strain distribution with the upper lobe having a lower magnitude than the bottom lobe. This has a pronounced impact when introducing the final step of the perturbation: limiting the simulation to a given strain resolution. By setting a threshold for the strain resolution and setting all values below that to zero, it is apparent that the upper lobe can disappear entirely while the bottom lobe can remain. In fact, for the screw component of ϵ_{zx}, this is exactly what happens. Fig. 4.13 shows the ϵ_{yx} and ϵ_{zx} simulations for edge, screw and mixed TDs with the additional effects of interaction volume size/elongation and strain resolution taken into account for a 20 keV electron beam. The strain resolution limit was taken to be 2×10^{-4}, the approximate precision of strain measurements using the pattern matching approach (estimated from the average full width at half maximum of the e11 and e22 strain components for a Si wafer). In order to simulate an approximate spatial resolution, the initial simulations were first binned down to a step size of 40nm (effectively simulating a flat sample) and then each pixel had a weighted average contribution from the two pixels below it (reducing the

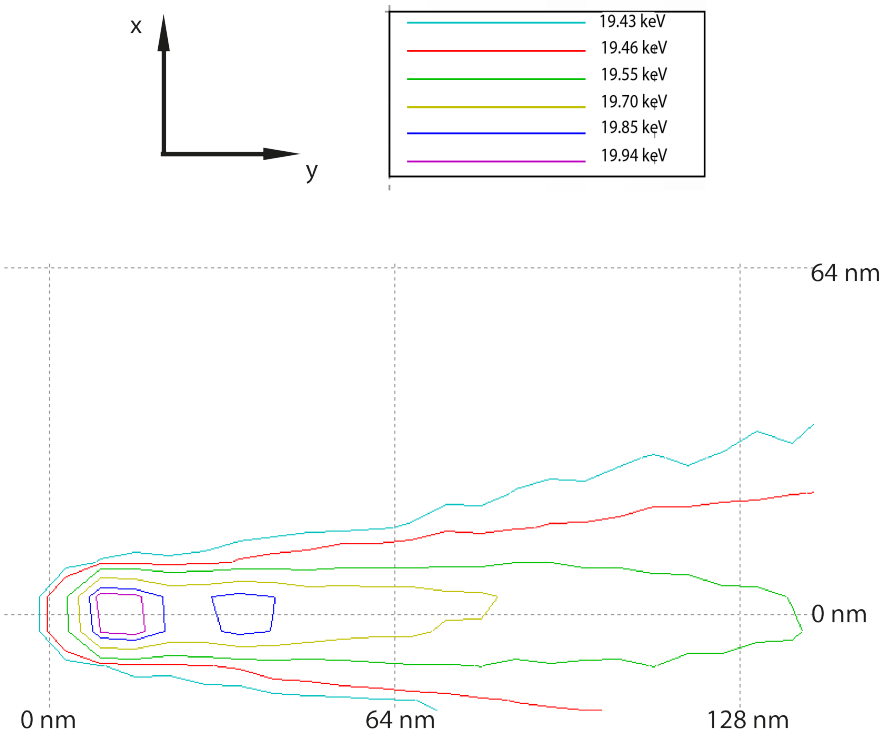

Figure 4.12: x-y plane view of a Monte Carlo simulation of 1000 electrons incident on 900 nm thick GaN thin film tilted 70° to the horizontal. The minimum energy of the plotted electrons is 19.4 keV. This shows the approximate size of the interaction volume from which BSEs diffract out of the sample. The coloured lines represent te average energy by position of the electrons in the interaction volume.

y-resolution by a factor of 3).

The shear strain component ϵ_{zx} for a screw TD (Fig. 4.13a)) shows the behaviour described previously, where the upper lobe has disappeared due to the scan at that point effectively also sampling the bottom lobe and reducing its magnitude below the strain threshold. The ϵ_{zx} for an edge TD ((Fig. 4.13b)) disappears below the threshold entirely. However, its effects are not completely gone when considering the mixed TD ((Fig. 4.13e)). In fact, the combination of the magnitude of the edge component and the screw component for a mixed TD means that there is a slight noticeable difference between a) and e). This is such that the ϵ_{zx} strain distribution for a mixed TD slightly narrows compared to a screw TD. That is to say, when combined with the strain from the screw component of a mixed TD, the edge component does have a measurable effect above the strain resolution threshold. However, in practice, the ϵ_{zx} strain associated

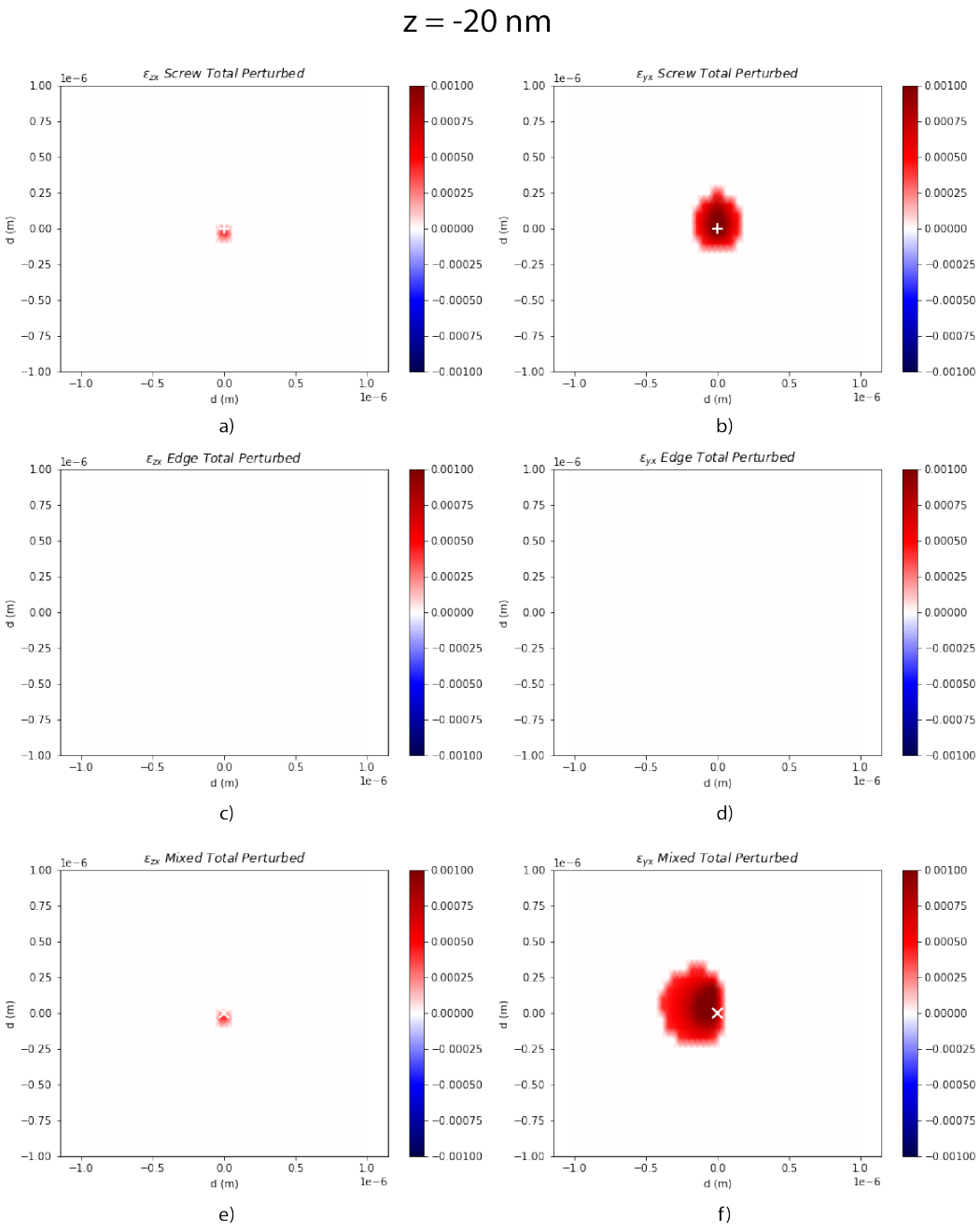

Figure 4.13: Simulations of shear strain components ϵ_{yx} and ϵ_{zx} for edge, screw and mixed TDs in GaN. Mixed TDs are a combination of the screw ([**0001**]) and edge ($\mathbf{b} = [11\bar{2}0]$) components. These have been perturbed so as to simulate the effects of an interaction volume for a 20 kV beam and a strain resolution of 2×10^{-4}. In order to estimate the effects of an interaction volume, binning was first increased to represent the spatial resolution imposed by the size of the volume for a flat sample. The y-component of the strain was then elongated, reducing the spatial resolution in the y-direction further, by filtering such that each pixel had weighted contributions from the two pixels below.

with pure edge TDs is so low that it will be undetectable.

For the perturbed shear strain component ϵ_{yx}, the screw TD has a slightly shorter range (Fig. 4.13b)) compared to the non-perturbed version (Fig. 4.7) which is simply due to the strain resolution limit. Similarly, as for the ϵ_{zx} perturbed simulations, the ϵ_{yx} strain associated with an *individual* edge TD is below the strain resolution limit (Fig. 4.13d)). However, it again does affect the mixed TD due to its combination with the screw component (Fig. 4.13f)) and for regions of GaN where same-sign edge TDs are very close to one another, the magnitude of the net ϵ_{yx} shear strain associated with them will be higher than the strain resolution limit, meaning they are detectable.

4.6 Summary

Analytical shear strain and lattice rotation simulations have been performed for the case of threading dislocations in GaN at both the surface boundary and a sampling depth of 20 nm below the surface- an approximate sampling depth for an electron beam of 20 keV. Ultimately, the simulations show that strong surface relaxation effects from screw (and therefore mixed) TDs means that their associated strain is significant in both in-plane and out-of-plane shear strain and lattice rotation measurements. On the contrary, edge TDs have small surface relaxation effects and so, in practice, are only visible in the in-plane components. This has great significance for EBSD measurements as it means screw component (pure screw and mixed TDs) should be distinguishable from pure edge TDs if in-plane and out-of-plane shear strain and lattice rotations are mapped, providing a mechanism to help identify TD types. This is summarised for clarity in Table 4.1.

Moreover, the shear strain simulations were perturbed to impose the effects of the interaction volume at 70° tilt and the minimum detectable strain (strain resolution). These simulations, while a rough emulation of EBSD measurements due to the absence of any consideration for diffraction effects, estimate that the dipole nature of screw component TDs may vanish in ϵ_{zx}, with only the bottom lobes visible. Moreover, the ϵ_{yx} distributions for screw and mixed TDs should be considerably more diffuse (longer range) than those for ϵ_{zx}.

TD Type	SR In-plane	SR Out-of-plane	IM In-plane	IM Out-of-plane	Visible In
Edge	Small	Small	Large	0	In-plane
Screw	Large	Large	0	Large	In/out-of-plane
Mixed	Large	Large	Large	Large	In/out-of-plane

Table 4.1: Summary of the relative magnitudes of in-plane and out-of-plane surface relaxation (SR) and infinite medium (IM) effects associated with different types of TDs in GaN. The last column shows which TDs are visible in the in-plane and out-of-plane components of orientation and strain EBSD plots for the spatial, angular and strain resolution limits imposed by the current method.

Chapter 5

Misorientation and Strain Mapping Using EBSD for Threading Dislocation Identification

5.1 Introduction

Having demonstrated the ability to map/image individual threading dislocations in Chapter 3 and simulate strain and lattice rotations in Chapter 4, this chapter combines the techniques and knowledge developed so far to investigate real misorientation and strain associated with TDs in a variety of GaN thin films.

In Chapter 2 the detrimental effects of TDs in GaN thin films were discussed. A brief summary of the main points follows. TDs are centres of non-radiative recombination [1,2], which can limit the efficiency of LED-based devices and reduce carrier mobility via scattering [3]. Moreover, as GaN is piezoelectric, variations in strain associated with TDs can spawn variations in polarisation. This results in regions of reduced carrier mobility [87] and strain can also alter local bandgaps [5].

Conventionally grown epitaxial GaN thin films generally have TD densities in range of low 10^8cm^{-2} to high 10^9 cm^{-2}. As has been explained, TDs have three main types

in GaN (edge, screw and mixed) with proportions varying from sample to sample based on growth conditions [6]. While there is evidence that all types of TDs in GaN cause non-radiative recombination [7], the electronic properties of TDs can vary with type [8]. Moreover, the relatively high misorientation associated with them means that their density, types, and distributions can have a large impact on the subgrain structure of the thin films. Similarly, strain distributions associated with edge, screw and mixed TDs also differ as shown in Chapter 4, meaning the strain profile across a GaN thin film is strongly dependent on TD types, density and distributions as well. This makes understanding TD types and distributions along with their misorientation and strain extremely important for future GaN-based device development.

There are three alternative techniques to EBSD that offer TD identification and associated strain and misorientation measurements: TEM [10-14], Raman spectroscopy [15-18], and X-ray diffraction [19-21]. However, TEM relies on specially prepared electron transparent samples, which is both time-consuming and destructive, while also being limited in its strain and misorientation resolution [13, 14]. X-ray on the other hand is a bulk technique, and while recently showing promise in nanoscale mapping of strain and lattice rotations [22], it does not yet have sufficient spatial resolution to resolve individual threading dislocations. Raman spectroscopy relies on indirect measurements related to the Raman shift and is often restricted to certain components of the strain tensor.

Atomic force microscopy (AFM) and electron channeling contrast imaging have sufficient spatial resolution to resolve individual TDs and determine densities and types [23-28] [14, 122, 123, 126]; however, both lack quantitative misorientation and strain information.

In recent years, the capabilities of EBSD for mapping misorientation and strain in nitride thin films have been demonstrated [12, 15, 125] [29-32], while EBSD has also proven to be an effective imaging technique for TDs in GaN (Chapter 3). It is a non-destructive technique and allows large areas of thin films to be mapped in a relatively short amount of time. However, misorientation maps produced by EBSD have not been used to identify threading dislocation types, and EBSD has also been

limited by its spatial resolution such that the strain profiles of individual TDs have not been resolved. Transmission Kikuchi diffraction (TKD), a technique closely related to EBSD but using electron transparent samples, has shown the ability to map the strain distributions associated with individual TDs in Tungsten [35] [42]; however, similar to TEM, this requires specialist sample preparation.

In this chapter, sufficient spatial resolution is demonstrated to map the strain and misorientation, using a pattern-matching approach based on dynamical simulations, associated with individual TDs in a variety of GaN thin films. Using the misorientation information, and the context provided by the simulations in Chapter 4, it is possible to distinguish between screw-component and pure edge TDs. Furthermore, high spatial resolution images of the TD distributions and the subgrain structure are provided such that TD densities are also calculated and dominant misorientations (in-plane and/or out-of-plane) are identified.

5.2 Methods of Mapping Misorientation

Once an EBSD dataset has been acquired and crystal orientations for each EBSP have been determined (as described in Section 2.3.4 *Indexing*), there are numerous ways in which the orientation information can be visualised. This section describes the (mis)orientation mapping methods relevant to the content later in this chapter. All maps have been produced using the open-source crystallographic MATLAB toolbox MTEX [153].

5.2.1 Grain Reference Orientation Deviation Maps

Grain reference orientation deviation (GROD) maps are an important subset of misorientation maps. They map the relative difference in orientation between each EBSP and a user-defined reference from the dataset. This reference can be a single EBSP or the average orientation over a region of interest (ROI) in the acquired map. For c-oriented GaN, where misorientations are small ($< 0.5°$) a useful reference can actually be the mean orientation of the entire dataset, as the Cartesian z-direction should then roughly

be aligned with the crystal c-direction. The GROD map is then a measure of the rotation required to bring the crystal reference frames of each EBSP into coincidence with the mean crystal reference frame, where the c-axis is aligned with the specimen z-direction. The choice of reference has a significant impact on the visual appearance of GROD maps, and so careful consideration must be taken when deciding this and when interpreting the final maps.

The simplest GROD map is the GROD Angle, which plots the net misorientation between each EBSP and the reference point. This is most often plotted as an absolute value, with no regard for the direction of misorientation. Thus, it can be useful to interrogate how large misorientations occurring in the sample or between neighbouring ROIs are, but not much more beyond this. The GROD Angle map can, however, be decomposed into components representing the misorientation around the axes of a simple xyz Cartesian reference frame. This decomposition allows the user to interrogate around which axis/axes the misorientation occurs and to compare in-plane misorientation (GROD Z) with out-of-plane misorientation (GROD X and GROD Y). Example GROD Angle and GROD XYZ maps are shown in Fig. 5.1.

The decomposition of misorientation axes can be taken one step further in the GROD Axis map. An example of this map, along with its key, is shown in Fig. 5.2. For this map, each black dot on the key is a pixel in the EBSD map. When working in the specimen coordinate system, the misorientation axis can be oriented in any direction in 3 dimensions, and so upper and lower keys are used to show the misorientation axes directions in the upper and lower parts of a 3D sphere. The centre of the key is aligned with the z axis, meaning all points that are black or white represent purely in-plane misorientation. The edges of the key represent misorientation axes perpendicular to z, while areas in between are misorientation axes tilted with respect to z below 90°. As each region of the key is assigned a colour, the black dots occupying it then have their corresponding pixels coloured in the GROD Axis map according to the key, allowing the spread of misorientation axes and their directions to be visualised in the EBSD map. The saturation of the colour in the map is dictated by the magnitude of the misorientation angle around the given axis. i.e., the bigger the misorientation, the

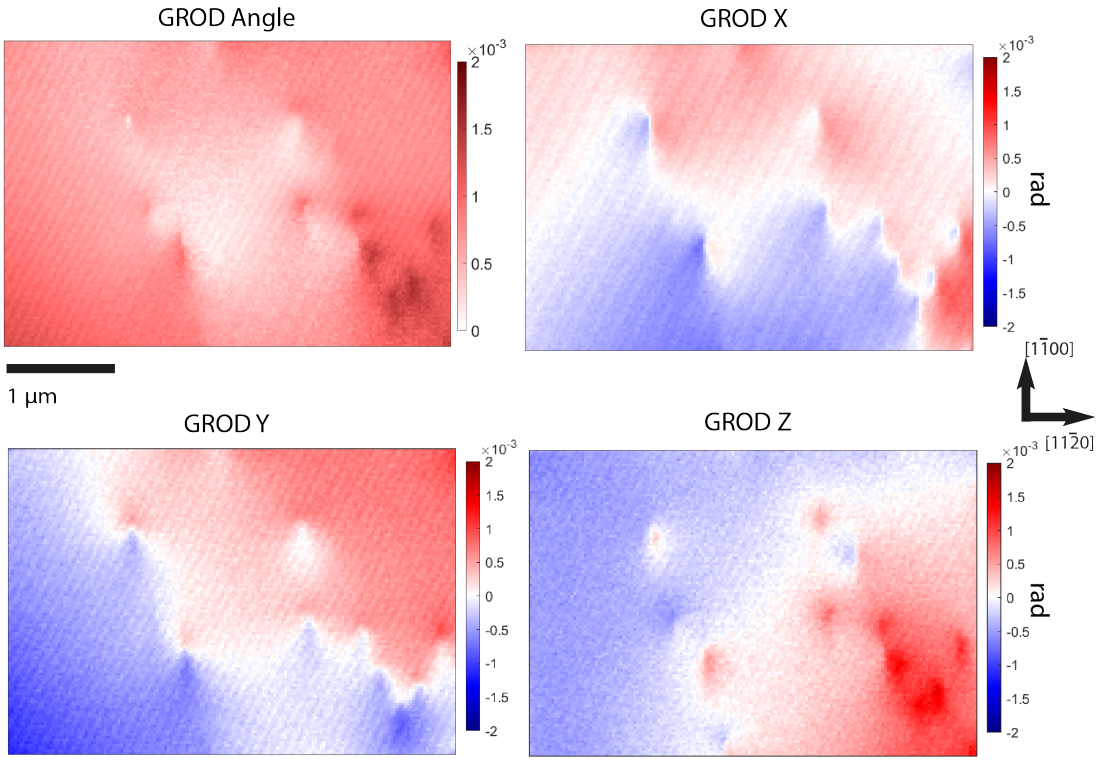

Figure 5.1: Grain reference orientation deviation (GROD) Angle map showing the total misorientation in a GaN thin film (Sample C in Section 5.3) measured using a 20 kV electron beam. The components of this misorientation are then given around each axis of the Cartesian reference frame. Misorientation around Z (GROD Z) is denoted in-plane misorientation, while misorientation around X and Y denotes out-of-plane misorientation. The level of saturation of the colour indicates the magnitude of the misorientation angle. The user-defined threshold chosen for complete saturation is 3.5 mrad in this example.

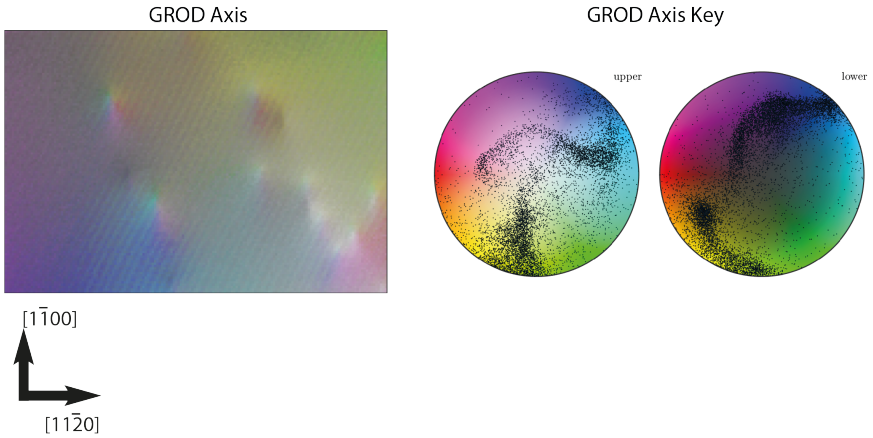

Figure 5.2: Grain reference orientation deviation (GROD) Axis map showing the distribution of misorientation axes in a GaN thin film measured using a 20 kV electron beam. The colour on the GROD axis map references a direction in the key for the misorientation axis. Each black dot in the key corresponds to a pixel in the GROD Axis map The centre of the key (white/black) denotes purely in-plane misorientation, i.e. a misorientation axis parallel to z. The points/colours at the periphery of the key denote misorientation axes 90° from z, while colours in between denote a misorientation axis somewhere in between. The magnitude of rotation around the misorientation axis at which the colour saturates is 3.5 mrad (0.20°) for this map. When working in the specimen coordinate system, the misorientation axis can be oriented in any direction in 3 dimensions, and so upper and lower keys are used to show misorientation axes directions in the upper and lower parts of a 3D sphere.

stronger the colour. The threshold at which the colour fully saturates is user-defined, and for this map is equal to 3.5 mrad. Ultimately, the map is particularly useful as the key shows whether the distribution of the points in the map are predominantly in-plane (located at the centre of the key) or out-of-plane (located at some distance away from the centre). The map then tells the user exactly in which regions this misorientation occurs and to some extent the relative magnitude of it, although visually distinguishing between colour saturation levels can be challenging. In Fig. 5.2, for example, most of the points in the GROD axis key are distributed away from the centre, indicating the map is dominated by out-of-plane misorientation, with some white (associated with in-plane misorientation) located at the TDs, which may indicate they at least have an edge component. A more thorough analysis of GROD axis maps is explored in the upcoming Section 5.4 *VDCOM and Mapping Misorientation.*

5.2.2 The Curvature Tensor

The curvature tensor, κ, [154] is a rank 2 tensor that is formed by taking the directional derivatives, x,y and z (specimen reference frame), of the pixel to pixel net misorientation around the x, y and z axes. It can be thought of then as the derivative of the GROD XYZ maps, taken in both the x and y directions. It is of the form:

$$\kappa = \begin{bmatrix} \frac{d\theta_x}{dx} & \frac{d\theta_x}{dy} & \frac{d\theta_x}{dz} \\ \frac{d\theta_y}{dx} & \frac{d\theta_y}{dy} & \frac{d\theta_y}{dz} \\ \frac{d\theta_z}{dx} & \frac{d\theta_z}{dy} & \frac{d\theta_z}{dz} \end{bmatrix}$$

Where $d\theta_x/dx$ would indicate the derivative of the misorientation around the sample x axis, moving in the x direction across the sample surface. The obvious exception is that EBSD data, while sampling some extended depth, only shows orientation information for a 2D section of the sample, and so the z directional derivatives (in the direction of increasing sample depth) are unavailable.

For the c-axis oriented GaN samples used in this thesis, the curvature tensor gives valuable information on the extent of in-plane and out-of-plane rotation taking place close to the sample surface. To clarify, any non zero value for the $d\theta_z$ directional derivatives would indicate in-plane rotation and any non-zero values for the $d\theta_x$ and the $d\theta_y$ directional derivatives would indicate out-of-plane rotation. Each component of the curvature tensor can be plotted as an individual map, showing how the magnitude of the component changes across the sample surface. For EBSD measurements where misorientation measurements are local and relative to a reference, TDs are a dominant source of misorientation in GaN, and so the curvature tensor should, theoretically, pick out the TDs quite well.

5.2.3 Weighted Burgers Vector

Similar to the curvature tensor is the Weighted Burgers Vector (WBV) [155, 156]. It is defined as the sum, over all types of dislocations, of [(density of intersections of dislocation lines with a map) $\times$ (Burgers vector)]. Mathematically, this is given as [156]:

$$W_i = \sum_N [\rho^{(N)} l_3^{(N)}] b_i^{(N)} \tag{5.1}$$

Where W is the weighted Burgers vector, and ρ and b are the dislocation density and Burgers vector of each type of dislocation (denoted as N). l is the line direction of each type of dislocation and is given the subscript 3 to show it is the component parallel to the specimen z direction. This is where the 'weighting' comes from in the WBV method. The value of l_3 is equal to 1 for dislocations with line vectors parallel to z and decreases to 0 for line vectors perpendicular to z. The subscript i denotes the type of TD (edge, screw, mixed) with a particular Burgers vector. Put simply then, the WBV is, in theory, a measure of the curvature due to the Burgers vector of TDs weighted by the line direction of the TDs.

Where the curvature tensor is computed via a differential method, the WBV method typically computes the curvature via an integral method. This is done by using a user-defined kernel (square or circular), e.g. 5×5 pixels, within which the orientation content is integrated over. Mathematically, this is the same as the differential method, however as it offers the ability to integrate over larger kernel sizes, whereas the curvature is just the nearest neighbour differential, in certain cases it may have the advantage of significantly reducing noise. The WBV content can be broken down into components showing curvature as a result of dislocations with Burgers vectors that have components parallel to the x, y, and z specimen axes. These components can then be plotted in individual maps, denoted WBVx, WBVy and WBVz respectively. If the sample is oriented such that the x specimen direction is parallel to the $[11\bar{2}0]$ direction, for example, then the in-plane curvature due to all edge TDs would be visible in WBVx. This is even true for other symmetrically equivalent edge Burgers vectors, as, due to the six-fold-symmetry of the hexagonal system, they are separated by intervals of 60°, meaning they will at least still have a *component* of their Burgers vector in the x direction. It's possible misorientation due to edge TDs with these other symetrically equivalent Burgers vectors may show slightly weaker, however once this has been integrated over within a kernel it would be difficult to distinguish them from other edge TDs based on magnitude of the curvature alone. This would also be complicated by scenarios where TDs are very

close together. WBVx would also be affected by the misorientation associated with the surface relaxation of screw-component TDs (as shown in Chapter 4, *Simulating Strain and Lattice Rotations in GaN*, Subsection 4.4 *Simulation of Strain and Lattice Rotations in GaN at fixed non-zero z*).

The WBV approach suffers from similar limitations to the curvature tensor which are inherent to EBSD analysis techniques due to the geometry of the measurment. Firstly, information is restricted to two dimensions. Where the curvature tensor is unable to determine gradients in the specimen z direction, WBV also cannot perform the integral method along this axis. Additionally, curvature detected as a result of dislocation lines intercepting the sample surface is weighted by the angle between the dislocation line and the surface plane. As dislocation lines become more inclined they will have a lower effect on the calculated WBV value, with dislocation lines parallel to the surface not contributing at all. Moreover, the WBV method, and curvature tensor method, do not give a definitive answer as to what causes the distortion. The WBV method simply tests the compatibility of measured distortion with that of the Burgers vectors of known dislocations.

5.2.4 Interpreting Misorientation and Strain Maps Using Simulations

Prior to analysing any misorientation or strain distributions, it is important to understand the significance of the in-plane and out-of-plane strain and misorientation associated with TDs. Looking back to the simulations in Chapter 4 Section 4.4 *Simulation of Strain and Lattice Rotations in GaN at Fixed Non-zero z*, it is clear that all three types of TDs (edge, screw and mixed) contribute strongly to in-plane strain and lattice rotations. For the misorientation maps previously discussed this means it is expected, based on the simulations, that there is strong contrast from all TD types in GROD Z and WBVx . Meanwhile, all TDs will contribute strongly to the contrast in the in-plane shear component ϵ_{yx}.

However, for out-of-plane strain and misorientation, the contribution from screw TDs is significantly higher than that from edge. This means it is expected, based on the simulations, that screw and mixed TDs will show much stronger contrast than edge

in GROD X/Y, WBV Z and shear strain ϵ_{zx} maps. In fact, going by the simulations, it is likely that edge TDs will be effectively invisible in the experimentally acquired maps as the strain and angular resolution of EBSD is similar to the expected magnitude of the out-of-plane strain and misorientation associated with the surface relaxation of edge TDs.

A consequence of this is that edge TDs can be identified by comparing, for example, WBVx and WBVz and seeing which TDs show strong in-plane misorientation but minimal/no out-of-plane misorientation. The Weighted Burgers Vector approach is preferred to the curvature tensor in this chapter due to the lower noise (facilitated by the bigger kernel size of WBV versus the nearest neighbour differential approach of the curvature tensor) and better numerical properties. Additionally, for GROD Axis maps, the fewer edge TDs there are, the more balanced the out-of-plane and in-plane misorientation becomes (i.e. in-plane misorientation is less dominant), leading to less clustering in the middle of the GROD Axis key.

Ultimately, the in-plane strain and misorientation associated with the surface relaxation of screw TDs means they are visible in all components of GROD, WBV and the strain tensor that can be measured by EBSD. However, due to the extremely small surface relaxation associated with edge TDs, they are not visible in the out-of-plane components of these measurements. By then comparing out-of-plane and in-plane components, edge TDs can be directly identified.

5.3 Materials

The first sample used in this chapter, denoted Sample A, is a 1600 nm thick thin film grown on a *c*-plane sapphire substrate via MOVPE. A 30 nm GaN nucleation layer was grown at 525 °C. This layer was annealed briefly at a temperature of 1023 °C prior to the epitaxial growth of the sample. More information on the growth process is available in [147]. Samples B and C are GaN thin films grown on sapphire substrates via a 2D-3D growth method similar to that outlined in [70], with varying growth conditions such that the coalescence time and consequently TDD content was different between the two

samples. Samples B and C were provided by the University of Cambridge.

5.4 VDCOM and Mapping Misorientation

The first step in comparing samples A, B and C is to interrogate the TD distributions visually via VDCOM and reconcile this with the associated misorientation via the GROD Axis. This can give information on subgrain size and whether the subgrains are misoriented predominantly in-plane or out-of-plane. The latter then allows one to make assumptions about the local TD types: more out-of-plane misorientation than in-plane misorientation may indicate more screw component TDs and vice versa. Moreover, using the VDCOM images for multiple datasets from each sample it is possible to count TDs and build up TD density estimates with relatively high statistics.

Figure. 5.3 shows the VDCOMy images produced from the bottom half of EBSPs in a dataset for each sample (a,b,c), and the corresponding GROD Axis plots (d,e,f). Looking at the VDCOMy plots, it is clear from a visual inspection that samples A and B have a much greater TD density than sample C. This is confirmed from a rigorous count of TDs across many different datasets for each sample. In fact it was found that sample A has a TDD of $8 \pm 0.6 \times 10^8$ cm^{-2} (from 1800 TDs), sample B has a TDD of $5 \pm 0.4 \times 10^8$ cm^{-2} (from 440 TDs) and sample C has a TDD of $1.8 \pm 0.1 \times 10^8$ cm^{-2} (from 390 TDs).

From the contrast in VDCOM for these datasets it is difficult to discern any subgrain structure. However, looking at GROD Axis the subgrain structure becomes clear as the boundaries between misoriented regions become much more visible. From a qualitative perspective, both samples A and B have much smaller subgrains than sample C. This can be expected as the misorientation associated with TDs dominates the subgrain structure, and as sample C has considerably fewer TDs it is expected that the subgrains should be larger. All three samples exhibit both in- (black/white regions in GROD Axis key) and out-of-plane misorientation (color regions in GROD Axis key). However, the presence of stronger black/white regions in samples A and B indicates in-plane misorientation is more dominant than in sample C. The misorientation axes in A and B are also distributed around the z direction (centre of GROD Axis key), while those

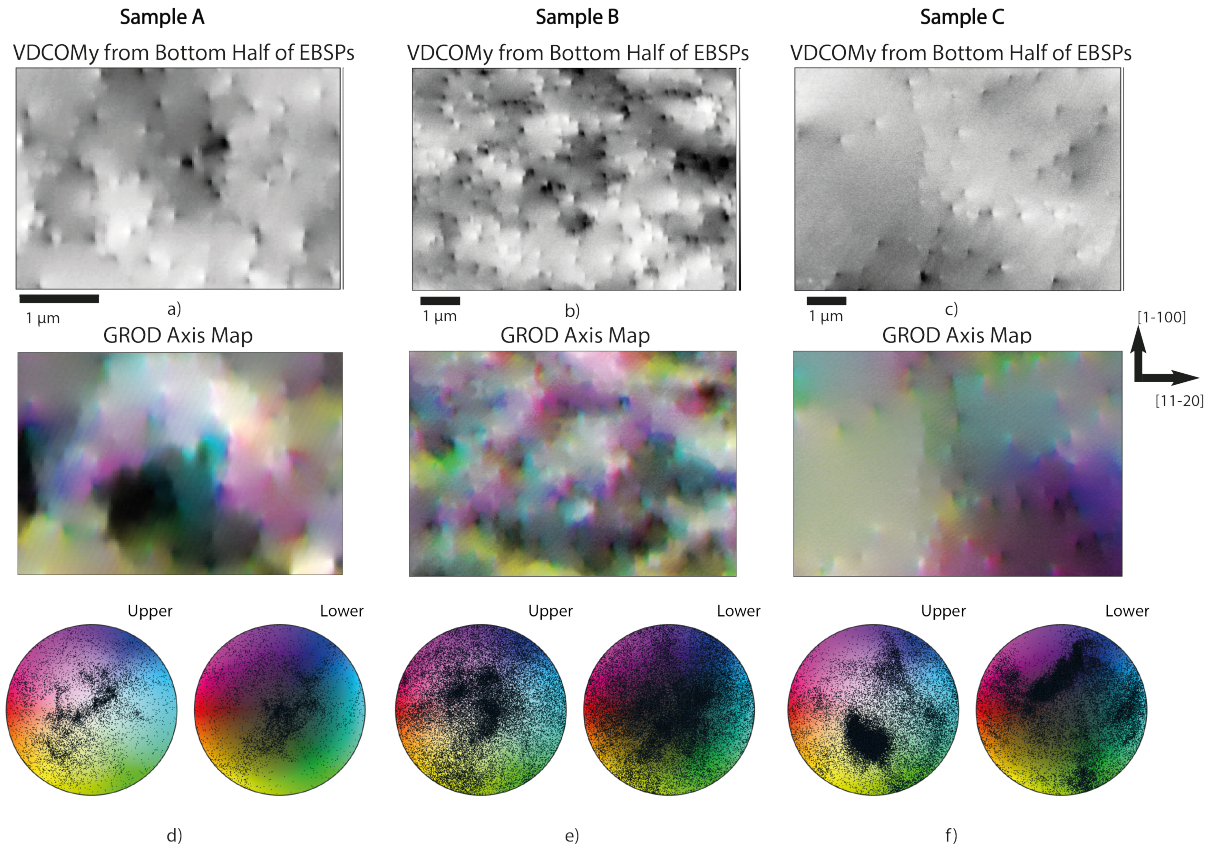

Figure 5.3: a-c) Virtual diode centre of mass (VDCOM) images of dislocations threading to the surface of samples A, B and C acquired using the bottom half of EBSPs. d-f) Corresponding Misorientation Axis maps with associated keys. The colour on the Misorientation Axis map references a direction in the key for the misorientation axis. Each black dot in the key corresponds to a pixel in the Misorientation Axis map The centre of the key (white/black) denotes purely in-plane misorientation, i.e. a misorientation axis parallel to Z. The points/colours at the periphery of the key denote misorientation axes 90° from z, while colours in between denote a misorientation axis somewhere in between. The key colour saturation value is 0.15° and the misorientation was calculated with respect to the mean in each sample.

for sample C are more off-axis. This may indicate that the ratio of screw component TDs is higher in sample C. Moreover, the in-plane misorientation sample A exhibits approaches the saturation value of the key (0.15 degrees). This is higher than for both samples B and C, suggesting sample A may have the highest proportion of edge TDs.

The subgrains walls/boundaries are also decorated by the TDs, which is intuitive as the misorientation associated with these TDs is in fact the same misorientation that gives rise to the subgrain structures. As the TDs in the three samples are, for the most part, clearly separated from one another, these subgrain boundaries can be considered 'low-angle' boundaries (see discussion on high-angle vs low-angle boundaries in Chapter 2 Section 2.1.2 *Types of Defect and Effects on Crystal Lattice*. Moreover, the subgrains which are dominated by black/white colour in the GROD axis are bounded by twist boundaries (in-plane misorientation) which would indicate the TDs decorating them are of edge type. Conversely, those subgrains showing non-black/white colour will have strong out-of-plane misorientation and can be considered to have twist subgrain boundaries, indicating they are decorated by mixed or screw TDs. For the cases where mixed decorate the boundary, there will of course be a combination of tilt and twist. It is then obvious from the GROD axis maps that Sample A and Sample B contain a higher degree of twist and a higher number of pure twist boundaries than Sample C, indicating Sample C has a lower proportion of edge TDs.

Other than the visual inspection of the GROD Axis plots, the breakdown of in-plane and out-of-plane misorientation can be quantitatively analysed by looking at the histograms corresponding to the GROD X, Y and Z plots for each sample. These are shown in Figure. 5.4. These histograms were compiled for each sample by using one reference point and several datasets, in order to improve the statistics compared to using just one dataset for each. The areas covered were $223\mu m^2$, $92\mu m^2$, and $218\mu m^2$ for samples A, B and C respectively. The histogram widths were then calculated by subtracting the 2nd percentile value from the 98th percentile value. This eliminated the impact of anomalies on the calculated widths where extremely high misorientations would occur but were not representative of the actual spread of misorientations in a sample. The ratios of the rotation around the X,Y and Z axes are also shown in the

plots. Overall, the relative in-plane/out-of-plane data shown in the GROD Axis plots for the individual datasets in Figure. 5.3 are reciprocated in the histograms, indicating that the single datasets are fairly representative of the total area sampled for each sample. In Figure. 5.4a) it is clear that the rotation around z in Sample A is dominant and also greater than that in the other two samples. This is a result of the high TDD and suggests there is also a relatively high percentage of pure edge TDs in Sample A. Furthermore, Sample C shows the smallest difference between the magnitudes of out-of-plane and in-plane misorientation, again suggesting it has the highest relative number of screw-component TDs. The non-Gaussian nature of Sample C is likely due to the much larger subgrains, resulting in the subgrains causing peaks in the histogram. If a much larger area was sampled then this may tend towards a Gaussian distribution.

There are, however, some important things to bear in mind when analysing the misorientation histograms this way. Histogram broadening can be dependent on TD clustering and the sign (positive or negative) of the TDs. For example, a cluster of screw TDs with the same sign will result in a high net misorientation while the same number of screw TDs with 50% having a positive sign and 50% negative will lead to approximately 0 net misorientation. However, on the large scale for these samples there is no obvious evidence of same sign TD clustering and so it is suggested that the current treatment is acceptable for this case.

5.5 Identification of Threading Dislocations and Strain Mapping

After getting a general sense of subgrain size and making some predictions about TD types based on measured misorientation, individual TDs will now be identified as either pure edge or as having a screw component (screw or mixed type TDs). Based on the simulations in Chapter 4 this can be done by identifying which TDs contribute in-plane and/or out-of-plane misorientation and strain. The TDs with only associated measurable in-plane misorientation and strain will be pure edge TDs, while all others will be screw component. Unfortunately, as screw TDs have a large surface relaxation

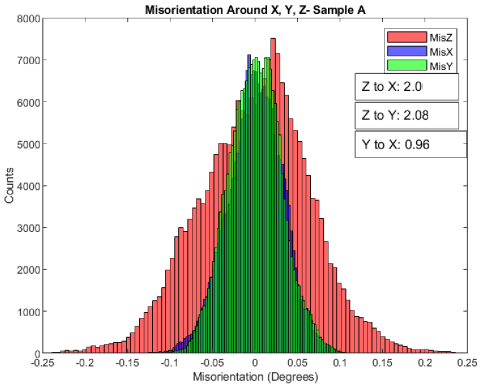

a)

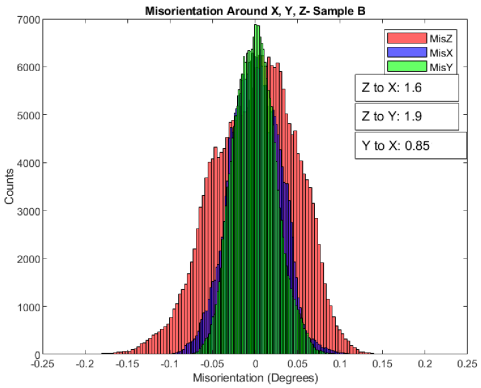

b)

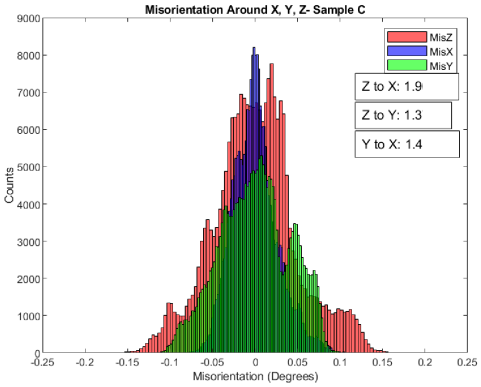

c)

Figure 5.4: a-c) Histogram plots showing misorientation around the sample x,y and z axes for samples A, B, and C respectively. The histogram widths were calculated by deducting the 2nd percentile value from the 98th percentile value and the ratio between the three misorientations are shown using these.

effect in both misorientation and strain, it is not possible in plan-view to differentiate between pure screw TDs and mixed TDs at this time.

Rather than using GROD X, Y and Z for the misorientation, it is better to use the Weighted Burgers Vector (WBV) approach introduced earlier in this chapter. As the WBV approach integrates the misorientation (calculating what is known as curvature) it is effectively reference-independent, whereas with GROD plots it can be hard to see TDs that have a misorientation close to the reference. The integration also makes the peaks due to TDs much more visible, and neighbouring TDs can be separated from one another more easily. To investigate the in-plane and out-of-plane of the WBV content, the plots WBV Z and WBV X will be used. These correspond to the curvature associated with a Burgers vector that has a component parallel to the z direction (screw TDs) and with a Burgers vector that has a component parallel to the x direction (edge TDs), respectively. As the specimen x direction is aligned with a $[11\bar{2}0]$ direction, all edge TDs with that Burgers vector and symmetrically equivalent Burgers vectors will have a component in the x direction. This means the curvature associated with this has been integrated over, all edge TDs will appear in the WBV X plots. Consequently, WBV X can simply be thought of as the in-plane curvature (misorientation) content and WBV Z as the out-of-plane curvature content. The in-plane and out-of-plane strain will also be compared by plotting the shear components ϵ_{21} and ϵ_{31} respectively. These are the strain components simulated in Chapter 4.

Figures. 5.5, 5.6, and 5.7 show the VDCOM, WBV and shear strain plots for Sample A, B and C respectively. In b) of each of these figures is the VDCOM with TDs marked as either pure edge (circles) or screw component (squares). It is clear from the shear strain and WBV plots that the TDs identified as screw component are the only ones to show contrast in the out-of-plane maps. This is consistent with predictions made in Section 5.2.4, which were backed up by the simulations produced in Chapter 4. Consequently, those that do not appear in the out-of-plane maps but show contrast in the in-plane maps are edge TDs. Doing this for all datasets for each sample gives a representative picture of the ratio of edge and screw component TD across the samples. These are shown in Table 5.1 where the TD densities are also

given. The calculated relative amounts of edge and screw component TDs is in fairly good agreement with the predictions made based on the misorientation histograms. Sample A has the highest TD density and also the highest proportion of edge TDs. Sample B also has a relatively high number of edge TDs as was indicated by the misorientation histogram having a significantly wider misorientation around z. It is important to remember that mixed TDs will contribute to the misorientation around z due to the edge component of the Burgers vector and also the surface relaxation of the screw component. Similarly, pure screw TDs will contribute surface relaxation-driven misorientation around z. Despite this, as the relative number of edge TDs decreases, the magnitudes of the in-plane and out-of-plane rotation will begin to converge as the surface relaxation and infinite medium effects from screw TDs are similar. This effect is observed in Sample C where there is a significant decrease in the proportion of edge TDs and as such there is a smaller difference between in-plane and out-of-plane misorientation across the sample (Figure. 5.4c)). A decrease in edge TDs is again in good agreement with predictions made previously based on the misorientation histograms. Despite this, with approximately 31% edge TDs still present, it is not expected that the out-of-plane and in-plane histograms would converge so quickly. However, samples B and C were intentionally doped while sample A was not. It is possible, then, that the dopants have some effect on the misorientation, which could be distorting the histograms in Sample C. This effect is currently under consideration, and comparisons between highly doped and nominally doped samples are being made. The sudden decrease in pure edge TDs in sample C could be a consequence of the slower coalescence used in Sample C which is known to cause edge TDs to bend and annihilate with one another near coalescence boundaries. This could also potentially explain the convergence of the histograms for sample C. It could be the case that there are inclined edge TDs present, leading to more out-of-plane misorientation or even non-threading TDs that are bent below the surface. This is also currently under consideration.

Examining the shear strain plots (derived using the pattern-matching approach discussed in Chapter 2 Section 2.3.5 *Deriving Strain from EBSPs*), it is also clear that only one lobe of the strain profile is visible for each TD in ϵ_{zx}. This is consistent with

Sample	TDD (cm^{-2})	Edge TDs	Approximate Edge TDD (cm^{-2})
A	8.1×10^8	40% ±5%	3.24×10^8
B	5×10^8	39% ±5%	1.95×10^8
C	1.8×10^8	31% ±5%	0.56×10^8

Table 5.1: Threading dislocation densities and relative amounts of pure edge TDs for samples A, B and C- as calculated from EBSD measurements.

the prediction stemming from the simulations in Chapter 4 which incorporated the effects of sample tilt and interaction volume elongation. Moreover, the contrast in the ϵ_{yx} map is more diffuse and does not exhibit the sharp peaks where TDs occur like ϵ_{zx}. This is also consistent with the perturbed simulations in Chapter 4. This would indicate that improvements in spatial resolution, which would reduce the interaction volume size, may produce strain maps with more detailed strain profiles for TDs. If the interaction volume could be reduced adequately such that the effects of the sample-tilt-induced elongation are minimised, then the dipole/quadrupole structure should be visible. There is already evidence that this would be the case from TKD measurements where the approximate spatial resolution is 10 nm [42]. This improvement in spatial resolution could be achieved from using much lower beam energies (≤ 5 kV) which could be facilitated by using direct electron detectors with much higher energy resolution and quantum detective efficiencies than typical CCD/CMOS-phosphor detectors. By achieving such a spatial resolution, pure screw and mixed TDs could be distinguished by comparing the measured strain profiles with simulations such as those in Chapter 4.

5.6 Summary

This chapter combines the ability to image TD distributions (VDCOM) with misorientation and strain mapping that has sufficiently high resolution to resolve the effects associated with individual TDs. It has been shown that this reveals important details about the subgrain structure across three differently grown GaN thin films. Additionally, by comparing in-plane and out-of-plane components of shear strain and curvature (via the WBV approach), TDs in each of the samples can be identified as being edge

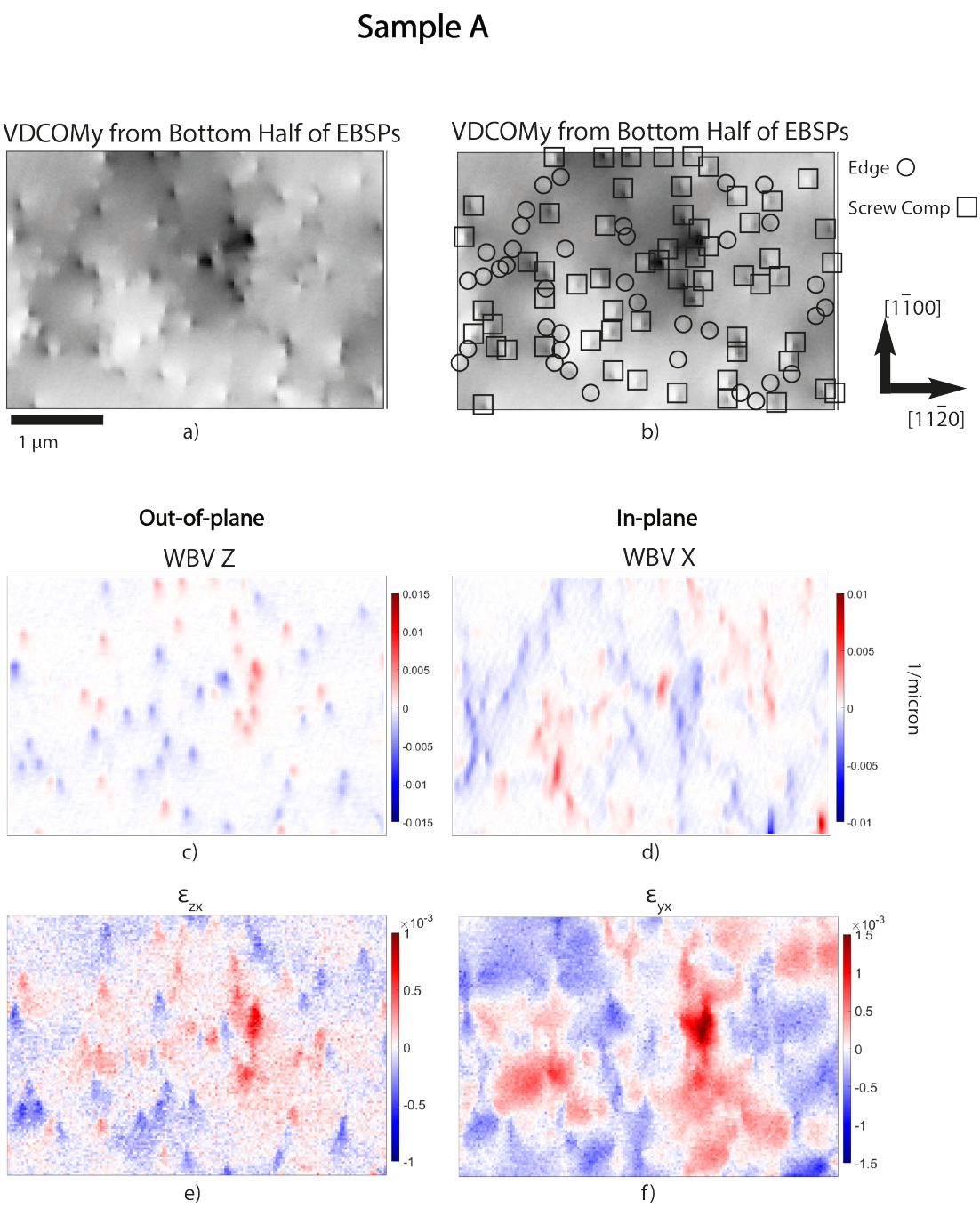

Figure 5.5: a) Virtual diode centre of mass (VDCOMy) image of TDs in Sample A. b) Shows the same VDCOMy image with pure edge TDs marked with a circle and screw component TDs marked with a square. Weighted Burgers vector (WBV) maps of the c) out-of-plane and d) in-plane components, respectively. WBV were plotted with 3x3 square loops. Pure edge TDs will only appear in d) while screw component TDs will appear in both. Relative shear strain components e) ϵ_{zx} and f) ϵ_{yx}. The screw components show strongly in e). The strain is calculated relative to a simulated reference pattern and subsequently normalised via subtraction of the mean value in each image.

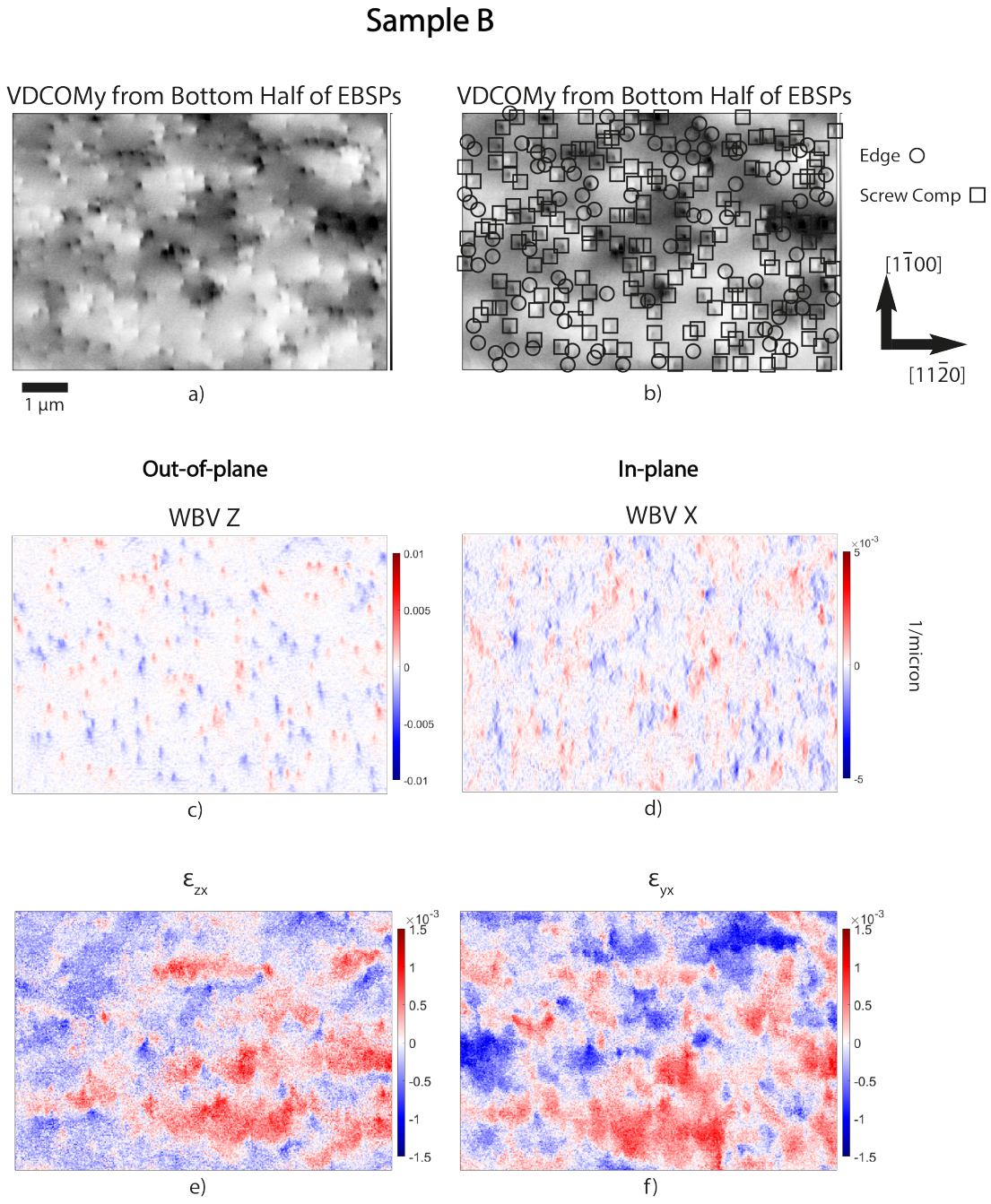

Figure 5.6: a) Virtual diode centre of mass (VDCOMy) image of TDs in Sample B. b) Shows the same VDCOMy image with pure edge TDs marked with a circle and screw component TDs marked with a square. Weighted Burgers vector (WBV) maps of the c) out-of-plane and d) in-plane components, respectively. WBV were plotted with 3x3 square loops. Pure edge TDs will only appear in d) while screw component TDs will appear in both. Relative shear strain components e) ϵ_{zx} and f) ϵ_{yx}. The screw components show strongly in e). The strain is calculated relative to a simulated reference pattern and subsequently normalised via subtraction of the mean value in each image.

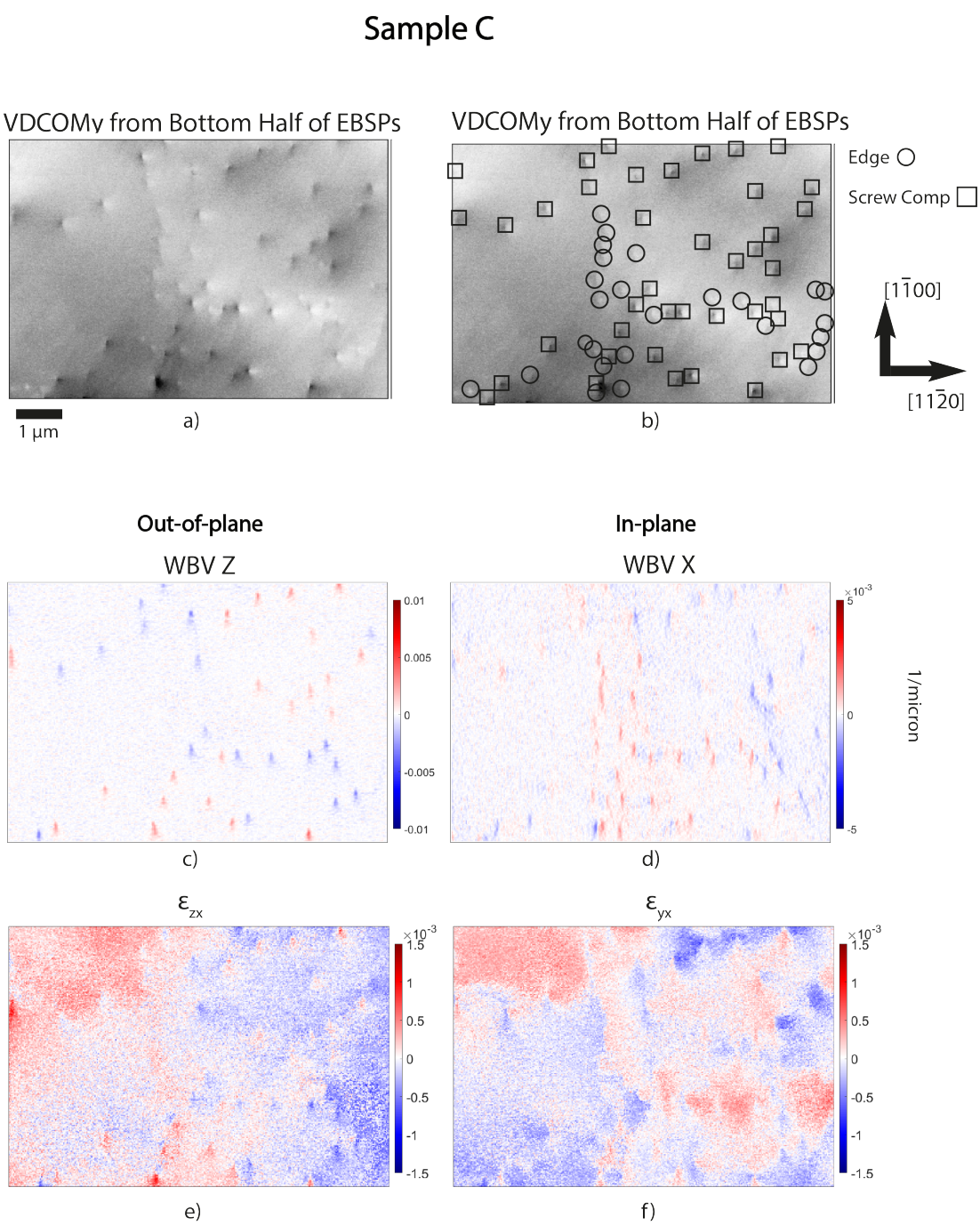

Figure 5.7: a) Virtual diode centre of mass (VDCOMy) image of TDs in Sample B. b) Shows the same VDCOMy image with pure edge TDs marked with a circle and screw component TDs marked with a square. Weighted Burgers vector (WBV) maps of the c) out-of-plane and d) in-plane components, respectively. WBV were plotted with 3x3 square loops. Pure edge TDs will only appear in d) while screw component TDs will appear in both. Relative shear strain components e) ϵ_{zx} and f) ϵ_{yx}. The screw components show strongly in e). The strain is calculated relative to a simulated reference pattern and subsequently normalised via subtraction of the mean value in each image.

or screw component (screw or mixed). While the screw component of the Burgers vector has significant surface relaxation affecting the in-plane strain and misorientation components as well as the out-of-plane, the surface relaxation associated with the edge TDs in the out-of-plane components is minimal, as shown in the simulations in Chapter 4. This means any TDs appearing in in-plane shear strain and WBV components but not in the out-of-plane are pure edge TDs. All other TDs must then be pure screw or mixed TDs. For the epitaxial growth of *c*-oriented GaN there tends to be very few pure screw TDs [126] and so it is assumed that most of the 'screw component' TDs are in fact mixed. With further improvements in spatial resolution, which could be facilitated by low beam energy ($\leq$ 5 keV) measurements, it will become possible to distinguish directly between mixed and screw TDs. This is because the interaction volume will be reduced, reducing the effect of the interaction volume elongation and allowing the strain profiles to be better resolved. Then, rather than seeing single lobes, the strain profiles should show their full dipole/quadrupole nature which can then be compared with simulations such as those in Chapter 4. However, even in its current state, the ability to map strain with such a high spatial resolution and minimal sample preparation, using EBSD, means local strain distributions can be investigated very quickly. This will prove to be extremely useful for GaN-based device development where strain-associated effects such as local piezoelectric polarisation play an enormous role in affecting device performance, becoming even more important as device diameters are reduced.

Chapter 6

Using Radon Transformations to Image Threading Dislocations Affecting Individual Lattice Planes

6.1 Introduction

The goal of this chapter is to develop an EBSD image processing technique that allows images to be acquired for specific diffraction conditions, similar to methods in transmission electron microscopy (TEM). In TEM, electron transparent samples are used such that the high energy electron beam is able to pass through the sample, with some electrons diffracting from crystal planes on their way through. These diffracted electrons contribute to the *diffracted beam* while the unaffected transmitted beam electrons contribute to the *direct beam* [91]. As the two beams impinge on a detector placed below the sample, an image, known as a diffraction spot pattern, is collected with a large central bright spot corresponding to the direct beam, and diffraction spots of constructive interference off-axis surrounding this (Figure. 6.1).

As the Bragg diffraction in TEM is dictated by the angle of incidence between beam and the sample crystal planes, it is possible to tilt the sample such that only

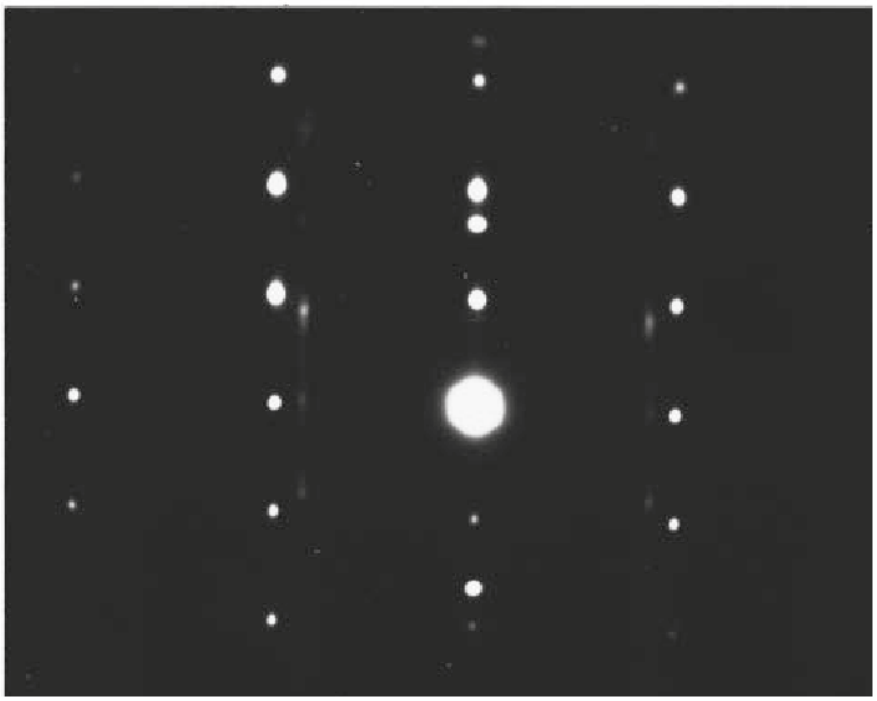

Figure 6.1: Cross-sectional diffraction pattern from a 22.5 nm GaN buffer layer, obtained in the transmission electron microscope (TEM). The large central bright spot corresponds to the direct beam with diffraction spots of constructive interference off-axis surrounding this. Figure adapted from [157].

one Bragg condition (diffraction condition) is satisfied by the incident beam. This is known as a 'two-beam' condition [91]. By then monitoring the intensity distribution of the diffracted beam, an image of TDs in the sample can then be acquired (known as dark-field imaging). These TDs will be ones whose Burgers vector or strain field distorts the diffracting plane [158]. Consequently, some TDs may not be visible for a given diffraction condition. The condition for dislocations to be invisible with a certain diffraction condition (described by the diffraction vector $\mathbf{g}$) is known as the 'invisibility criterion'. For screw dislocations this is simply given as [159, 160]:

$$\mathbf{g} \cdot \mathbf{b} = 0 \tag{6.1}$$

Where $\mathbf{b}$ is the Burgers vector of the dislocation. However, this is slightly more complicated for edge dislocations where the strain field is normal to the slip plane for edge dislocations. Consequently, edge dislocations are only completely invisible in a dark-field image if the condition in Eq. 6.1 and [159, 160]:

$$\mathbf{g} \cdot \mathbf{b} \times \mathbf{u} = 0 \tag{6.2}$$

are satisfied, where $\mathbf{u}$ is a unit vector along the dislocation line direction. Nonetheless, it is entirely possible, using TEM, to view which TDs affect which crystal planes and then to use this information to infer the possible Burgers vector of the TD [160]. This is also the basis for electron channelling contrast imaging (ECCI) analysis in the SEM. As ECCI images exhibit contrast based on the modulation of diffraction of the beam electrons through the sample (i.e. the immediate diffraction of beam electrons incident on crystal planes close to a Bragg angle which are then not backscattered), by taking images at various incoming diffraction conditions, it is possible to determine which TDs affect which planes [14, 122, 123, 126]. However in EBSD, this is not the case. Diffracted BSEs diffract from a multitude of different crystal planes on their way out of the sample, resulting in the many different Kikuchi bands visible in an EBSP. As such, the measured distortion that results from the strain and misorientation associated with TDs is a net distortion with contributions from all crystal planes in an

EBSP. It would however be very useful to see exactly which planes are affected by which TDs. This could give further insight into the Burgers vectors of any measured TDs and would effectively give EBSD users the ability to image TDs in much the same way as in the TEM and in the SEM for ECCI, while having the advantage of greater statistics than TEM and only one dataset with available strain and misorientation information compared to many datasets without this quantitative information when using ECCI. While it is theoretically feasible to do this in EBSD by monitoring the shift of individual Kikuchi bands, it can be extremely challenging due to the low signal in the Kikuchi bands relative to the rest of an EBSP. This chapter outlines a method for this using a Radon transformation approach to first map Kikuchi bands to points in Radon space, and then monitor the change in their intensity distribution via their centre of mass (much like VDCOM). By doing this for individual bands in every EBSP in a dataset, threading dislocations contributing to the distortion of the selected bands can be mapped. However, in normal plan-view EBSD surface relaxation plays a significant role, as demonstrated in the previous two chapters and discussed in [161, 162]. As such, the measurement is again limited to being able to distinguish edge-type TDs and screw-component TDs from one another. However, cross-sectional EBSD measurements could overcome this limitation as surface relaxation is no longer an issue (much like in TEM). Consequently, this chapter provides a proof-of-concept for being able to image TDs with EBSD by choosing individual planes that they might affect.

6.2 Materials

The first sample, named Sample A in this chapter is Sample C from Chapter 5. It is a GaN thin film grown on a sapphire substrate via a 2D-3D growth method similar to the one outlined in [70]. The second sample, Sample B, is the same N-polar GaN sample discussed in Chapter 3. It is a 900 nm thick N-polar GaN thin film grown by metal-organic vapor-phase epitaxy (MOVPE) on a sapphire substrate. The exact growth details for Sample B can be found in Section 3.2 of Chapter 3.

6.3 Radon Transform Imaging in EBSD

This section will briefly outline what a Radon transform is and then show its applicability for detecting Kikuchi bands. A method for imaging based on the Radon transform information using COM imaging is then explained.

6.3.1 Radon Transform of EBSPs

The Radon transform is directly related to the Hough transform, introduced earlier in this thesis, in that it is a mapping from an image space to a parameter space. This simply means each point in the 'true' image is mapped to a different image via user defined parameterisation. Like the Hough transform, the parameter space for the Radon transform is also parameterised by (ρ, θ), where ρ is the distance from the origin to a straight line in the image passing through a point (x_i, y_i) and θ is the angle of the straight line normal. They are related by $\rho = x_i cos\theta + y_i sin\theta$. And so in much the same way as in the Hough transform, lines of intensity in the image are mapped to points of intensity in Radon space. The main general difference, however, is that the Hough transform was designed with the intention of detecting straight lines in binary images based on a discrete vote-counting method [109]. This means when mapping via the voting method, every line intersecting a point is given the same intensity in Hough space, with the accumulated intensities showing as a bright point in the Hough space image (sinogram). The speed of this process is what has historically kept the Hough transform dominant in the EBSD space. The Radon transform, on the other hand, is a more general mathematically solid formula for the continuous mapping of an object in image space to parameter space via integration [109]. Although this makes it more computationally expensive than the Hough transform, it can be more accurate and can map the integrated intensities from each pixel of the line passing through a given point to Radon space. This is particularly useful for measuring any small changes in the intensity distribution of Kikuchi bands as the intensities are preserved in Radon space. While not commercially common practice in EBSD, the Radon transform has had increased use for the localisation of Kikuchi bands in recent EBSD indexing

applications [118, 163–166], while spherical Radon transformations have been used to approximate for the true parabolic nature of Kikcuhi bands in dynamical simulations [167].

In this chapter, for the parameterization of the Radon transform, pairs of lines forming Kikuchi bands were assumed to be straight parallel lines. This is justified by the small solid angle covered by the detector, such that the parabolic nature of the bands is not captured, giving a negligible divergence of the band edges. It is also important to note that the removal of the diffuse background from the EBSP before performing the Radon transform is absolutely paramount. This removes the signal from which VDCOM images in Chapter 3 are mostly formed and isolates the EBSP to the signal from diffraction-out processes only. This means that the processed EBSP contains only the signal from the Kikuchi bands and nothing else. This background removal can be done using a Fast Fourier Transform (effectively a high-pass filter). This converts the signal the patterns to Fourier space, which then allows the short wavelength components (Kikuchi lines) to be separated from the slow changing, low-frequency component (the diffuse background). An inverse transform back to real space then produces the desired image of the Kikuchi bands. Additionally, due to the nature of the BSE intensity distribution, EBSPs suffer from a reduction in intensity near the edges of the pattern. This was corrected for using a basic contrast limited histogram equalisation (CLAHE) algorithm, making Kikuchi bands near the edges of the image easier to detect in Radon space. Figure 6.2 shows a) a processed EBSP pattern for GaN and b) the corresponding Radon space image (known as a sinogram). From this figure, it can be seen that the Kikuchi bands appear not as point-like structures in the sinogram but as 'butterflies' with a top lobe, middle lobe, and bottom lobe. This is due to the smearing out of the non-zero width of the intensity of the Kikuchi bands, with the middle lobe corresponding to the intensity running through the middle of the band. Higher-order Kikuchi bands will have less intensity in the EBSP, and so appear as dimmer butterflies in the sinogram. Additionally, some butterflies may show asymmetry in their intensity. This is related to excess-deficiency effects found in EBSPs, where one band edge has greater intensity than the other due to the anisotropic scattering of

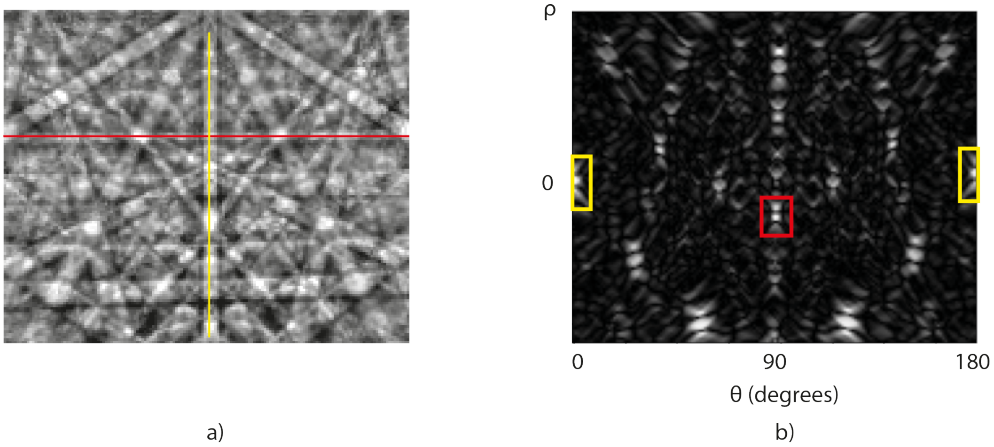

Figure 6.2: a) An EBSP with the diffuse background subtracted via a Fast Fourier Transform, leaving only the signal from the Kikuchi bands. b) The sinogram (Radon space image) of a) once a Radon transform has been applied, mapping the Kikuchi bands in real space to points/butterflies in Radon space. The yellow band marked in a) corresponds to the signal contained in the yellow boxes in b) and likewise for the red band. See Figure 2.19 for a comparison with a Hough transform sinogram.

beam electrons before diffraction which is related to the geometry of EBSD. A complete explanation of this effect can be found in [168]. For the purpose of this chapter it is simply important to know that this asymmetry exists, such that when it comes to interpreting the sinograms it is easy to understand that the butterfly intensity is not constant. The only exception in the mapping of bands to Radon space is if there is a central vertical band. As the (0,0) of the parameterisation is in the middle of this band, the left half will be mapped to $\theta = 0$ and the right half will be mapped to $\theta = 180$. This is not an issue for the processing performed in this chapter, as the signal is still entirely within the sinogram, the two halves just have to be summed together. Figure 6.2 shows this triviality with the central band, $(11\bar{2}0)$, marked by a yellow line in a) is transformed into the butterflies contained in the yellow boxes in b). As a comparison, another band, $(1\bar{1}01)$, is marked in with a red line in a) and is transformed into a singular butterfly in b), contained in the red box.

The code used to perform the Radon transformation was written in Python. The computational time for the transformation of an EBSP to Radon space depends on many factors. While hardware is arguably one of the most important, it is also the most

variable from institution to institution. Additionally, with hardware evolving rapidly from year to year, a lengthy discussion on it here will probably not stay particularly relevant for long. The most important bit of hardware that the user can have, however, for performing a Radon transform is a dedicated graphics processing unit (GPU). This allows the user to run the Radon transform on the GPU, via a parallel computing platform such as CUDA, rather than on the central processing unit (CPU). This was done for the work in this thesis using the ASTRA toolbox (originally developed for tomography applications) [169, 170], improving computational times by a factor of six when compared to the previous code, which was based on the CPU-run Python Scikit Radon transform.

Another factor that has a significant impact on the computational time is image resolution. The higher the resolution for EBSPs, the longer the Radon Transform takes. Consequently, binning the patterns before the Radon transform can significantly speed the process up. However, as binning reduces the resolution, it also reduces the capacity for any slight changes in the intensity distribution of Kikuchi bands to be detected. As a result, there is a binning threshold at which major information could be lost. This will vary for different materials and even for different samples. The greater the distortion of Kikuchi bands from misorientation and strain, the greater the binning can be without loss of information.

6.3.2 Radon Centre of Mass Imaging (RCOM) in EBSD

Once Kikuchi bands have been mapped to Radon space, the changes in their position on the EBSP due to the strain and misorientation associated with TDs can be tracked by monitoring the centre of mass of their butterflies in Radon space across the entire dataset. This can be achieved by monitoring the entire butterfly, but more easily by simply tracking the centre lobe corresponding to the bulk intensity of a band. For example, to monitor the changes in the Kikuchi band corresponding to $(11\bar{2}0)$, a square boundary can be placed around the middle lobe of the butterfly corresponding to the $(11\bar{2}0)$ band for the first EBSP in the dataset. The centre of mass/intensity within this boundary can be calculated using Eq. 3.1 from Chapter 3. This is then repeated

for every other EBSP in the dataset, where the square boundary remains at the same fixed position for all of them. By plotting the change in the COM from pattern to pattern, a map can be plotted where the contrast depends on changes in the position of the Kikuchi band edge. This is because any crystallographic change causing the measured plane (Kikuchi band) to move, will also cause the intensity distribution of the middle lobe of the butterfly in Radon space to move, giving a change in intensity/COM value. Theoretically, there should be the highest contrast at TDs affecting the $(11\bar{2}0)$ plane, with the exception of surface relaxation effects for plan-view EBSD. This can be repeated for other Kikuchi bands, resulting in an imaging technique that can isolate TDs that affect particular bands by selecting different diffraction conditions, similar to TEM.

6.4 Invisibility Criteria for Threading Dislocations in GaN

To be able to make use of the Radon centre of mass (RCOM) technique for GaN, the invisibility criteria for edge, screw and mixed TDs must be understood. As the measurements in this thesis were taken in plan-view, however, the RCOM images will always exhibit contrast around screw-component TDs due to the strong in-plane surface relaxation effects associated with screw-component TDs. These effects mean that no invisibility criteria can be achieved in plan-view for screw component TDs, even when $\mathbf{g} \cdot \mathbf{b} = 0$. Therefore, the question is more simply, at what diffraction condition (specific Kikuchi band) will edge TDs have minimal or no contrast (i.e. be invisible). For the edge Burgers vector most commonly found in GaN, $1/3 < 11\bar{2}0 >$, the diffraction vector ($\mathbf{g}$) must then satisfy Eqs. 6.1 and 6.2. For the case of threading dislocations in c-oriented GaN, $\mathbf{u} = [0001]$. This gives 3 unique Burgers vectors for edge TDs for the purpose of the invisibility criterion, as the 6 symmetrically equivalent vectors are really 3 pairs of Burgers vectors where the pairs have the same indices but one of the pair is simply the negative of the other (which has no bearing on the invisibility criterion). This is illustrated in Fig. 6.3.

An obvious candidate for fulfilling Eqs. 6.1 and 6.2 would be to pick a diffraction condition of $\mathbf{g} = (0002)$. This would make all edge TDs invisible. However, this is

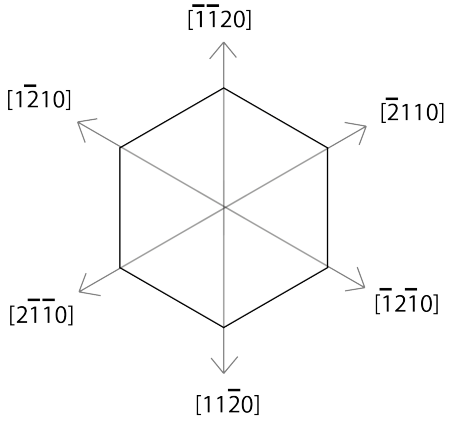

Figure 6.3: The possible Burgers vector directions for edge TD in wurtzite GaN.

not possible for the plan-view geometry. Consequently, the next best option is to pick a diffraction condition perpendicular to a $[11\bar{2}0]$ band. This satisfies Eq. 6.1 but not Eq. 6.2 for those TDs with exactly the Burgers vector $\mathbf{b} = 1/3[11\bar{2}0]$. By reducing Eq. 6.1 to zero, however, there is a contrast minimum, and if this is sufficiently small, an 'effective invisibility' is achieved [171]. This occurs because the remaining intensity from Eq. 6.2 is below the noise level of the measurement.

Assuming the Burgers vector is exactly $\mathbf{b} = 1/3[11\bar{2}0]$, using the RCOM technique this can be accomplished by sampling the diffraction vector $\mathbf{g} = (1\bar{1}01)$. To then maximise the contrast for edge TDs with a Burgers vector $1/3[11\bar{2}0]$, the $(11\bar{2}0)$ band can be selected for RCOM analysis as this corresponds to the diffraction vector $\mathbf{g} = (11\bar{2}0)$. In a cross-sectional measurement, where surface relaxation would play no role, this would also turn off the pure screw TDs as $[11\bar{2}0] \cdot [0001] = 0$. However, the surface relaxation due to the screw TDs means they maintain strong contrast. Mixed TDs can never be completely turned off due to having both a screw and an edge component.

6.5 Results

The RCOM method outlined in the previous section was used for two different GaN thin-films. The datasets for both were taken with a 20 kV beam and a step size of 25 nm. Due to the symmetry of the crystal, it is impossible to determine from an EBSP which band belongs to an *exact* plane, only that it belongs to a family of symmetrically

$\mathbf{g}$	$\mathbf{g}\cdot\mathbf{b}$	$\mathbf{g}\cdot\mathbf{b}\times\mathbf{u}$
$(11\bar{2}0)$	$\neq 0$	$\neq 0$
$(1\bar{1}01)$	$= 0$	$\neq 0$
$(10\bar{1}1)$	$\neq 0$	$\neq 0$

Table 6.1: Here the invisibility criteria is tested for edge TDs with a Burgers vector of $1/3[11\bar{2}0]$ against three different diffraction conditions. Edge TDs with this Burgers vector should only have an effective invisibility for the diffraction condition $(1\bar{1}01)$ and should be visible for both other conditions.

equivalent planes. This means that for the $11\bar{2}0$ planes for example, it becomes arbitrary to label a particular corresponding band with exact indices such as $(1\bar{2}10)$ etc. For the purpose of interrogating invisibility criteria the central band in the EBSPs used in this chapter, highlighted in yellow in Figure. 6.2, will be assumed to correspond to the $(11\bar{2}0)$ plane. Figure. 6.4 and Figure. 6.5 show then the results of the RCOMy analysis on samples A and B for the diffraction vector $\mathbf{g} = (11\bar{2}0)$, the perpendicular diffraction vector $\mathbf{g} = (1\bar{1}01)$ and a symmetrically equivalent diffraction vector $\mathbf{g} = (10\bar{1}1)$ which is not perpendicular to $\mathbf{g} = (11\bar{2}0)$. Figures 6.6 and 6.7 show the corresponding TD identification using the weighted Burgers vector method introduced in Chapter 5. It can be seen that the TDs identified as pure edge in Figures 6.6 and 6.7 only show with the diffraction vectors $\mathbf{g} = (11\bar{2}0)$ and $\mathbf{g} = (10\bar{1}1)$ but remain invisible for the diffraction vector $\mathbf{g} = (1\bar{1}01)$ in both samples, as expected for edge TDs with Burgers vectors $1/3[11\bar{2}0]$ (i.e. the diffraction contrast is minimised for the edge TDs as $\mathbf{g}\cdot\mathbf{b} = 0$). This suggests that the pure edge TDs appearing in the imaged regions of both samples have exactly that Burgers vector and not some other, symmetrically equivalent Burgers vector. A summary of the invisibility criteria for an edge TD with Burgers vector $1/3[11\bar{2}0]$ for the different diffraction conditions imaged is found in Table 6.1.

What is also noticeable in Figures. 6.4 and Figures. 6.5 is the difference in the signal produced by monitoring the different diffraction conditions for the two samples. The TDs appearing in the images produced with the diffraction vector $\mathbf{g} = (11\bar{2}0)$ have noticeably lower contrast than those produced by $\mathbf{g} = (10\bar{1}1)$ and $\mathbf{g} = (10\bar{1}1)$. This is because the latter two diffraction conditions contain the effects from both the surface relaxation and the Burgers vector of the screw component TDs. This is a significantly

greater effect than just the screw surface relaxation and edge surface relaxation/Burgers vector in the $\mathbf{g} = (11\bar{2}0)$ diffraction condition. This is most easily visualised by looking at the strain profiles of screw, edge and mixed TDs for in-plane and out-of-plane in Chapter 4.

When comparing the RCOM method with other crystallographic analysis methods used in this thesis, such as the WBV method, it is clear the signal is noisier in RCOM images. This is because the WBV method measures the net curvature/distortion in the crystal from multiple planes/Kikuchi bands in each EBSP, whereas the RCOM extracts its contrast from the distortion of only one plane/band. Consequently, the WBV method measures larger distortions, meaning the SNR is much improved compared to RCOM. WBV however does not have the flexibility to measure distortion from only one plane.

Further work is ongoing to utilise this technique across a range of samples with larger areas, containing more than one type of edge TD Burgers vector.

6.6 Summary

In this chapter, a new EBSD-based methodology has been developed, which produces images of TDs for different diffraction conditions, which can be chosen by the user. This has been achieved by performing a Radon transform on each EBSP in an EBSD dataset, allowing the intensities of each Kikuchi band to be mapped to points in Radon space where the change in the position of the intensity for each point (band) can be monitored using the COM approach introduced in Chapter 3. This produces an image where any crystallographic distortion (strain/misorientation) that affects a particular crystal plane produces contrast. This results in an image where any TDs affecting that particular plane are visible, and those not affecting the plane are invisible. By doing this and utilising the invisibility criterion, it is possible to identify which TDs are edge and screw-component, like in Chapter 4, but also directly identify the exact Burgers vector for the edge TDs present in a given sample by testing for which diffraction conditions an effective invisibility criterion occurs. It may be the case however that, due to the

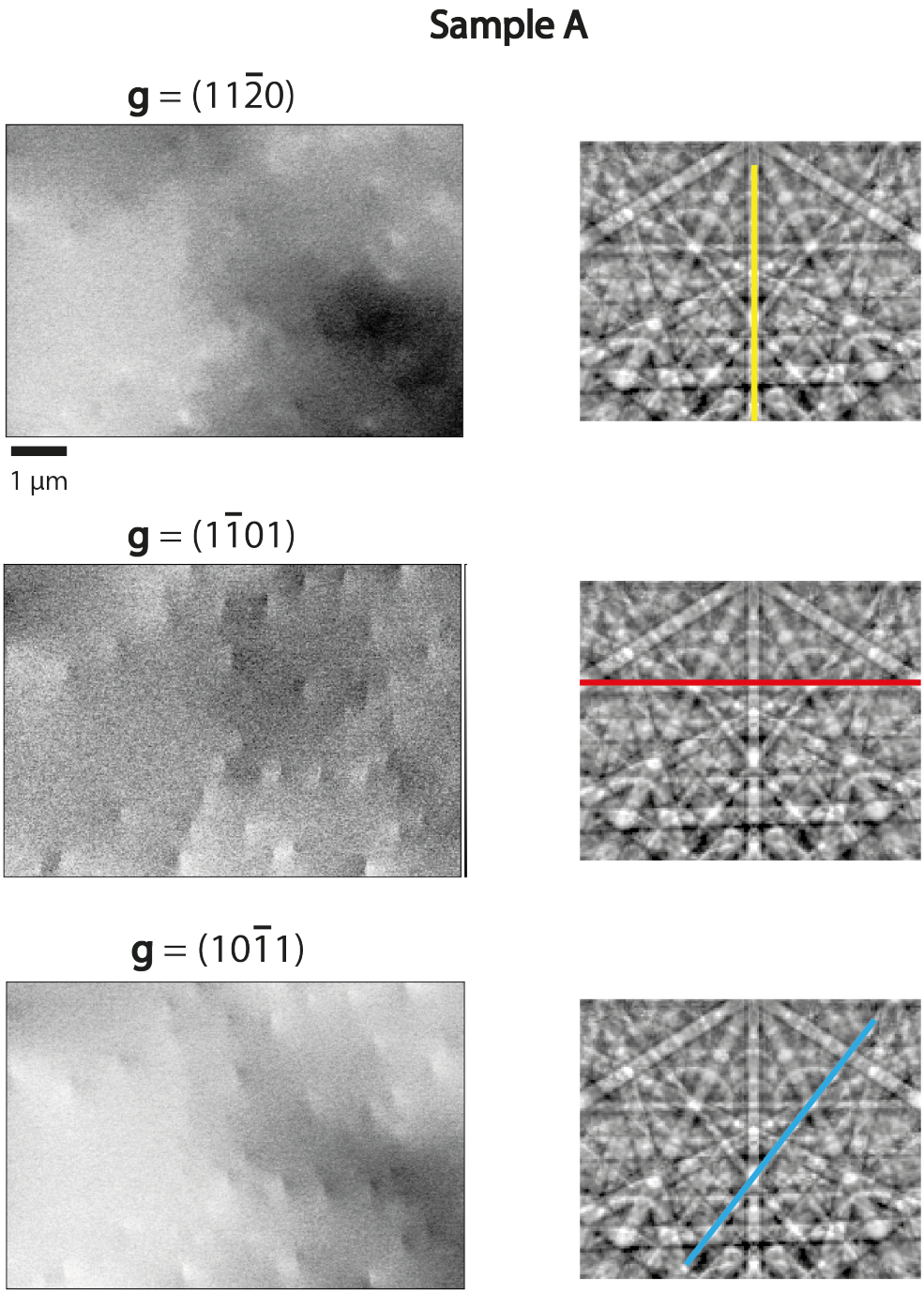

Figure 6.4: RCOMy images of Sample B alongside EBSP with corresponding diffraction condition marked. Image taken with diffraction vector $\mathbf{g} = (11\bar{2}0)$ shows all TDs due to the combination of in-plane Burgers vector effects from the edge TDs and surface relaxation from the screw component TDs. Images taken with diffraction vector $\mathbf{g} = (1\bar{1}01)$ satisfy the invisibility criterion for pure edge TDs with Burgers vectors $1/3[11\bar{2}0]$. The edge TDs show no contrast in these images and only screw component TD are visible. All TDs are again visible for $\mathbf{g} = (10\bar{1}1)$ with no invisibility condition satisfied, indicating all edge are $\mathbf{b} = 1/3[11\bar{2}0]$.

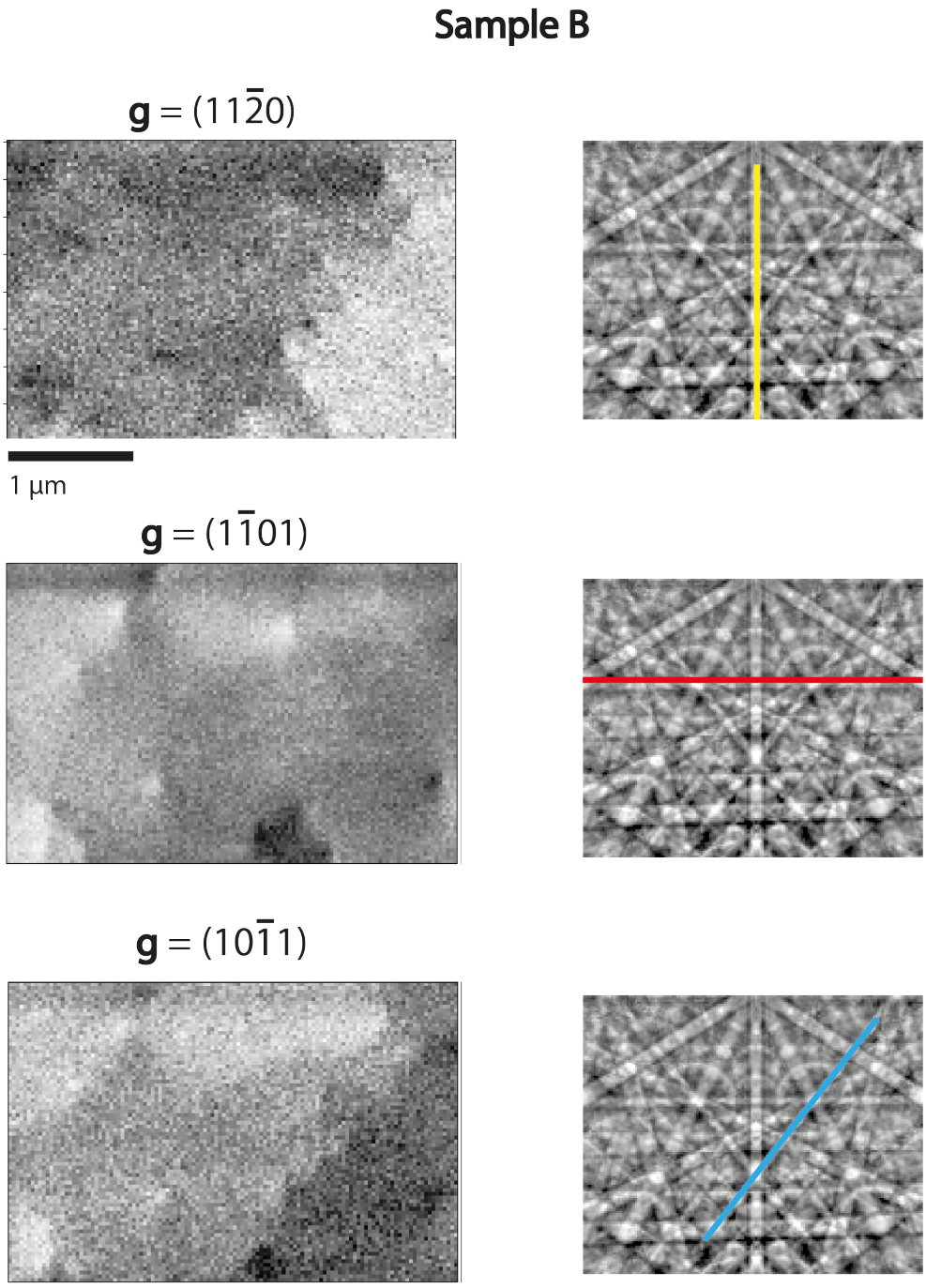

Figure 6.5: RCOMy images of Sample B alongside EBSP with corresponding diffraction condition marked. Image taken with diffraction vector $\mathbf{g} = (11\bar{2}0)$ shows all TDs due to the combination of in-plane Burgers vector effects from the edge TDs and surface relaxation from the screw component TDs. Images taken with diffraction vector $\mathbf{g} = (1\bar{1}01)$ satisfy the invisibility criterion for pure edge TDs with Burgers vectors $1/3[11\bar{2}0]$. The edge TDs show no contrast in these images and only screw component TD are visible. All TDs are again visible for $\mathbf{g} = (10\bar{1}1)$ with no invisibility condition satisfied, indicating all edge are $\mathbf{b} = 1/3[11\bar{2}0]$.

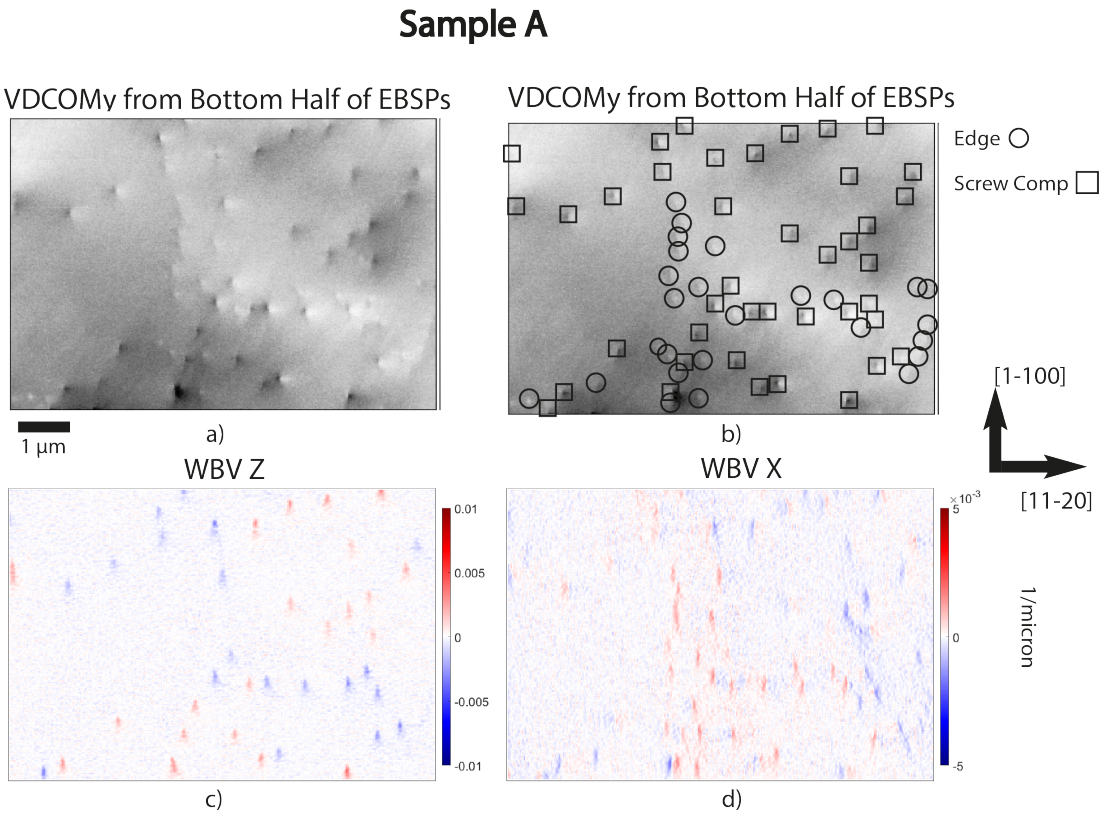

Figure 6.6: a) VDCOMy image of Sample A generated from the bottom half of the EBSPs in the dataset. b) The same VDCOMy image but with screw component TDs marked with squares and edge component TDs marked with circles. The edge TDs have been identified by observing which TDs show strong in-plane curvature in the weighted Burgers vector X map (d) and no curvature in the out-of-plane weighted Burgers vector Z map (c). Screw component TDs show strongly in both.

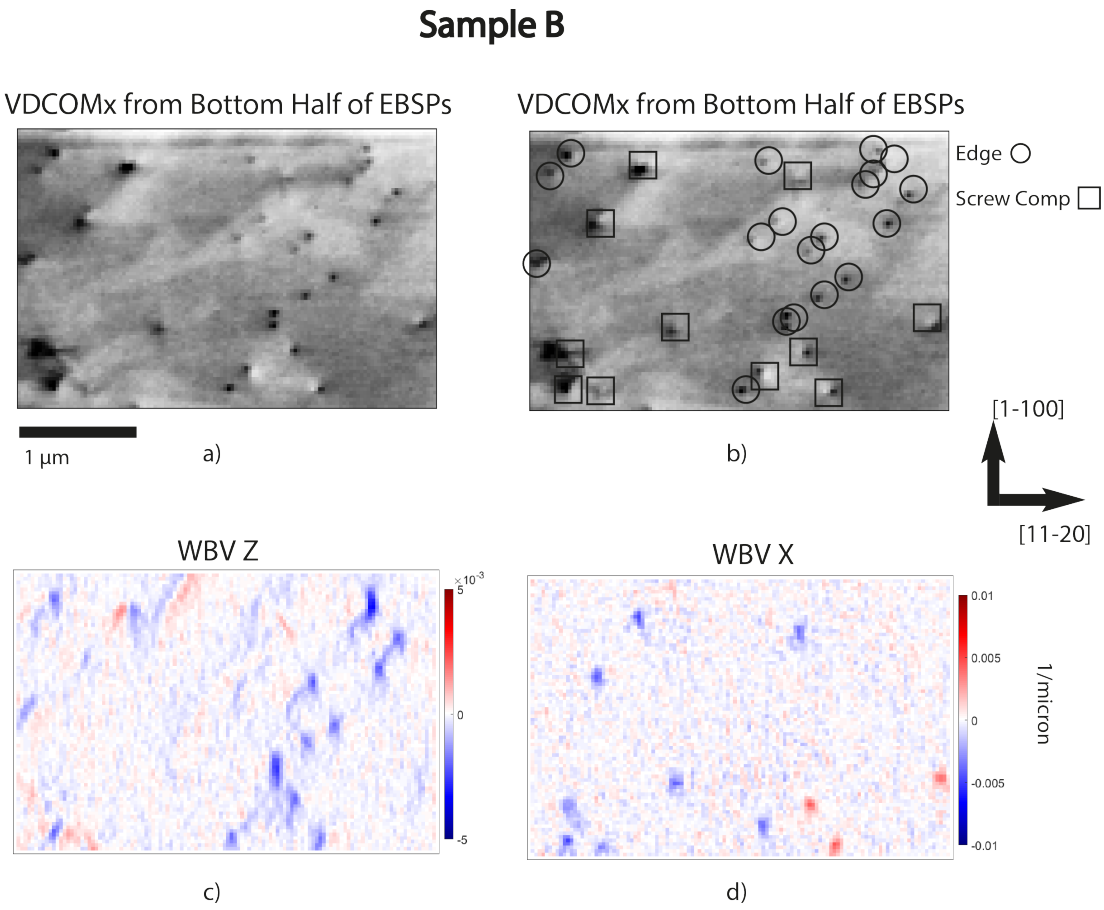

Figure 6.7: a) VDCOMx image of Sample B generated from the bottom half of the EBSPs in the dataset. b) The same VDCOMx image but with screw component TDs marked with squares and edge component TDs marked with circles. The edge TDs have been identified by observing which TDs show strong in-plane curvature in the weighted Burgers vector X map (d) and no curvature in the out-of-plane weighted Burgers vector Z map (c). Screw component TDs show strongly in both.

limited solid angle of the Kikuchi sphere covered by the detector, a band corresponding to an invisibility condition may be out of frame. If this is the case, the sample could be rotated and the EBSD dataset taken again to access the necessary bands, or the detector can be moved closer to the sample, such that a larger solid angle is covered (see Figure 2.18 for a brief discussion on typical solid angles). Due to the effects of surface relaxation, this technique is not able to utilise the invisibility criterion for screw and mixed TD identification when in plan-view. However, if cross-sectioned samples were used then the RCOM technique introduced here would allow the EBSD user to perform TD identification much like that in transmission electron microscopy, where all TDs can be identified. This technique has been demonstrated across two differently grown GaN thin-films, showing its consistency as a technique for different samples.

Chapter 7

Conclusions and Future Work

This thesis describes the analysis of threading dislocations in GaN using electron backscatter diffraction. This involves characterising their densities, their associated misorientation and strain, and also their type. In developing the EBSD technique to be able to obtain all of this, it has become a particularly strong technique with high statistics, short acquisition and analysis times, minimal sample preparation and a low skill barrier for the analysis of TDs in GaN, with the capability of extending to other materials. The main developments from this thesis will now be summarised with suggestions of how future work may improve the capabilities of EBSD even further.

Chapter 3 was centred around developing a post-acquisition imaging processing technique which could be applied to EBSD datasets that would provide high signal-to-noise images of TD distributions while having the flexibility to produce topographically dominated images of the same area simultaneously. This was achieved via the virtual diode centre of mass (VDCOM) imaging technique. As an EBSD detector is pixelated, it is possible to measure not only the scalar change in intensity as the electron beam is scanned across a sample, but also how the centre of the intensity distribution changes between EBSPs recorded at each dwell point in the scan. It had already been shown in previous research that this is an effective way of imaging with crystallographic contrast, as any crystallographic distortion in the sample results in a change in the distribution of backscattered electrons- giving contrast at TDs. The work in this thesis then combined this with virtual diode imaging. This is the post-acquisition segmentation of the EBSD

detector, meaning the COM can be measured in any user-defined region of interest on the pixelated EBSD detector. In doing so, not only can COM images be optimised for signal by taking into account where the BSE distribution peaks on the detector, but images dominated by topographic contrast, and showing surface steps, can also be obtained. This VDCOM technique is advantageous over traditional virtual diode imaging as by measuring the change in the centre of intensity distribution in the x and y directions, two different images with high-signal but different dominant contrast mechanism can be produced. Traditional virtual diode imaging leads to at least one image inevitably having poor signal-to-noise due to the asymmetry of the BSE distribution on the detector. VDCOM is also more flexible than ECCI imaging in that no physical hardware has to be moved to achieve different contrast and it is also simultaneously available alongside the quantitative information that EBSD provides. The technique is however very dependent on the setup geometry, sample and beam characteristics. Future developments would be to understand exactly what adjustments need to be made to the geometry and beam such that VDCOM can be optimised for any microscope and any sample.

Chapter 4 produced isotropic elasticity analytical simulations, written in Python, for the strain and lattice rotations associated with screw, edge and mixed TDs in GaN. These were performed at the surface and at a fixed depth below the surface. It was found that the misorientation and strain associated with a screw TD is significant both in-plane (around the specimen z axis) and out-of-plane, while that of the edge TD was significant only in-plane. This indicated that if the misorientation and strain profiles can be measured and mapped with sufficient resolution, then by comparing in-plane and out-of-plane strain and misorientation, it would be possible to distinguish between edge TDs and screw component TDs (screw and mixed) in GaN in plan-view geometry. A 'perturbed simulation' was then produced in an attempt to take into account the effects of the interaction volume on the strain distribution measured by EBSD. This, however, ignored diffraction effects and thus used only a ballpark depth for where the low-loss diffracted electrons originated from within the sample. While this number was still in agreement with the consensus found in literature, it would be better in

future to try to incorporate the effects of diffraction rather than using a simple Monte Carlo model. The effects of the orientation of the edge half plane relative to the oblique beam should also be considered in future perturbed simulations, as the distribution will change with different edge Burgers vectors and so the measurement may be distorted differently.

Chapter 5 measured and mapped the misorientation and strain associated with TDs in three different GaN samples. This had sufficient resolution to resolve the strain and misorientaion profiles of individual TDs. By interrogating how the misorientation axes changed from point to point on the samples, the subgrain structure became visible. By then comparing in-plane and out-of-plane components of the strain and Weighted Burgers Vector (curvature) it was possible to distinguish between screw-component (screw and mixed TDs) and edge TDs. Combining this information with the VDCOM images, TD densities and types were given for each sample. Due to surface relaxation and spatial resolution it is not possible at this point in time to distinguish between pure screw and mixed TDs. However, the future application of direct electron detectors should allow EBSD measurements to be taken at much lower beam energies which would significantly reduce the interaction volume size and therefore improve spatial resolution. By doing so, the dipole/quadrupole nature of the strain profiles should become visible and, with comparison to simulations, not only should the exact TD type become available but also its Burgers vector. The ability to map strain in this way should also prove useful for future investigations into how piezoelectric polarisation varies across the sample as well as aiding correlative studies which could look at variations in (opto)electronic properties as a result of local strain distributions. Furthermore, the differences between WBVx and WBVz should be more closely interrogated to explain the visual differences in the curvature distributions, such as the somewhat smeared out nature of WBVx compared to the more point like structures in WBVz. Another useful application for the weighted Burgers vector approach which could be applied in future to possibly discern the Burgers vector of individual TDs is to colour code the direction of the net WBV using crystal coordinates. This may produce a map which reveals the direction of Burgers vectors for TDs that are sufficiently separated.

Chapter 6 outlined the development of a further post-acquisition image processing technique which can be applied to EBSD datasets, Radon centre of mass (RCOM) imaging. This technique performs a Radon transformation on each background removed EBSP in an EBSD dataset, mapping the intensity along the Kikuchi bands to points in Radon space. By then applying the COM technique around one of these points in the Radon image (sinogram), images can be produced with contrast based on the distortion of that particular plane. This means only TDs affecting that plane are visible in the images. In plan-view EBSD, surface relaxation is significant for screw-component TDs, so again only edge/screw-component TDs can be distinguished. However, by utilising the invisibility criterion for edge TDs it was shown that it is possible to determine their exact Burgers vectors, which for both samples used in Chapter 6 was $1/3[11\bar{2}0]$. If cross-sectional samples were to be used in future, this RCOM technique would provide EBSD users with the same imaging capabilities as TEM users, where the Burgers vector of *any* TD can be determined. Due to the low signal in the Kikuchi bands however, the signal in the RCOM images can be quite low. This could perhaps be improved by using direct electron detection where energy filtering can be applied. This would improve signal-to-noise within the bands. Furthermore, higher resolution detectors may also mean that smaller changes are detectable which could improve signal. Finally, by analysing samples with much higher misorientation and strain, changes in the position of the intensity of the Kikuchi bands would be much more significant and may also improve image quality.

Bibliography

[1] H. of Commons, "The Semiconductor Industry in the UK," *Business, Energy and Industrial Strategy Commission*, 2022.

[2] O. Ambacher, "Growth and applications of group III-nitrides," *Journal of Physics D: Applied Physics*, vol. 31, no. 20, pp. 2653–2710, 1998.

[3] J. Millan, P. Godignon, X. Perpina, A. Perez-Tomas, and J. Rebollo, "A survey of wide bandgap power semiconductor devices," *IEEE Transactions on Power Electronics*, vol. 29, no. 5, pp. 2155–2163, 2014.

[4] F. A. Ponce and D. P. Bour, "Nitride-based semiconductors for blue and green light-emitting devices," *Nature*, vol. 386, no. 6623, pp. 351–359, 1997.

[5] U. K. Mishra, P. Parikh, and Y. F. Wu, "AlGaN/GaN HEMTs - An overview of device operation and applications," *Proceedings of the IEEE*, vol. 90, no. 6, pp. 1022–1031, 2002.

[6] J. S. Speck, "Role of threading dislocations in the physical properties of GaN and its alloys," *Materials Science Forum*, vol. 353-356, pp. 769–778, 2001.

[7] X. H. Wu, P. Fini, E. J. Tarsa, B. Heying, S. Keller, U. K. Mishra, S. P. DenBaars, and J. S. Speck, "Dislocation generation in GaN heteroepitaxy," *Journal of Crystal Growth*, vol. 189-190, pp. 231–243, 1998.

[8] S. J. Rosner, E. C. Carr, M. J. Ludowise, G. Girolami, and H. I. Erikson, "Correlation of cathodoluminescence inhomogeneity with microstructural defects in epi-

taxial GaN grown by metalorganic chemical-vapor deposition," *Applied Physics Letters*, vol. 70, no. 4, pp. 420–422, 1997.

[9] T. S, H. Sato, M. Hao, Y. Naoi, S. Kurai, and S. Tottori, ".Pdf," vol. 37, no. 4, pp. 398–400, 1998.

[10] W. Pantleon, "Resolving the geometrically necessary dislocation content by conventional electron backscattering diffraction," *Scripta Materialia*, vol. 58, no. 11, pp. 994–997, 2008.

[11] A. J. Wilkinson, "Assessment of lattice strain, rotation and dislocation content using electron back-scatter diffraction," *Journal of Physics: Conference Series*, vol. 326, no. 1, 2011.

[12] A. Vilalta-Clemente, G. Naresh-Kumar, M. Nouf-Allehiani, P. Gamarra, M. A. di Forte-Poisson, C. Trager-Cowan, and A. J. Wilkinson, "Cross-correlation based high resolution electron backscatter diffraction and electron channelling contrast imaging for strain mapping and dislocation distributions in InAlN thin films," *Acta Materialia*, vol. 125, pp. 125–135, 2017.

[13] C. Trager-Cowan, F. Sweeney, A. Winkelmann, A. J. Wilkinson, P. W. Trimby, A. P. Day, A. Gholinia, N. H. Schmidt, P. J. Parbrook, and I. M. Watson, "Characterisation of nitride thin films by electron backscatter diffraction and electron channelling contrast imaging," *Materials Science and Technology*, vol. 22, no. 11, pp. 1352–1358, 2006.

[14] C. Trager-Cowan, F. Sweeney, P. W. Trimby, A. P. Day, A. Gholinia, N. H. Schmidt, P. J. Parbrook, A. J. Wilkinson, and I. M. Watson, "Electron backscatter diffraction and electron channeling contrast imaging of tilt and dislocations in nitride thin films," *Physical Review B - Condensed Matter and Materials Physics*, vol. 75, no. 8, pp. 1–8, 2007.

[15] C. Trager-Cowan, A. Alasmari, W. Avis, J. Bruckbauer, P. R. Edwards, B. Hourahine, S. Kraeusel, G. Kusch, R. Johnston, G. Naresh-Kumar, R. W.

Martin, M. Nouf-Allehiani, E. Pascal, L. Spasevski, D. Thomson, S. Vespucci, P. J. Parbrook, M. D. Smith, J. Enslin, F. Mehnke, M. Kneissl, C. Kuhn, T. Wernicke, S. Hagedorn, A. Knauer, V. Kueller, S. Walde, M. Weyers, P.-M. Coulon, P. A. Shields, Y. Zhang, L. Jiu, Y. Gong, R. M. Smith, T. Wang, and A. Winkelmann, "Scanning electron microscopy as a flexible technique for investigating the properties of UV-emitting nitride semiconductor thin films," *Photonics Research*, vol. 7, no. 11, p. B73, 2019.

[16] A. Kelly and K. M. Knowles, *Crystallography and Crystal Defects*. Wiley.

[17] R. Steadman, *Crystallography*. Van Nostrand Reinhold.

[18] J. V. Smith, *Geometrical and Structural Crystallography*. Wiley.

[19] G. Z. J. P. Mercier and W. Kurz, *Introduction to Material Science*. Elsevier Science, 2003.

[20] H. P. Myers, *Introductory Solid State Physics*. Taylor and Francis.

[21] D. B. Holt and B. G. Yacobi, *Extended Defects in Semiconductors: Electronic Properties, Device Effects and Structures*. Cambridge University Press, 2007.

[22] D. Hull and D. J. Bacon, *Introduction to Dislocations*. Butterworth-Heinemann, 2011.

[23] B. Henderson, *Defects in Crystalline Solids*. Edward Arnold.

[24] S. Bellini, Y. Sun, F. Gallucci, and A. Caravella, "Thermodynamic aspects in non-ideal metal membranes for hydrogen purification," *Membranes*, vol. 8, no. 3, 2018.

[25] P. Lejcek, *Grain Boundary Segregation in Metals*. Heidelberg; New York, 2010.

[26] J. Salzman, C. Uzan-Saguy, B. Meyler, and R. Kalish, "Effect of grain boundaries on electrical conductivity in thin GaN layers," *Physica Status Solidi (A) Applied Research*, vol. 176, no. 1, pp. 683–687, 1999.

[27] A. Szyszka, B. Paszkiewicz, R. Paszkiewicz, and M. Tłaczała, "Study of grain boundaries influence on electrical properties of nitrides," *Vacuum*, vol. 82, no. 10, pp. 1034–1039, 2008.

[28] W. D. C. Jr. and D. G. Rethwisch, *Material Science and Engineering: An Introduction*. Wiley, 2003.

[29] W. F. Hosford, *Fundamentals of Engineering Plasticity*. Cambridge University Press, 2013.

[30] J. Frenkel, "Zur Theorie der Elastizitätsgrenze und der Festigkeit kristallinischer Körper," *Zeitschrift für Physik*, vol. 37, no. 7-8, pp. 572–609, 1926.

[31] G. I. Taylor, "The mechanism of plastic deformation of crystals. Part I.- Theoretical," *Proceeding of the Royal Society of London*, vol. 145, no. 855, 1934.

[32] M. Polanyi *Physics*, vol. 605, 614, 634, 1934.

[33] E. Orowan *Physics*, vol. 605, 614, 634, 1934.

[34] A. M. K. E. M. Lifshitz and L. P. Pitaevskii, *Theory of Elasticity*. Butterworth-Heinemann, 1986.

[35] N. F. Nye, *Physical Properties of Crystals*. Oxford University Press.

[36] J. F. Shroder, *Treatise on Geomorphology*. Elsevier, 2013.

[37] A. M. Rodríguez, G. Bozzolo, and J. Ferrante, "Multilayer relaxation and surface energies of fcc and bcc metals using equivalent crystal theory," *Surface Science*, vol. 289, no. 1, pp. 100–126, 1993.

[38] X. Liu and M. C. Hersam, "Interface Characterization and Control of 2D Materials and Heterostructures," *Advanced Materials*, vol. 30, no. 39, 2018.

[39] M. W. Finnis and V. Heine, "Theory of lattice contraction at aluminium surfaces," *Journal of Physics F: Metal Physics*, vol. 4, no. 3, 1974.

[40] B. Gurrutxaga-Lerma, D. S. Balint, D. Dini, and A. P. Sutton, "Elastodynamic image forces on dislocations," *Proceedings of the Royal Society A: Mathematical, Physical and Engineering Sciences*, vol. 471, no. 2181, 2015.

[41] E. H. Yoffe, "A dislocation at a free surface," *Philosophical Magazine*, vol. 6, no. 69, pp. 1147–1155, 1961.

[42] H. Yu, J. Liu, P. Karamched, A. J. Wilkinson, and F. Hofmann, "Mapping the full lattice strain tensor of a single dislocation by high angular resolution transmission Kikuchi diffraction (HR-TKD)," *Scripta Materialia*, vol. 164, pp. 36–41, 2019.

[43] M. Frentrup, L. Y. Lee, S. L. Sahonta, M. J. Kappers, F. Massabuau, P. Gupta, R. A. Oliver, C. J. Humphreys, and D. J. Wallis, "X-ray diffraction analysis of cubic zincblende III-nitrides," *Journal of Physics D: Applied Physics*, vol. 50, no. 43, p. aa865e, 2017.

[44] M. Leszczynski, H. Teisseyre, T. Suski, I. Grzegory, M. Bockowski, J. Jun, S. Porowski, K. Pakula, J. M. Baranowski, C. T. Foxon, and T. S. Cheng, "Lattice parameters of gallium nitride," *Applied Physics Letters*, vol. 69, no. 1, pp. 73–75, 1996.

[45] J. S. Speck and S. F. Chichibu, "Nonpolar and semipolar Group III nitride-based materials," *MRS Bulletin*, vol. 34, no. 5, pp. 304–309, 2009.

[46] H. P. Maruska and W. C. Rhines, "A modern perspective on the history of semiconductor nitride blue light sources," *Solid-State Electronics*, vol. 111, pp. 32–41, 2015.

[47] M. Grundmann, *The Physics of Semiconductors: An Introduction Including Nanophysics and Applications*. Springer Cham, 2016.

[48] C. Persson, A. Ferreira Da Silva, R. Ahuja, and B. Johansson, "Effective electronic masses in wurtzite and zinc-blende GaN and AlN," *Journal of Crystal Growth*, vol. 231, no. 3, pp. 397–406, 2001.

[49] M. Suzuki and T. Uenoyama, "First-principles calculation of effective mass parameters of gallium nitride," *Japanese Journal of Applied Physics*, vol. 34, no. 7R, pp. 3442–3446, 1995.

[50] O. Ambacher, B. Foutz, J. Smart, J. R. Shealy, N. G. Weimann, K. Chu, M. Murphy, A. J. Sierakowski, W. J. Schaff, L. F. Eastman, R. Dimitrov, A. Mitchell, and M. Stutzmann, "Two dimensional electron gases induced by spontaneous and piezoelectric polarization in undoped and doped AlGaN/GaN heterostructures," *Journal of Applied Physics*, vol. 87, no. 1, pp. 334–344, 2000.

[51] M. A. Littlejohn, J. R. Hauser, and T. H. Glisson, "Monte Carlo calculation of the velocity-field relationship for gallium nitride," *Applied Physics Letters*, vol. 26, no. 11, pp. 625–627, 1975.

[52] F. Bernardini, V. Fiorentini, and D. Vanderbilt, "Spontaneous polarization and piezoelectric constants of III-V nitrides," *Physical Review B - Condensed Matter and Materials Physics*, vol. 56, no. 16, pp. R10024–R10027, 1997.

[53] W. Soluch, E. Brzozowski, M. Lysakowska, and J. Sadura, "Determination of mass density, dielectric, elastic, and piezoelectric constants of bulk GaN crystal," *IEEE Transactions on Ultrasonics, Ferroelectrics, and Frequency Control*, vol. 58, no. 11, pp. 2469–2474, 2011.

[54] G. D. O'Clock and M. T. Duffy, "Acoustic surface wave properties of epitaxially grown aluminum nitride and gallium nitride on sapphire," *Applied Physics Letters*, vol. 23, no. 2, pp. 55–56, 1973.

[55] M. A. Caro, S. Schulz, and E. P. O'Reilly, "Theory of local electric polarization and its relation to internal strain: Impact on polarization potential and electronic properties of group-III nitrides," *Physical Review B - Condensed Matter and Materials Physics*, vol. 88, no. 21, pp. 1–22, 2013.

[56] F. Schwierz, "An electron mobility model for wurtzite GaN," *Solid-State Electronics*, vol. 49, no. 6, pp. 889–895, 2005.

[57] S. Porowski, "Bulk and homoepitaxial GaN-growth and characterisation," *Journal of Crystal Growth*, vol. 189-190, pp. 153–158, 1998.

[58] A. Krost and A. Dadgar, "GaN-based optoelectronics on silicon substrates," *Materials Science and Engineering: B*, vol. 93, no. 1-3, pp. 77–84, 2002.

[59] H. P. Maruska and J. J. Tietjan, "The Preparation and Properties of Vapor-deposited Single Crystal-line GaN," *Applied Physics Letters*, vol. 15, pp. 327–329, 1969.

[60] B. Beaumont, M. Vaille, T. Boufaden, B. El Jani, and P. Gibart, "High quality GaN grown by MOVPE," *Journal of Crystal Growth*, vol. 170, no. 1-4, pp. 316–320, 1997.

[61] K. Matsumoto, H. Tokunaga, A. Ubukata, K. Ikenaga, Y. Fukuda, T. Tabuchi, Y. Kitamura, S. Koseki, A. Yamaguchi, and K. Uematsu, "High growth rate metal organic vapor phase epitaxy GaN," *Journal of Crystal Growth*, vol. 310, no. 17, pp. 3950–3952, 2008.

[62] P. Rudolph, *Handbook of Crystal Growth*. Elsevier, 2015.

[63] W. A. Melton and J. I. Pankove, "GaN growth on sapphire," *Journal of Crystal Growth*, vol. 178, no. 1-2, pp. 168–173, 1997.

[64] S. Nakamura, "Gan growth using gan buffer layer," *Japanese Journal of Applied Physics*, vol. 30, no. 10A, pp. L1705–L1707, 1991.

[65] I. M. Watson, "Metal organic vapour phase epitaxy of AlN, GaN, InN and their alloys: A key chemical technology for advanced device applications," *Coordination Chemistry Reviews*, vol. 257, no. 13-14, pp. 2120–2141, 2013.

[66] H. Morkoç, S. Strite, G. B. Gao, M. E. Lin, B. Sverdlov, and M. Burns, "Large-band-gap SiC, III-V nitride, and II-VI ZnSe-based semiconductor device technologies," *Journal of Applied Physics*, vol. 76, no. 3, pp. 1363–1398, 1994.

[67] H. Amano, K. Hiramatsu, and I. Akasaki, "Heteroepitaxial growth and the effect of strain on the luminescent properties of gan films on (11-0) and (0001) sapphire substrates," *Japanese Journal of Applied Physics*, vol. 27, no. 8 A, pp. L1384–L1386, 1988.

[68] S. D. Lester, F. A. Ponce, M. G. Craford, and D. A. Steigerwald, "High dislocation densities in high efficiency GaN-based light-emitting diodes," *Applied Physics Letters*, vol. 1251, p. 1249, 1995.

[69] X. J. Ning, F. R. Chien, P. Pirouz, J. W. Yang, and M. Asif Khan, "Growth defects in GaN films on sapphire: The probable origin of threading dislocations," *Journal of Materials Research*, vol. 11, no. 3, pp. 580–592, 1996.

[70] R. A. Oliver, M. J. Kappers, C. McAleese, R. Datta, J. Sumner, and C. J. Humphreys, "The origin and reduction of dislocations in Gallium Nitride," *Journal of Materials Science: Materials in Electronics*, vol. 19, no. SUPPL. 1, pp. 208–214, 2008.

[71] T. J. O'Hanlon, T. Zhu, F. C. Massabuau, and R. A. Oliver, "Dislocations at coalescence boundaries in heteroepitaxial GaN/sapphire studied after the epitaxial layer has completely coalesced," *Ultramicroscopy*, vol. 231, no. March, p. 113258, 2021.

[72] V. Narayanan, K. Lorenz, W. Kim, and S. Mahajan, "Origins of threading dislocations in GaN epitaxial layers grown on sapphire by metalorganic chemical vapor deposition," *Applied Physics Letters*, vol. 78, no. 11, pp. 1544–1546, 2001.

[73] M. A. Moram, R. A. Oliver, M. J. Kappers, and C. J. Humphreys, "The spatial distribution of threading dislocations in gallium nitride films," *Advanced Materials*, vol. 21, no. 38-39, pp. 3941–3944, 2009.

[74] V. Narayanan, K. Lorenz, W. Kim, and S. Mahajan, "Gallium nitride epitaxy on (0001) sapphire," *Philosophical Magazine A: Physics of Condensed Matter, Structure, Defects and Mechanical Properties*, vol. 82, no. 5, pp. 885–912, 2002.

[75] S. E. Bennett, "Dislocations and their reduction in GaN," *Materials Science and Technology*, vol. 26, no. 9, pp. 1017–1028, 2010.

[76] I. P. Smorchkova, C. R. Elsass, J. P. Ibbetson, R. Vetury, B. Heying, P. Fini, E. Haus, S. P. DenBaars, J. S. Speck, and U. K. Mishra, "Polarization-induced charge and electron mobility in AlGaN/GaN heterostructures grown by plasma-assisted molecular-beam epitaxy," *Journal of Applied Physics*, vol. 86, pp. 4520–4526, 10 1999.

[77] B. Chatterjee, D. Shoemaker, H.-Y. Wong, and S. Choi, "6 - algan/gan hemt device physics and electrothermal modeling," in *Thermal Management of Gallium Nitride Electronics* (M. J. Tadjer and T. J. Anderson, eds.), Woodhead Publishing Series in Electronic and Optical Materials, pp. 103–163, Woodhead Publishing, 2022.

[78] J. He, W. C. Cheng, Q. Wang, K. Cheng, H. Yu, and Y. Chai, "Recent Advances in GaN-Based Power HEMT Devices," *Advanced Electronic Materials*, vol. 7, no. 4, pp. 1–24, 2021.

[79] M. Meneghini, G. Meneghesso, and E. Zanoni, *Power GaN Devices*. Springer Cham, 2017.

[80] J. Pankove, E. Miller, D. Richman, and J. E. Berkeyheiser, "Electroluminescence in GaN," *Journal of Luminescence*, vol. 4, pp. 63–66, 1971.

[81] S. Nakamura, M. Senoh, N. Iwasa, and S. I. Nagahama, "High-brightness InGaN blue, green and yellow light-emitting diodes with quantum well structures," *Japanese Journal of Applied Physics*, vol. 34, no. 7, pp. L797–L799, 1995.

[82] S. P. Denbaars, D. Feezell, K. Kelchner, S. Pimputkar, C. C. Pan, C. C. Yen, S. Tanaka, Y. Zhao, N. Pfaff, R. Farrell, M. Iza, S. Keller, U. Mishra, J. S. Speck, and S. Nakamura, "Development of gallium-nitride-based light-emitting diodes (LEDs) and laser diodes for energy-efficient lighting and displays," *Acta Materialia*, vol. 61, no. 3, pp. 945–951, 2013.

[83] G. Koley and M. G. Spencer, "Scanning Kelvin probe microscopy characterization of dislocations in III-nitrides grown by metalorganic chemical vapor deposition," *Applied Physics Letters*, vol. 78, no. 19, pp. 2873–2875, 2001.

[84] P. J. Hansen, Y. E. Strausser, A. N. Erickson, E. J. Tarsa, P. Kozodoy, E. G. Brazel, J. P. Ibbetson, U. Mishra, V. Narayanamurti, S. P. DenBaars, and J. S. Speck, "Scanning capacitance microscopy imaging of threading dislocations in GaN films grown on (0001) sapphire by metalorganic chemical vapor deposition," *Applied Physics Letters*, vol. 72, no. 18, pp. 2247–2249, 1998.

[85] E. G. Braze, M. A. Chin, and V. Narayanamurti, "Direct observation of localized high current densities in GaN films," *Applied Physics Letters*, vol. 74, no. 16, pp. 2367–2369, 1999.

[86] G. Maciejewski, S. Kret, and P. Ruterana, "Piezoelectric field around threading dislocation in GaN determined on the basis of high-resolution transmission electron microscopy image," *Journal of Microscopy*, vol. 223, no. 3, pp. 212–215, 2006.

[87] N. S. Al-Mamun, M. Wetherington, D. E. Wolfe, A. Haque, F. Ren, and S. Pearton, "Local strain modification effects on global properties of AlGaN/GaN high electron mobility transistors," *Microelectronic Engineering*, vol. 262, p. 111836, 2022.

[88] N. G. Weimann, L. F. Eastman, D. Doppalapudi, H. M. Ng, and T. D. Moustakas, "Scattering of electrons at threading dislocations in GaN," *Journal of Applied Physics*, vol. 83, no. 7, pp. 3656–3659, 1998.

[89] H. M. Ng, D. Doppalapudi, T. D. Moustakas, N. G. Weimann, and L. F. Eastman, "The role of dislocation scattering in n-type GaN films," *Applied Physics Letters*, vol. 73, no. 6, pp. 821–823, 1998.

[90] A. Ul-Hamid, *A Beginner's Guide to Scanning Electron Microscopy*. Springer, 2023.

[91] D. B. Williams and C. B. Carter, *Transmission Electron Microscopy*. Springer, 2009.

[92] E. Rutherford *Philosophical Magazine*, vol. 6, no. 21, 1911.

[93] K. Kanaya and S. Okayama, "Penetration and energy-loss theory of electrons in solid targets," *Journal of Physics D: Applied Physics*, vol. 5, no. 1, pp. 43–58, 1972.

[94] A. J. Schwartz, *Electron Backscatter Diffraction in Materials Science*. Springer, NY.

[95] D. Drouin, A. R. Couture, D. Joly, X. Tastet, V. Aimez, and R. Gauvin, "CASINO V2.42 - A fast and easy-to-use modeling tool for scanning electron microscopy and microanalysis users," *Scanning*, vol. 29, no. 3, pp. 92–101, 2007.

[96] A. Winkelmann, G. Nolze, M. Vos, F. Salvat-Pujol, and W. S. Werner, "Physics-based simulation models for EBSD: Advances and challenges," *IOP Conference Series: Materials Science and Engineering*, vol. 109, no. 1, 2016.

[97] A. Winkelmann, F. Salvat-Pujol, and W. Werner, "Monte Carlo Simulations for Applications in Electron Backscatter Diffraction," *Microscopy and Microanalysis*, vol. 19, no. S2, pp. 738–739, 2013.

[98] A. Winkelmann, "Principles of depth-resolved Kikuchi pattern simulation for electron backscatter diffraction," *Journal of Microscopy*, vol. 239, no. 1, pp. 32–45, 2010.

[99] P. G. Callahan and M. D. Graef, "Dynamical Electron Backscatter Diffraction Patterns," *Microscopy and Microanalysis*, pp. 1255–1265, 2013.

[100] J. I. Goldstein, *Scanning Electron Microscopy and X-Ray Microanalysis*. Springer, NY.

[101] S. Vespucci, A. Winkelmann, G. Naresh-Kumar, K. P. Mingard, D. Maneuski, P. R. Edwards, A. P. Day, V. O'Shea, and C. Trager-Cowan, "Digital direct electron imaging of energy-filtered electron backscatter diffraction patterns," *Physical*

Review B - Condensed Matter and Materials Physics, vol. 92, no. 20, pp. 8–14, 2015.

[102] J. A. Mir, R. Clough, R. MacInnes, C. Gough, R. Plackett, I. Shipsey, H. Sawada, I. MacLaren, R. Ballabriga, D. Maneuski, V. O'Shea, D. McGrouther, and A. I. Kirkland, "Characterisation of the Medipix3 detector for 60 and 80 keV electrons," *Ultramicroscopy*, vol. 182, pp. 44–53, 2017.

[103] R. Ballabriga, J. Alozy, G. Blaj, M. Campbell, M. Fiederle, E. Frojdh, E. H. Heijne, X. Llopart, M. Pichotka, S. Procz, L. Tlustos, and W. Wong, "The medipix3RX: A high resolution, zero dead-time pixel detector readout chip allowing spectroscopic imaging," *Journal of Instrumentation*, vol. 8, no. 2, 2013.

[104] A. Deal, T. Hooghan, and A. Eades, "Energy-filtered electron backscatter diffraction," *Ultramicroscopy*, vol. 108, no. 2, pp. 116–125, 2008.

[105] A. Winkelmann, G. Nolze, S. Vespucci, G. Naresh-Kumar, C. Trager-Cowan, A. Vilalta-Clemente, A. J. Wilkinson, and M. Vos, "Diffraction effects and inelastic electron transport in angle-resolved microscopic imaging applications," *Journal of Microscopy*, vol. 267, no. 3, pp. 330–346, 2017.

[106] A. Winkelmann, C. Trager-Cowan, F. Sweeney, A. P. Day, and P. Parbrook, "Many-beam dynamical simulation of electron backscatter diffraction patterns," *Ultramicroscopy*, vol. 107, no. 4-5, pp. 414–421, 2007.

[107] A. Winkelmann, G. Nolze, G. Cios, T. Tokarski, P. Bała, B. Hourahine, and C. Trager-Cowan, "Kikuchi pattern simulations of backscattered and transmitted electrons," *Journal of Microscopy*, vol. 284, no. 2, pp. 157–184, 2021.

[108] N. C. K. Lassen, "Image Processing Procedures for Analysis of Electron Back Scattering Patterns," vol. 6, no. 1, 1992.

[109] M. V. Ginkel, C. L. L. Hendriks, L. J. V. Vliet, C. L. Luengo Hendriks, and L. J. V. Vliet, "A short introduction to the Radon and Hough transforms and how they relate to each other," *Reading*, no. May 2013, pp. 1–11, 2004.

[110] T. B. Britton, J. Jiang, Y. Guo, A. Vilalta-clemente, D. Wallis, L. N. Hansen, A. Winkelmann, and A. J. Wilkinson, "Materials Characterization Tutorial : Crystal orientations and EBSD — Or which way is up ?," *Materials Characterization*, vol. 117, pp. 113–126, 2016.

[111] H.-J. Bunge, *Texture Analysis in Materials Science*. Butterworth-Heinemann, 1969.

[112] F. J. Humphreys, "Quantitative metallography by electron backscattered diffraction," *Journal of Microscopy*, vol. 195, no. 3, pp. 170–185, 1999.

[113] G. Nolze, M. Jürgens, J. Olbricht, and A. Winkelmann, "Improving the precision of orientation measurements from technical materials via EBSD pattern matching," *Acta Materialia*, vol. 159, pp. 408–415, 2018.

[114] A. Winkelmann *et al.*, "Improving EBSD precision by orientation refinement with full pattern matching," *Journal of Microscopy*, vol. 277, no. 2, pp. 79–92, 2020.

[115] A. J. Wilkinson, G. Meaden, and D. J. Dingley, "High-resolution elastic strain measurement from electron backscatter diffraction patterns: New levels of sensitivity," *Ultramicroscopy*, vol. 106, no. 4-5, pp. 307–313, 2006.

[116] A. J. Wilkinson and D. Randman, "Determination of elastic strain fields and geometrically necessary dislocation distributions near nanoindents using electron back scatter diffraction," *Philosophical Magazine*, vol. 90, no. 9, pp. 1159–1177, 2010.

[117] S. Villert, C. Maurice, C. Wyon, and R. Fortunier, "Accuracy assessment of elastic strain measurement by EBSD," *Journal of Microscopy*, vol. 233, no. 2, pp. 290–301, 2009.

[118] T. B. Britton and J. L. Hickey, "Understanding deformation with high angular resolution electron backscatter diffraction (HR-EBSD)," *IOP Conference Series: Materials Science and Engineering*, vol. 304, no. 1, 2018.

[119] G. Nolze, A. Winkelmann, G. Cios, and T. Tokarski, "Tetragonality mapping of martensite in a high-carbon steel by EBSD," *Materials Characterization*, vol. 175, 2021.

[120] A. Winkelmann, G. Nolze, G. Cios, and T. Tokarski, "Mapping of local lattice parameter ratios by projective Kikuchi pattern matching," *Physical Review Materials*, vol. 2, no. 12, pp. 1–7, 2018.

[121] J. Lähnemann, V. M. Kaganer, K. K. Sabelfeld, A. E. Kireeva, U. Jahn, C. Chèze, R. Calarco, and O. Brandt, "Carrier Diffusion in GaN: A Cathodoluminescence Study. III. Nature of Nonradiative Recombination at Threading Dislocations," *Phys. Rev. Appl.*, vol. 17, p. 024019, 2022.

[122] A. J. Wilkinson and P. B. Hirsch, "Electron diffraction based techniques in scanning electron microscopy of bulk materials," *Micron*, vol. 28, p. 279, 1997.

[123] M. A. Crimp, B. A. Simkin, and B. C. Ng, "Demonstration of the g · b x u = 0 edge dislocation invisibility criterion for electron channelling contrast imaging," *Philosophical Magazine Letters*, vol. 81, p. 833, 2001.

[124] J. Hite, M. Mastro, and C. Eddy, "Approach for dislocation free GaN epitaxy," *Journal of Crystal Growth*, vol. 312, p. 3143, 2010.

[125] Y. N. Picard, R. Kamaladasa, M. De Graef, N. T. Nuhfer, W. J. Mershon, T. Owens, L. Sedlacek, and F. Lopour, "Future Prospects for Defect and Strain Analysis in the SEM via Electron Channeling," *Microscopy Today*, vol. 20, p. 12, 2012.

[126] G. Naresh-Kumar, B. Hourahine, P. R. Edwards, A. P. Day, A. Winkelmann, A. J. Wilkinson, P. J. Parbrook, G. England, and C. Trager-Cowan, "Rapid nondestructive analysis of threading dislocations in wurtzite materials using the scanning electron microscope," *Physical Review Letters*, vol. 108, p. 135503, 2012.

[127] S. Zaefferer and N. N. Elhami, "Theory and application of electron channelling contrast imaging under controlled diffraction conditions," *Acta Materialia*, vol. 75, p. 20, 2014.

[128] S. D. Carnevale, J. I. Deitz, J. A. Carlin, Y. N. Picard, M. De Graef, S. A. Ringel, and T. J. Grassman, "Rapid misfit dislocation characterization in heteroepitaxial III-V/Si thin films by electron channeling contrast imaging," *Applied Physics Letters*, vol. 104, p. 232111, 2014.

[129] K. N. Yaung, S. Kirnstoetter, J. Faucher, A. Gerger, A. Lochtefeld, A. Barnett, and M. L. Lee, "Threading dislocation density characterization in III–V photovoltaic materials by electron channeling contrast imaging," *Journal of Crystal Growth*, vol. 453, p. 65, 2016.

[130] N. Brodusch, H. Demers, and R. Gauvin, *Electron Diffraction Techniques in the SEM*, pp. 85–105. Springer Singapore, 2018.

[131] P. G. Callahan, B. B. Haidet, D. Jung, G. G. E. Seward, and K. Mukherjee, "Direct observation of recombination-enhanced dislocation glide in heteroepitaxial GaAs on silicon," *Phys. Rev. Mater.*, vol. 2, p. 081601, 2018.

[132] S. Kaboli and P. C. Burnley, "Direct observations of crystal defects in polycrystalline diamond," *Materials Characterization*, vol. 142, p. 154, 2018.

[133] N. Miyajima, Y. Li, S. Abeykoon, and F. Heidelbach, "Electron channelling contrast imaging of individual dislocations in geological materials using a field-emission scanning electron microscope equipped with an EBSD system," *European Journal of Mineralogy*, vol. 30, p. 5, 2018.

[134] A. Schulze, L. Strakos, T. Vystavel, R. Loo, A. Pacco, N. Collaert, W. Vandervorst, and M. Caymax, "Non-destructive characterization of extended crystalline defects in confined semiconductor device structures," *Nanoscale*, vol. 10, p. 7058, 2018.

[135] G. L'hôte, C. Lafond, P. Steyer, S. Deschanel, T. Douillard, C. Langlois, and S. Cazottes, "Rotational-Electron Channeling Contrast Imaging analysis of dislocation structure in fatigued copper single crystal," *Scripta Materialia*, vol. 162, p. 103, 2019.

[136] H. Han, T. Hantschel, L. Strakos, T. Vystavel, M. Baryshnikova, Y. Mols, B. Kunert, R. Langer, W. Vandervorst, and M. Caymax, "Application of electron channeling contrast imaging to 3D semiconductor structures through proper detector configurations," *Ultramicroscopy*, vol. 210, p. 112928, 2020.

[137] R. A. Schwarzer and J. Sukkau, "Electron back scattered diffraction: current state, prospects and comparison with x-ray diffraction texture measurement," *Banaras Metall*, vol. 18, p. 1, 2013.

[138] M. M. Nowell, S. I. Wright, T. Rampton, and R. de Kloe, "Advances in Scattered Electron Intensity Distribution Imaging for Microstructural Visualization and Correlations with EBSD Measurements," *Microscopy and Microanalysis*, vol. 20, p. 856, 2014.

[139] T. M. Rampton, M. M. Nowell, and S. I. Wright, "New Tools for the Study of Deformed and Heat-Treated Materials via Electron Backscatter Diffraction," *Microscopy and Microanalysis*, vol. 20, p. 1482, 2014.

[140] S. I. Wright, M. M. Nowell, R. De Kloe, P. Camus, and T. Rampton, "Electron imaging with an EBSD detector," *Ultramicroscopy*, vol. 148, p. 132, 2015.

[141] N. Brodusch, H. Demers, and R. Gauvin, "Dark-field imaging based on post-processed electron backscatter diffraction patterns of bulk crystalline materials in a scanning electron microscope," *Ultramicroscopy*, vol. 148, p. 123, 2015.

[142] G. Nolze, R. Hielscher, and A. Winkelmann, "Electron backscatter diffraction beyond the mainstream," *Crystal Research and Technology*, vol. 52, p. 1600252, 2017.

[143] N. Brodusch, H. Demers, and R. Gauvin, "Imaging with a commercial electron backscatter diffraction (EBSD) camera in a scanning electron microscope: A review," *Journal of Imaging*, vol. 4, p. 88, 2018.

[144] O. C. Wells, R. J. Savoy, P. J. Bailey, O. C. Wells, R. J. Savoy, and P. J. Bailey, "Backscattered Electron (BSE) Imaging in the Scanning Electron Microscope (SEM) - Measurement of Surface Layer Mass- Thickness," *Scanning Electron Microscopy*, vol. 1982, p. 25, 1982.

[145] T. Tanaka, K. Kawakami, H. Mogi, and S. Arai, "An EBSD camera as a tool to characterise in-plane magnetisation vectors on Fe-Si (001) surface," *Ultramicroscopy*, vol. 250, p. 113754, 2023.

[146] A. Winkelmann, G. Cios, T. Tokarski, P. Bała, Y. Grin, and U. Burkhardt, "Assignment of chiral elemental crystal structures using Kikuchi diffraction," *Materials Characterization*, vol. 196, p. 112633, 2023.

[147] T. A. Lafford, P. J. Parbrook, and B. K. Tanner, "Direct, independent measurement of twist and tilt mosaic as a function of thickness in epitaxial GaN," *Physica Status Solidi C: Conferences*, vol. 545, no. 1, pp. 542–545, 2002.

[148] S. Walde, S. Hagedorn, P. M. Coulon, A. Mogilatenko, C. Netzel, J. Weinrich, N. Susilo, E. Ziffer, L. Matiwe, C. Hartmann, G. Kusch, A. Alasmari, G. Naresh-Kumar, C. Trager-Cowan, T. Wernicke, T. Straubinger, M. Bickermann, R. W. Martin, P. A. Shields, M. Kneissl, and M. Weyers, "AlN overgrowth of nano-pillar-patterned sapphire with different offcut angle by metalorganic vapor phase epitaxy," *Journal of Crystal Growth*, vol. 531, no. November 2019, pp. 1–6, 2020.

[149] M. Chapman, P. G. Callahan, and M. De Graef, "Determination of sample surface topography using electron back-scatter diffraction patterns," *Scripta Materialia*, vol. 120, p. 23, 2016.

[150] J. M. Wagner and F. Bechstedt, "Properties of strained wurtzite GaN and AlN: Ab initio studies," *Physical Review B - Condensed Matter and Materials Physics*, vol. 66, no. 11, pp. 1–20, 2002.

[151] C. Kisielowski, J. Krüger, S. Ruvimov, T. Suski, J. Ager, E. Jones, Z. Liliental-Weber, M. Rubin, E. Weber, M. Bremser, and R. Davis, "Strain-related phenomena in GaN thin films," *Physical Review B - Condensed Matter and Materials Physics*, vol. 54, no. 24, pp. 17745–17753, 1996.

[152] M. A. Moram, Z. H. Barber, and C. J. Humphreys, "Accurate experimental determination of the Poisson's ratio of GaN using high-resolution x-ray diffraction," *Journal of Applied Physics*, vol. 102, no. 2, 2007.

[153] F. Bachmann, R. Hielscher, and H. Schaeben, "Texture analysis with MTEX- Free and open source software toolbox," *Solid State Phenomena*, vol. 160, pp. 63–68, 2010.

[154] S. Sun, B. L. Adams, and W. E. King, "Observations of lattice curvature near the interface of a deformed aluminium bicrystal," *Philosophical Magazine A: Physics of Condensed Matter, Structure, Defects and Mechanical Properties*, vol. 80, no. 1, pp. 9–25, 2000.

[155] J. Wheeler, E. Mariani, S. Piazolo, D. J. Prior, P. J. Trimby, and M. R. Drury, "The Weighted Burgers Vector: A quantity for constraining dislocation densities and types using electron backscatter diffraction on 2D sections through crystalline materials," *Materials Science Forum*, vol. 715-716, pp. 732–736, 2012.

[156] J. Wheeler, S. Piazolo, D. J. Prior, P. W. Trimby, and J. A. Tielke, "Using crystal-lattice distortion data for geological investigations: the weighted Burgers vector method," *Journal of Structural Geology*, vol. 179, no. December 2022, p. 105040, 2024.

[157] B. Pécz, M. A. Di Forte-Poisson, F. Huet, G. Radnóczi, L. Tóth, V. Papaioannou, and J. Stoemenos, "Growth of GaN layers onto misoriented (0001) sapphire by metalorganic chemical vapor deposition," *Journal of Applied Physics*, vol. 86, no. 11, pp. 6059–6067, 1999.

[158] F. C. Massabuau, J. Bruckbauer, and R. A. Oliver, "Microscopy of defects in semiconductors 10 . 2 Basic principles of the microscopy techniques,"

[159] D. J. Dingley, "Dislocation Invisibility in Dark-Field Electron Microscopy," *Physica Status Solidi (B)*, vol. 38, no. 1, pp. 345–355, 1970.

[160] M. Gandais, A. Hihi, C. Willaime, and Y. Efelboin, "Dislocation contrast by transmission electron microscopy A method for Burgers vector characterization if the invisibility criterion is not valid," *Philosophical Magazine A: Physics of Condensed Matter, Structure, Defects and Mechanical Properties*, vol. 45, no. 3, pp. 387–400, 1982.

[161] R. Datta, M. J. Kappers, J. S. Barnard, and C. J. Humphreys, "Revealing all types of threading dislocations in GaN with improved contrast in a single plan view image," *Applied Physics Letters*, vol. 85, no. 16, pp. 3411–3413, 2004.

[162] D. M. Follstaedt, N. A. Missert, D. D. Koleske, C. C. Mitchell, and K. C. Cross, "Plan-view image contrast of dislocations in GaN," *Applied Physics Letters*, vol. 83, no. 23, pp. 4797–4799, 2003.

[163] J. Sukkau and R. A. Schwarzer, "Reconstruction of Kikuchi patterns by intensity-enhanced Radon transformation," *Pattern Recognition Letters*, vol. 33, no. 6, pp. 739–743, 2012.

[164] D. J. Rowenhorst, P. G. Callahan, and H. W. Ånes, "Fast Radon transforms for high-precision EBSD orientation determination using PyEBSDIndex," *Journal of Applied Crystallography*, vol. 57, pp. 3–19, 2024.

[165] Y. Han, R. Li, Y. Zeng, and M. Liu, "Automatic detection of Kikuchi bands based on Radon transform and PPHT," *Journal of Microscopy*, vol. 285, no. 2, pp. 95–111, 2022.

[166] R. A. Schwarzer and J. Hjelen, "High-speed orientation microscopy with offline solving sequences of EBSD patterns," *Solid State Phenomena*, vol. 160, pp. 295–300, 2010.

[167] R. Hielscher, F. Bartel, and T. B. Britton, "Gazing at crystal balls: Electron backscatter diffraction pattern analysis and cross correlation on the sphere," *Ultramicroscopy*, vol. 207, no. September, p. 112836, 2019.

[168] A. Winkelmann, "Dynamical effects of anisotropic inelastic scattering in electron backscatter diffraction," *Ultramicroscopy*, vol. 108, no. 12, pp. 1546–1550, 2008.

[169] W. van Aarle, W. J. Palenstijn, J. De Beenhouwer, T. Altantzis, S. Bals, K. J. Batenburg, and J. Sijbers, "The ASTRA Toolbox: A platform for advanced algorithm development in electron tomography," *Ultramicroscopy*, vol. 157, no. 2015, pp. 35–47, 2015.

[170] W. van Aarle, W. J. Palenstijn, J. Cant, E. Janssens, F. Bleichrodt, A. Dabravolski, J. De Beenhouwer, K. Joost Batenburg, and J. Sijbers, "Fast and flexible X-ray tomography using the ASTRA toolbox," *Optics Express*, vol. 24, no. 22, p. 25129, 2016.

[171] S. Zaefferer, "Computer-aided crystallographic analysis in the TEM," *Advances in Imaging and Electron Physics*, vol. 125, 2003.